Julius-Maximilians-
UNIVERSITÄT
WÜRZBURG

Fakultät für
Physik und Astronomie

Dissertation zur Erlangung des naturwissenschaftlichen Doktorgrades der Bayerischen Julius-Maximilians-Universität Würzburg

Modelling high-energy observables of supernova explosions

vorgelegt von

Alexander Summa

aus Hünfeld

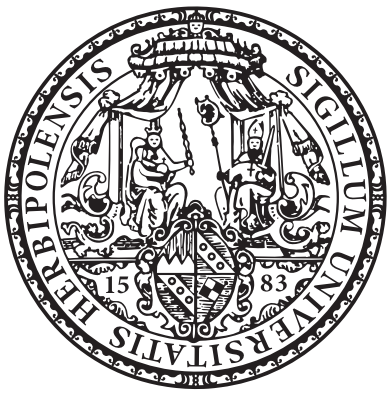

Würzburg 2014

Eingereicht am: 24.02.2014
bei der Fakultät für Physik und Astronomie.

1. Gutachter: .....
2. Gutachter: .....
3. Gutachter: .....

der Dissertation.

1. Prüfer: .....
2. Prüfer: .....
3. Prüfer: .....

im Promotionskolloquium.

Tag des Promotionskolloquiums: .....

Doktorurkunde ausgehändigt am: .....

There is something fascinating about science.
One gets such wholesale returns of conjecture
out of such a trifling investment of fact.

Mark Twain, Life on the Mississippi

Contents

List of Figures

1 Introduction

In this work, the diagnostic value of high-energy observables for selected types and evolutionary stages of supernova explosions is discussed. The aim of this chapter is to lay a foundation for all aspects of supernovae that are studied in the following parts of this thesis. Therefore, the different observational classes and suggested progenitor scenarios of supernovae as well as certain properties of supernova remnants are reviewed. Depending on their importance for the following chapters, the level of detail of the particular parts is accordingly adjusted and further information can be inferred from the given references.

1.1 Historical overview

Supernova (SN) explosions are among the most spectacular events that can be observed in the Universe. They mark the violent end of a star's life and lead to luminosities comparable to the brightness of a whole galaxy consisting of billions of stars (see Fig. 1.1). With rise times from several days to a few weeks and decline times of several months, the emission of these transient objects already fascinated people in antiquity. One of the earliest records of a stellar explosion can be found in the Chinese source *Hou Hanshu*, the "Book of the later Han", where the appearance of a "guest star" in the year 185 AD is mentioned (Stephenson & Green 2005). In the modern age, Tycho Brahe (1546-1601) and Johannes Kepler (1551-1630) were the first astronomers who studied local stellar explosions in greater detail. Brahe published the results of his observations of SN 1572 in the book *De nova* [...] *stella* ("On the new star"), providing the origin of the terminology of these events. The determination of the distance to the Andromeda nebula by Lundmark revealed that this nebula is in fact a galaxy situated outside of our Milky Way and led to the conclusion that the luminosity of a nova-like event observed in 1885 (S Andromaedae or SN 1885A in modern nomenclature) was three orders of magnitude higher than previously estimated (Lundmark 1920). In light of further discoveries of superluminous events and in order to distinguish those from much fainter classical novae, Baade and Zwicky introduced a new class of objects named *super-novae* (Baade & Zwicky 1934b). Additional observations of SNe in the following years enabled access to an understanding of the physical processes taking place in these violent explosions and first spectral analyses of the brightest SNe illustrated prominent observational differences. A classification scheme first introduced by Minkowski (1940) tried to cover these differences and has progressively been developed. Although still in use

Figure 1.1: Hubble Space Telescope image of supernova 1994D in galaxy NGC 4526 (Credit: NASA/ESA, The Hubble Key Project Team and The High-Z Supernova Search Team).

today, it more reflects an empirical differentiation between observations than being a link to the underlying explosion mechanisms, as described in the following section.

1.2 Supernova classification

The classification of SNe is mainly based on their early spectra in the optical wavelength regime at maximum light and therefore relies on the chemical and physical properties of the outermost layers of the ejected material. Due to the high velocities of the ejecta, the spectral lines are broad and often show P Cygni profiles formed by resonant scattering above the photosphere. Additionally, light curves and late time spectra are used to differentiate between several subtypes (see e.g. Filippenko 1997).

The current classification scheme is illustrated in Fig. 1.2. The two main classes are differentiated by the presence or absence of hydrogen in the spectra (cf. Fig. 1.3). While SNe of Type II show H lines, this is not the case for SNe of Type I. SNe of the subclass Type Ia are characterised by a strong Si II absorption feature around 6150 Å, SNe of Type Ib and Type Ic are distinguished by He I lines that are only present in the spectra of Type Ib. SNe of Type II are further subdivided depending on the shape of their light curves (SNe IIP exhibit a plateau of almost constant luminosity after maximum, the luminosity of SNe IIL declines linearly) or depending

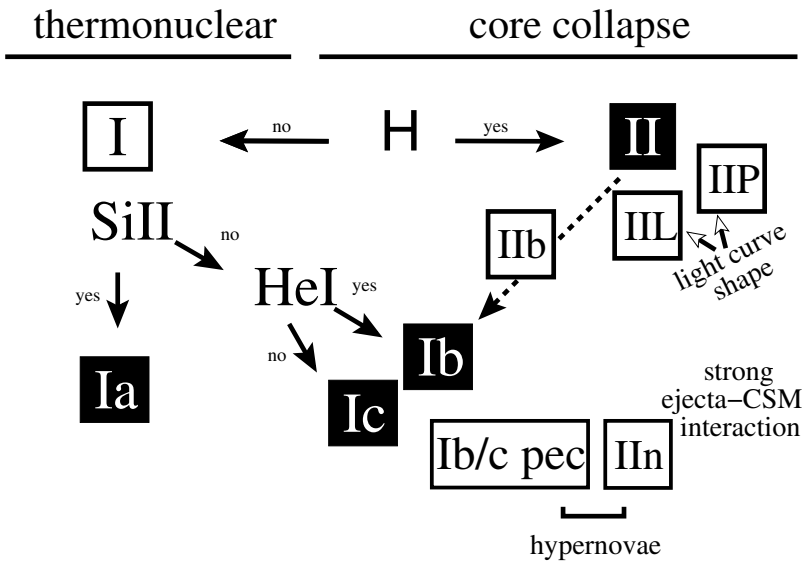

Figure 1.2: Classification scheme of SN explosions (taken from Turatto 2003).

on spectral characteristics (narrow hydrogen lines define the class of SNe IIn). SNe of Type IIb change their spectral properties with time. While the spectra at early times are similar to those of SNe II, the late time spectra are comparable to those of SNe Ib. The term "hypernova" is used for objects of Type Ib/c or IIn with explosion energies larger than $\sim 10^{52}$ erg.

In view of the enormous brightnesses of SNe, only the release of gravitational or nuclear binding energy provides a sufficient source to power these phenomena. Both possibilities seem to be realised in nature. SNe Ia are thought to be the thermonuclear explosions of electron-degenerate white dwarfs (WDs), a scenario first explored by Hoyle & Fowler (1960). The idea for the origin of all other types of SNe dates back to a suggestion by Zwicky and describes these events as the gravitational collapse of massive stars that have exhausted their nuclear fuel and turn into a neutron star or a black hole (Zwicky 1938). The two fundamentally different scenarios considered for the explanation of SNe are described in more detail in the subsequent two sections.

1.3 Type Ia supernovae

The following overview of observational properties and progenitor scenarios of SNe Ia is based on Filippenko (1997); Hillebrandt & Niemeyer (2000); Hillebrandt et al. (2013). For further details, the reader is referred to these publications and references therein.

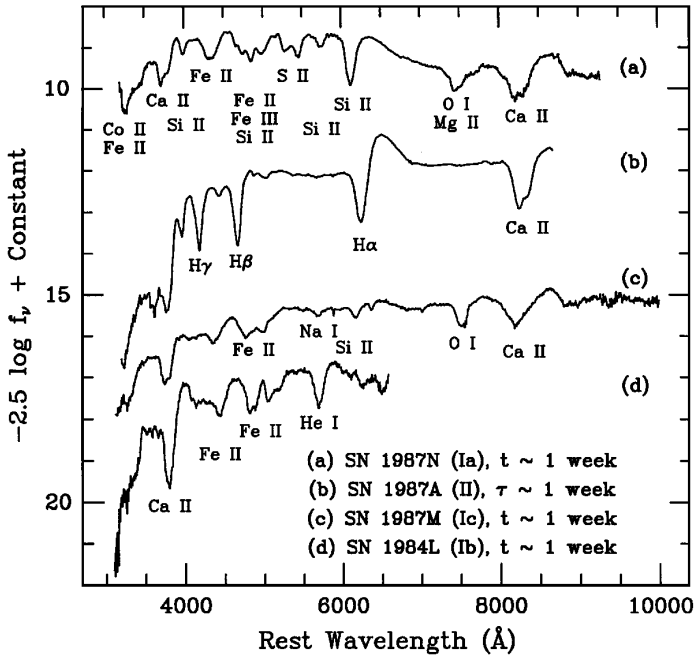

Figure 1.3: Early-time spectra of different SN types at roughly one week after B-band maximum (Type Ia) and core collapse (other types), respectively. For a better readability, the spectra have been shifted by a constant in y-direction (taken from Filippenko 1997).

1.3.1 Observational properties

Overall, SNe Ia show a very uniform behaviour regarding their light-curve shapes, spectral properties or absolute magnitudes. Following the results of a study by Li et al. (2011b), 77 % in a magnitude-limited sample and 70 % in a volume-limited sample of SNe Ia are fairly homogeneous and represent the class of "normal" SNe Ia.

At early times, the optical spectra of normal SNe Ia are characterised by broad peaks and troughs formed by lines of neutral and singly ionised intermediate-mass elements (IMEs, mainly O, Mg, Si, S, and Ca). Additionally, a small contribution of lines from iron group elements (IGEs) in weakly ionised states (Ni, Fe, Co) can be identified (see Fig. 1.3). The strongest features are Si II $\lambda\lambda$6347, 6371 and Ca II H&K $\lambda\lambda$3943, 3968 (Filippenko 1997). Since the ejected material expands and dilutes after the explosion, the temporal evolution of the spectra reflects the composition of the ejecta from the outmost layers (early time spectra, photospheric phase) to the innermost layers (late time spectra, nebular phase). Therefore, the early time spectra of SNe Ia give evidence that the outer layers mainly consist of IMEs. The blue shifts of the absorption component in the P Cygni profiles indicate that ejecta velocities up to $25,000\,\mathrm{km\,s^{-1}}$ can be reached. Different expansion velocities of different lines indicate a layered structure of the ejected material (e.g. Patat et al. 1996; Stehle et al. 2005; Hachinger et al. 2009). The amount of IGEs that contribute

to the spectra increases with time. Two weeks after peak brightness, the spectrum is already dominated by permitted lines of Fe II and only a small portion is made up by lines of IMEs. This is in line with the assumption of Fe-rich material in the central part of the ejecta (Harkness 1991). At roughly four weeks after maximum, the ejecta are completely optically thin and the nebular phase begins. Now, forbidden lines of Fe and Co are visible in the spectrum (Axelrod 1980).

The optical light curves of normal SNe Ia are believed to be powered by the decay energy of the radioactive isotope ^{56}Ni (Truran et al. 1967; Colgate & McKee 1969). They rise within a time of roughly 20 days, reach a maximum of $M_B \approx M_V \approx -19.3\,\mathrm{mag}$ (Hamuy et al. 1996) and then show a rapid decline of about three magnitudes in four weeks. Finally, they fade exponentially with approximately one magnitude per month. Together with the decrease of Co lines and the temporal changes in the intensity ratio of Co III and Fe III lines, this strongly supports the hypothesis that the light curve at late times is powered by the radioactive decay of ^{56}Co, an isotope that is part of the decay chain of the initially produced ^{56}Ni (Kuchner et al. 1994). The masses of ^{56}Ni can be inferred from the bolometric light curves and cover a range from $0.3\,\mathrm{M}_\odot$ to $0.9\,\mathrm{M}_\odot$ (cf. Stritzinger et al. 2006).

Despite the overall homogeneity of normal SNe Ia, spectroscopic and photometric differences still exist and prevent them being used as "standard candles" a priori. But the inhomogeneities of the observables are strongly intercorrelated (cf. Branch 1998): The weaker the explosions, the less luminous and the redder SNe Ia are. Furthermore, less energetic events exhibit faster declining light curves and slower ejecta velocities. Due to the correlations, SNe Ia can be used as "standardisable candles", which makes them an important tool for observational cosmology. Especially the fact that the light curves of more luminous SN Ia decline more slowly ("Phillips relation", Pskovskii 1977; Phillips 1993) is widely utilised as calibration procedure in cosmological surveys and allows to determine the absolute brightness of SNe Ia from their light curve shape (Leibundgut 2008; Goobar & Leibundgut 2011). Together with an independent determination of the redshifts, SNe Ia can be used as distance indicators probing the expansion history of the Universe (e.g. Riess et al. 1998; Perlmutter et al. 1999). The discovery that the Universe is in a state of accelerated expansion was awarded with the Nobel Prize in 2011.

Besides the class of normal SNe Ia, there are several subgroups of peculiar events that do not follow the above mentioned correlations (see Fig. 1.4). SN 1991bg-like objects are fainter than normal SNe Ia by roughly one magnitude, their light curves decline rapidly and the total mass of ^{56}Ni produced during the explosion is very low ($\sim 0.1\,\mathrm{M}_\odot$, Mazzali et al. 1997). Their spectra give evidence for large amounts of IMEs at low velocities and, according to Li et al. (2011b), about 15 % of all SNe Ia are members of this subgroup. Another subgroup of subluminous events ($\sim 5\,\%$ of all SNe Ia, Li et al. 2011b) is represented by SN 2002cx. Characteristic properties of these peculiar SNe are low ^{56}Ni masses, low ejecta velocities, low kinetic energies, and almost featureless spectra around peak luminosity (Li et al. 2003; Jha et al. 2006). The nebular phase is reached at very late times, even at 300 days after the

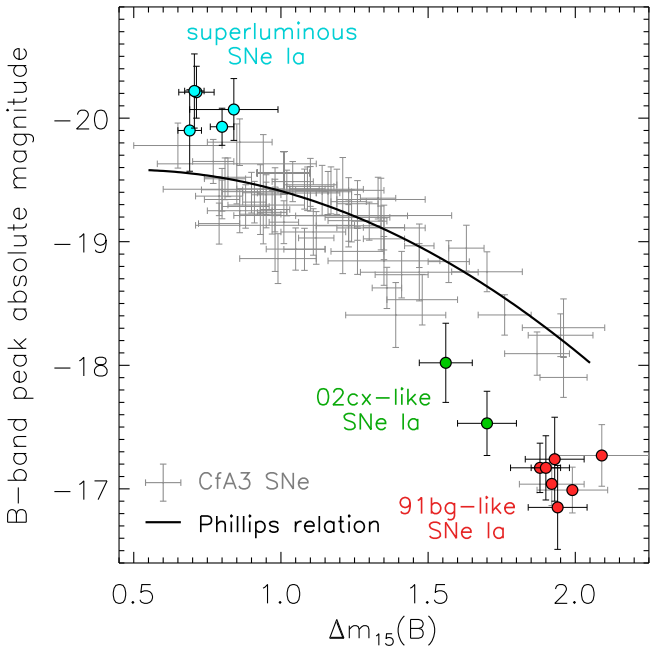

Figure 1.4: Observational diversity of SNe Ia, the B-band peak absolute magnitude is plotted against the B-band decline rate $\Delta m_{15}(B)$ that compares the maximum B-band luminosity to the B-band value 15 days after maximum. The subgroups described in the text are indicated with different colours, normal SNe Ia following the Philips relation are shown in grey (taken from Hillebrandt et al. 2013).

explosion, the ejecta are not totally diluted (Jha et al. 2006). The group of SN 1991T-like objects ($\sim 9\,\%$ of all SNe Ia, Li et al. 2011b) is slightly brighter than the brightest normal SNe Ia and their early spectra show Fe III lines (Phillips et al. 1992; Mazzali et al. 1995). At later times, their spectra are comparable to those of normal SNe Ia. Even SNe with luminosities that are two to three times higher than the bright end of the Philipps relation have been found (Howell et al. 2006; Yamanaka et al. 2009; Taubenberger et al. 2011). Their light curves exhibit longer rise times and slower declines than normal SNe Ia, their spectra indicate lower ejecta velocities and present prominent C II absorption features. If the luminosity in total is attributed to the radioactive decay of ^{56}Ni, the needed ^{56}Ni mass can exceed the Chandrasekhar mass limit (Howell et al. 2006; Taubenberger et al. 2011; Kamiya et al. 2012).

1.3.2 Progenitor scenarios

Nowadays, it is commonly believed that SNe Ia result from thermonuclear explosions of WDs, as already suggested by Hoyle & Fowler (1960). There has not been a direct detection of a progenitor system of SNe Ia yet, but this proposition is supported

by several arguments. SNe Ia are found in galaxies of all types and likewise in old and young stellar populations. Compact objects as remnants of the explosions have not been observed. This precludes the death of massive stars (see also Section 1.4) from being the origin of these explosions. Additionally, the absence of significant contributions of H and He in the spectra points towards an evolved progenitor that has already lost its envelope and is not able to produce large amounts of circumstellar material by stellar winds or common envelope phases. Due to the lack of radio or X-ray emission from the sites of SNe Ia before the explosion, neutron stars and black holes can also be excluded. These constraints strongly favour WDs as progenitors of SNe Ia.

There are three different types of WDs that can be distinguished by their chemical composition: WDs mainly comprised of He, of C and O or of O and Ne (Livio 2000). In the first case, initial WD masses cannot be larger than $\sim 0.45\,\mathrm{M}_\odot$ (Iben & Tutukov 1985), otherwise He burning would immediately start in the core. Furthermore, the ejecta of an exploding He WD only consist of He and ^{56}Ni and do not accommodate for the spectral signatures of IMEs in SNe Ia (Nomoto & Sugimoto 1977; Woosley et al. 1986). Therefore He WDs can be excluded as progenitor candidates. O/Ne WDs are rather supposed to collapse to a neutron star than to explode when they are ignited (Saio & Nomoto 1985; Nomoto & Kondo 1991; Gutierrez et al. 1996), but a minor contribution of these WDs to the zoo of SNe Ia is not completely ruled out. This leaves C/O WDs as the most promising candidates for the majority of SNe Ia.

Since most C/O WDs are born with a mass of about $0.6\,\mathrm{M}_\odot$ (Weidemann & Koester 1983; Homeier et al. 1998), they are far below the Chandrasekhar mass limit of $\sim 1.4\,\mathrm{M}_\odot$ (Chandrasekhar 1931). Being otherwise stable for all times, the WD has to interact with a companion star in a binary system in such a way that mass transfer finally causes an explosion. In general, two different kinds of progenitor scenarios are distinguished by the nature of the companion star: the *single-degenerate* (Whelan & Iben 1973) and the *double-degenerate* scenario (Webbink 1984; Iben & Tutukov 1984). While in the first scenario the WD accretes mass from a main sequence star, a helium star or a red giant, the second scenario describes the case of a likewise degenerate companion, a C/O or a He WD.

The *single-degenerate* scenario can further be subdivided into two different model classes: the Chandrasekhar mass models and the sub-Chandrasekhar mass models. According to the most broadly discussed Chandrasekhar mass models, the C/O WD increases its mass by accretion through Roche-lobe overflow or through stellar winds. Shortly before the Chandrasekhar mass limit is reached, the temperature and density conditions in the centre of the WD lead to a thermonuclear runaway and a complete disruption of the star. Therefore, the homogeneity of SNe Ia can quite naturally be ascribed to the mass limit of the WDs.

Thermonuclear burning can propagate as supersonic detonation or subsonic deflagration flame. Detonations do not allow the WD material to expand before the burning

takes place since there is no causal contact between the energy release and the fuel in front of the combustion wave. In contrast to observations (see Subsection 1.3.1), the high initial densities of a Chandrasekhar mass WD in hydrostatic equilibrium lead to burning products that mainly consist of iron group elements (predominantly ^{56}Ni). This is why prompt detonations of Chandrasekhar mass WDs can be excluded as SNe Ia explosion model. Deflagration flames allow for a pre-expansion of the fuel and IMEs can also be synthesised, but even in optimistic cases with strong ignition conditions, only $\sim 0.3\,\mathrm{M}_\odot$ of ^{56}Ni can be produced (cf. Röpke et al. 2007). Additionally, strong chemical mixing effects due to buoyancy instabilities are visible in the spectra and lead to the conclusion that pure deflagrations cannot account for the class of normal SNe Ia, whereas peculiar subclasses might be explained by such a scenario (see e.g. Fink et al. 2013).

Within the framework of Chandrasekhar mass models, a successful description of normal SNe Ia requires a transition from an initial deflagration to a detonation wave at later times. Due to the pre-expansion during the deflagration phase, the detonation occurs at lower densities and can produce a substantial amount of IMEs in the outer layers of the WD. Thus, a chemical stratification of the ejecta similar to that inferred from optical spectra of normal SNe Ia can be realised. There are different suggestions how the transition between different burning modes can take place. One possibility is the so-called delayed-detonation model where turbulent mixing of fuel and ashes gives rise to the formation of a detonation (Khokhlov 1991). The total production of ^{56}Ni is determined by the initial ignition conditions and the resulting strength of the deflagration phase, because a larger pre-expansion leads to lower densities and a production of less ^{56}Ni in the detonation phase (see e.g. Mazzali et al. 2007). So the delayed-detonation model can in principle account for the spread of ^{56}Ni masses and brightnesses of normal SNe Ia. Besides the delayed-detonation model, alternative scenarios have been suggested that are also based on an initial deflagration phase and a subsequent detonation in a pre-expanded medium. These include the gravitationally confined detonation models (Plewa et al. 2004; Jordan et al. 2008; Meakin et al. 2009) and the pulsational (reverse) detonation models (Arnett & Livne 1994a,b; Bravo & García-Senz 2006) where different mechanisms for the triggering of the detonation are suggested. For further details, the reader is referred to the given references.

But this model also has drawbacks that do not seem to have been fully resolved up to now: When the WD accretes H or He from its companion star, the material is burned to C on the surface and the total mass of the C/O WD increases. In order to get stable surface burning conditions, the accretion rate is constrained to a small parameter range. While too low accretion rates are thought to lead to nova-like events, in which most of the accreted material is blown away (Townsley & Bildsten 2005), too high accretion rates can cause an expansion of the WD to a red giant-like object. Therefore mechanisms for a self-regulated accretion seem to be a necessary ingredient of Chandrasekhar mass models (Hachisu et al. 1999), and questions about the required level of fine-tuning in these models arise quite naturally

(e.g. Cassisi et al. 1998; Woosley & Kasen 2011). Furthermore, there is also debate about whether WDs with stable nuclear burning on the surface should be visible as super-soft X-ray sources or not (Di Stefano 2010; Gilfanov & Bogdán 2010, but see also Hachisu et al. 2010; Meng & Yang 2011).

An alternative to the deflagration-to-detonation transition in a Chandrasekhar mass WD is a detonation in a sub-Chandrasekhar mass WD, since the prevailing densities in these objects are lower and IMEs can be produced sufficiently (see e.g. Woosley & Weaver 1994; Livne & Arnett 1995). According to this model, accretion of He from a He star or a He WD generates a layer of He on the C/O WD. If the layer becomes massive enough, a detonation is induced by compressional heating. By sweeping around the C/O core and burning the He to heavier elements, this shock wave is thought to trigger another detonation at the interface to the C/O core or after converging at the centre of the WD. The secondary detonation burns the entire WD in a thermonuclear runaway. Since more massive C/O WDs contain more material at higher densities leading to higher abundances of ^{56}Ni in the burning processes, also this model can naturally account for the brightness distribution of normal SNe Ia. Problems arise due to the burning in the He shell. Depending on the mass of He and the resulting densities, significant amounts of IGEs can be produced there resulting in peculiar spectral features that are not observed. Although these problems can partially be circumvented by reducing the He mass in the outer layer, the simulated spectra still show differences compared to the spectra of normal SNe Ia (Fink et al. 2010; Kromer et al. 2010).

Studies concerning the expected signatures of the single-degenerate scenario have been inconclusive up to now, examples are searches for wind-blown cavities from the earlier accretion phases (e.g. Badenes et al. 2007, but see also Williams et al. 2011) or for the surviving companion (e.g. Ruiz-Lapuente et al. 2004, but see also Kerzendorf et al. 2009). Attempts to identify fingerprints from the interaction of the explosion shock waves with the donor star or its circumstellar winds could only place upper limits and present challenges for the single-degenerate scenario. Studies of SN 2011fe, a recent SN Ia in M101 observed with unprecedented coverage in many wavelength bands from very early times on, excluded red giants and most main-sequence stars more massive than the Sun as a possible companion star (Li et al. 2011a; Nugent et al. 2011; Brown et al. 2012; Bloom et al. 2012).

In the *double-degenerate* scenario, two WDs closely orbiting each other lose energy and angular momentum due to the emission of gravitational waves and finally merge. A robust mechanism leading to a thermonuclear explosion is described in the so-called "violent merger" model (Pakmor et al. 2010). Starting from a binary system of WDs with a mass ratio close to unity, the less massive secondary WD is deformed by tidal interactions and finally plunges into the primary WD. During this violent merger, a hot spot with adequate thermodynamic conditions for the initiation of a detonation is formed. The density structure of the primary WD is more or less unaffected by the infalling material and the burning takes place at conditions comparable to those of normal sub-Chandrasekhar mass explosions (see above). The prevailing

densities of the primary WD are high enough to produce IGEs, the remainder of the secondary WD is mostly burned to O. Although the total mass of the merged and exploding object is quite large, violent mergers of WDs can reproduce fundamental characteristics of light curves and spectra of normal SNe Ia (Pakmor et al. 2012b). The brightness distribution of normal SNe Ia can be covered by binary systems of WDs with different masses (Ruiter et al. 2013).

The double-degenerate scenario is also debated: Arguments that the merger of two unequal-mass WDs should cause an accretion-induced collapse and a subsequent formation of a neutron star seem to be not valid for the violent merger model (Pakmor et al. 2010), but the robustness of the mechanism that leads to a detonation during the merger process still has to be investigated. From an observational point of view, it is quite difficult to conclusively verify or falsify the double-degenerate scenario, since, by the way the model is constructed, it eludes direct observations to a certain degree. Although measurements of SNe Ia delay-time distributions (the distribution of times after that progenitor systems of SNe Ia explode following a burst of star formation) appear to support the double-degenerate model (Mennekens et al. 2010; Ruiter et al. 2011; Toonen et al. 2012), detailed population synthesis calculations deliver different results concerning the question whether the measured SNe Ia rates are in line with the predictions of the single- or double-degenerate scenario (Maoz & Mannucci 2012, but see also the recent suggestion of He-ignited violent mergers by Pakmor et al. 2013). Furthermore, it is still unclear if the amount of observed WD binaries in the solar neighbourhood can account for a sufficient number of mergers within a Hubble time (e.g. Nelemans et al. 2005, but see Geier et al. 2010).

The current status of suggested progenitor models for SNe Ia explosions can be summarised as follows. In view of the diversity of SNe Ia events that has been revealed especially by observations in recent years, an explanation of all SNe Ia by one explosion scenario seems to be out of reach (Wang & Han 2012). The questions regarding the number of contributing progenitor models and the dominating explosion channel(s) still remain to be answered. Some current three-dimensional models produce spectra and light curves that are quite similar to the observed ones, in spite of the uncertainties in certain model aspects (exact initial conditions, treatment of detailed combustion physics, etc.) that still have to be removed. The difficulty of judging the models by comparing them to observations arises due to the fact that the simulated observables show a huge degeneracy (e.g. Röpke et al. 2012). Concerning, for example, the delayed-detonation Chandrasekhar mass models, the sub-Chandrasekhar mass models and the violent merger models, their main differences become apparent in the total mass of the ejecta and the amounts of unburnt C and O. But owing to the low opacities caused by these two elements, their influence on light curves and spectra is only marginal. The characteristic features of SNe Ia observables are mostly determined by the abundance distributions of IMEs and ^{56}Ni in the ejecta, and just these properties of the respective explosion models appear not to be distinct enough to disentangle them easily.

The apparent degeneracy of different progenitor scenarios concerning their observables is further discussed in Chapters 3 and 4. There it is shown that especially high-energy observables in the gamma and X-ray regime are well-suited for differentiating between certain explosion models, and observation strategies that can reveal these special characteristics are addressed.

1.4 Core-collapse supernovae

Besides SNe Ia, all other classes of SNe (Type II, Ib, Ic, etc.) are believed to result from the collapse of a massive star ($M \gtrsim 8\,\mathrm{M}_\odot$) to a neutron star or a black hole. This marks the end of several evolutionary phases the star has passed through (cf. Woosley et al. 2002; Janka 2012).

In general, stellar evolution can be thought of as an on-going contraction that is partially interrupted by phases of nuclear fusion. In the first and longest lasting thermonuclear stage, fusion of H into He takes place in the hot stellar core. After the exhaustion of H in the innermost regions of the star, H burning still proceeds in the outer shells. The fact that energy losses due to neutrinos become much more important than radiation losses leads to a decoupling of the He core from the stellar envelope. Because of the termination of the energy supply by nuclear burning in the core, gravity forces the star to contract. If the critical temperature for the initiation of the next burning stage is reached before the stellar interior is dominated by electron degeneracy pressure, nuclear fusion starts again[1]. Otherwise the final state of the stellar core is a WD that cools without further contraction and is stabilised by the pressure of degenerate fermions. The outer envelope is blown away and can be observed as so-called planetary nebula.

As more massive stars with correspondingly larger cores can achieve higher temperatures in the centre, the evolution of a star is totally determined by its initial mass (see Fig. 1.5). All further fusion stages after H burning (He, C, Ne, O, and Si fusion) proceed on significantly shorter time scales since the efficiency of energy production reduces. At the end of its thermonuclear life, the star exhibits an onion-skin structure with a core of O/Ne/Mg or Fe, the outer shells consist of elements with progressively lower atomic weights at decreasing temperatures and densities. Due to shell burning, the mass in the core continuously grows by mass accretion until it cannot be supported against collapse by degeneracy pressure any longer. Depending on the star's birth mass, three different processes can cause gravitational instabilities that finally lead to an implosion of the stellar core: electron capture, photodissociation, and pair production (see Fig. 1.5).

The progenitors of core-collapse SNe with the lowest masses do not reach the Ne burning phase because electron degeneracy sets in before (Nomoto 1984, see also

[1]Properties of burning processes under degenerate conditions (for example the so-called central He flash in the cores of red giants) are not considered here. The reader is referred to the corresponding literature (e.g. Padmanabhan 2001).

Fig. 1.5). Due to the increasing Fermi energy and the relatively low reaction thresholds in the O/Ne/Mg core, electron captures on Ne and Mg reduce the degeneracy pressure and a gravitational collapse is unavoidable. When nuclear densities ($\rho \gtrsim 2.7 \times 10^{14}\,\mathrm{g\,cm^{-3}}$) are reached, the dynamical collapse is immediately stopped by the repulsive short-range forces between nuclei. The inner core rebounds into the supersonically infalling layers, a shock front forms and disrupts the star in the SN explosion. According to Wanajo et al. (2009), these so-called electron-capture SNe constitute up to 30 % of all SNe. Because of an extremely steep density gradient in the regions around the core, the mass accretion rate from the outer shells onto the core decreases rapidly in these explosion scenarios. The ejecta contain only small amounts of ^{56}Ni, SNe of this class are therefore very faint (Janka 2012).

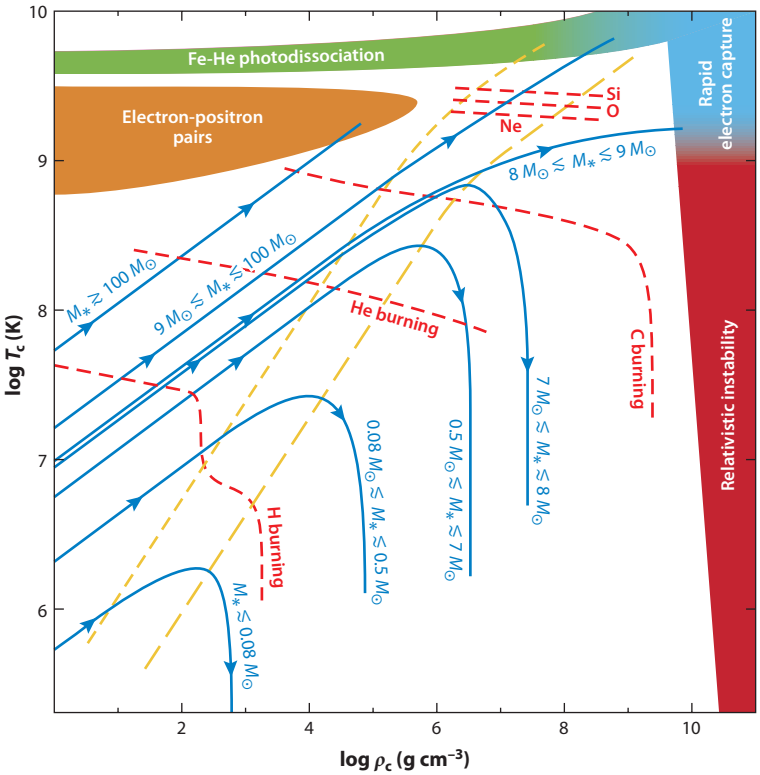

Figure 1.5: Schematic representation of stellar evolutionary tracks (in blue, the approximate birth-mass range necessary to reach the different burning stages is also given) in the plane of central density and temperature. In reality, stellar tracks show additional wiggles and loops that are caused by the star's readjustment at the beginning of new burning stages. The threshold values for H, He, C, Ne, O, and Si burning are marked in red, the diagonal yellow lines indicate the beginning of electron degeneracy (short-dashed) and the onset of strong degeneracy (long-dashed) towards higher densities. The coloured regions mark the different "death zones" where gravitational collapse is unavoidable (taken from Janka 2012).

Stars that are massive enough to initiate Ne burning finally build up an Fe core. If the temperature exceeds 10^{10} K, photodissociation of heavy nuclei into alpha particles and free nucleons destabilises the core (see Fig. 1.5) and, together with the onset of additional electron captures on heavy nuclei and free protons, the collapse is further accelerated. In contrast to the previous O/Ne/Mg core scenario, the much flatter density profile outside the Fe core leads to a very efficient mass accretion from the infalling shells. The pressure that is associated with the accretion processes obstructs the outward moving shock front and makes the realisation of a successful explosion more difficult (Janka et al. 2012).

The detailed explosion mechanisms of core-collapse SNe are still subject to current research (cf. Janka 2012). After rebound, the shock moves through the overlying Fe-core material and loses energy due to the dissociation of Fe-group nuclei into free nucleons. It is further damped by the pressure of the infalling material and finally develops into a quasi-stationary accretion shock (see Fig. 1.6). Therefore, a successful explosion requires a revival of the shock by additional processes. One suggestion is the so-called delayed neutrino-driven explosion mechanism (Bethe & Wilson 1985). Neutrinos are numerously produced in the forming proto-neutron star and only a small fraction of the energy that is radiated away by neutrinos ($\sim 10^{53}$ erg) is needed to account for the observed kinetic energies of a canonical Type II supernova ($\sim 10^{51}$ erg, Janka et al. 2012). According to this mechanism, the deposition of energy by neutrinos behind the shock can lead to a re-acceleration of the shock front. The neutrino luminosity that is necessary to reach the conditions for a runaway depends on the mass accretion rate and the mass of the proto-neutron star. On the one hand, the neutrino heating has to compete with the ram pressure of the accreted material, on the other hand, it has to overcome the gravitational potential energy of the nascent neutron star. Recent results of computer simulations show that multi-dimensional flows are especially important for successful explosions of more massive Fe-core progenitors. The efficiency of the neutrino heating mechanism crucially relies on non-radial hydrodynamical instabilities such as convective overturn (Herant et al. 1994) or the standing accretion shock instability (SASI, Blondin et al. 2003). But also the influence of different mechanisms with respect to the dimensionality of current explosion models (i.e. 2D vs. 3D) is still a matter of debate and many dynamical phenomena that may be important in neutrino-heated supernova cores remain to be studied (Janka 2012).

After the re-acceleration of the shock wave, radioactive species like ^{56}Ni are produced by explosive burning in the shock-heated outer layers of Si or O (see Fig. 1.6). The nucleosynthetic yields are further influenced by recombination processes of nucleons in the rising bubbles of neutrino-heated ejecta. Additionally, a neutrino-driven baryonic outflow (a so-called neutrino wind) that arises from the surface of the neutron star is thought to be a possible site of r-process nucleosynthesis where heavier nuclei up to $A \sim 110$ could be formed. But it is still not clear if the essential conditions for r-processes (sufficiently high entropy and sufficiently large neutron excess) can be realised in these neutrino winds (Arcones & Thielemann 2013).

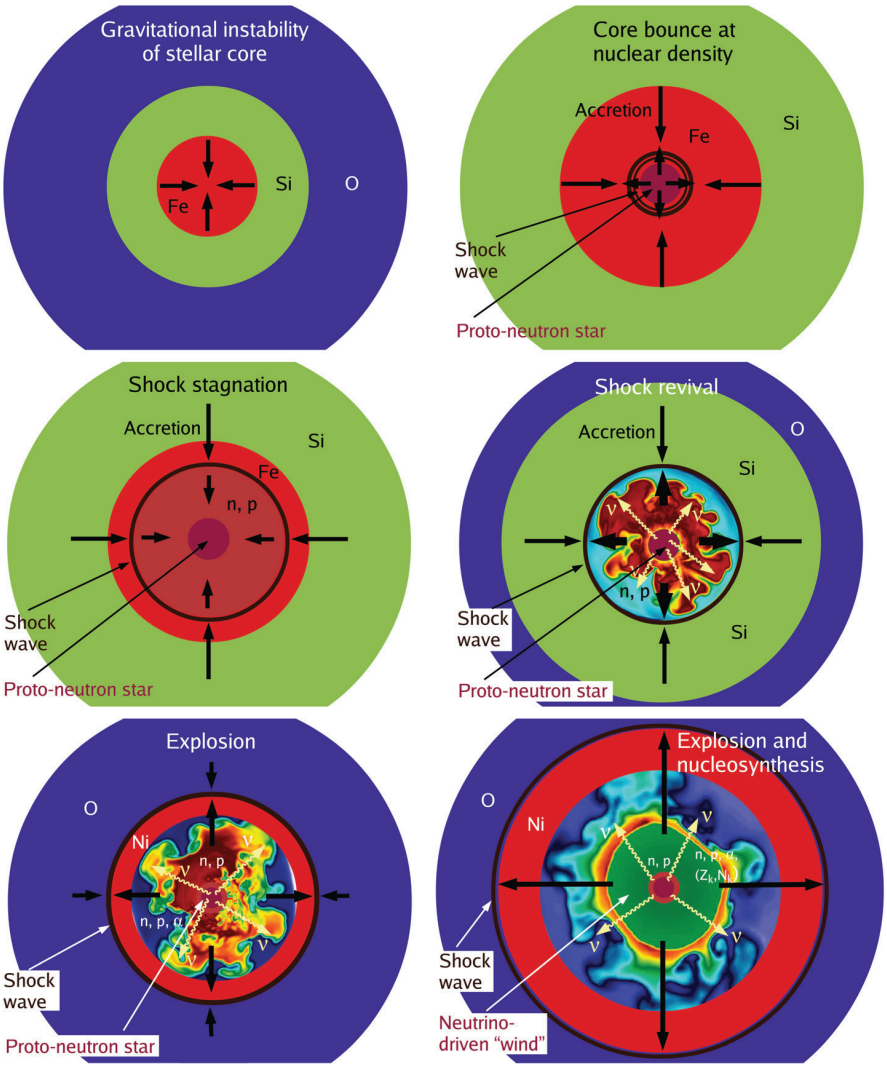

Figure 1.6: Schematic overview on evolutionary stages of core-collapse SNe from the beginning of the gravitational implosion (top left), through the formation and revival of the shock (middle panel) to the final explosion (bottom right, taken from Janka et al. 2012).

Stars with masses above $\sim 100\,M_\odot$ (see Fig. 1.5) become gravitationally unstable because of pair production processes soon after central C burning (pair-instability SNe, e.g. Woosley et al. 2002). Due to the prevailing high temperatures, conversion processes from photons to e^+e^--pairs transform thermal energy into rest-mass energy and the reduction of pressure support causes gravitational instability. For stellar masses between $\sim 100\,M_\odot$ and $\sim 140\,M_\odot$ as well as above $\sim 260\,M_\odot$, the final state after collapse is believed to be a black hole. In the mass ranges in between, violent thermonuclear burning produces enough energy to totally disrupt the star during the implosion. Explosion energies up to 10^{53} erg can be reached and the

production of more than $50\,M_\odot$ of ^{56}Ni is possible within these burning processes (Heger et al. 2003). But also strong interactions between the ejected material and a very dense circumstellar medium could be responsible for the extreme brightness of some recently discovered SNe (Woosley et al. 2007) and the question concerning the energy source of these superluminous events still remains to be solved.

Due to efficient mechanisms of angular momentum losses that come along with the mass losses during the red giant phase of a star (Heger et al. 2005), normal core-collapse SNe do not seem to be influenced very strongly by rotational effects. This is different for gamma-ray burst (GRB) SNe and Hypernovae (HNe) where stellar rotation is thought to be an important ingredient (cf. Woosley & Bloom 2006). In contrast to pair-instability SNe (and to earlier definitions), today the term HN is identified with stellar explosions that present very broad spectral lines and therefore high ejecta velocities (Iwamoto et al. 1998). HNe are often accompanied by GRBs, this connection can be validated spectroscopically and becomes apparent in a second light curve peak in the overall power-law decline of the GRB afterglow. Different scenarios are suggested for the explanation of GRBs and HNe (cf. Janka 2012). Stellar collapses that form rapidly spinning black holes with strong neutrino and electromagnetic Poynting fluxes or fast rotating neutron stars with very strong magnetic fields may be the sources of these peculiar SNe. The rotational energy of the neutron star or the gravitational and rotational energy of the accretion flow onto the black hole could provide enough resources to power the stellar explosion and the jet-like relativistic outflows associated with GRBs. The neutron star as well as the black hole scenario put strong constraints on the progenitor scenario. Although rapidly rotating Wolf-Rayet stars seem to be the preferred candidates, high initial spins and mechanisms that prevent the star from losing mass and angular momentum simultaneously (see above) are needed (e.g. Yoon & Langer 2005; Woosley & Heger 2006).

The preceding section about core-collapse SNe focuses on the theoretical foundations of these events. Further information about the status of current multi-dimensional simulations can be found in Janka (2012) and Janka et al. (2012). For more details on the relation between different progenitors and the spectral classes of core-collapse SNe introduced in Section 1.2, the reader may refer to Smartt (2009).

1.5 Supernova remnants

In addition to direct studies of SN explosions, observations of SN remnants (SNRs) can provide further insights into nucleosynthesis yields and explosion physics of SNe. Due to the interaction of SN ejecta with the circumstellar medium (CSM), SNRs are also well-suited for getting information about the closest surroundings of SNe. These ambient regions are influenced by the progenitor systems prior to the explosion and therefore allow conclusions on the SN progenitors themselves. Another property of SNRs that is investigated in detail in Chapter 2 is the existence

of high-Mach number collisionless shocks. Because of ambient media of rather low densities, shock heating is caused by plasma waves and electromagnetic fluctuations instead of particle-particle interactions. The presence of these shocks makes SNRs to preferred sites for the acceleration of particles. This assumption is supported by observations of synchrotron emission from the radio to the X-ray regime and high-energy gamma-ray emission in case of several SNRs, where the former is indicative of the existence of relativistic electrons and the latter points towards populations of accelerated electrons and ions (Reynolds 2008). Especially the emission of gamma-rays in the MeV energy range turns out to be a useful diagnostic tool for cosmic ray acceleration processes and is further discussed in Chapter 2.

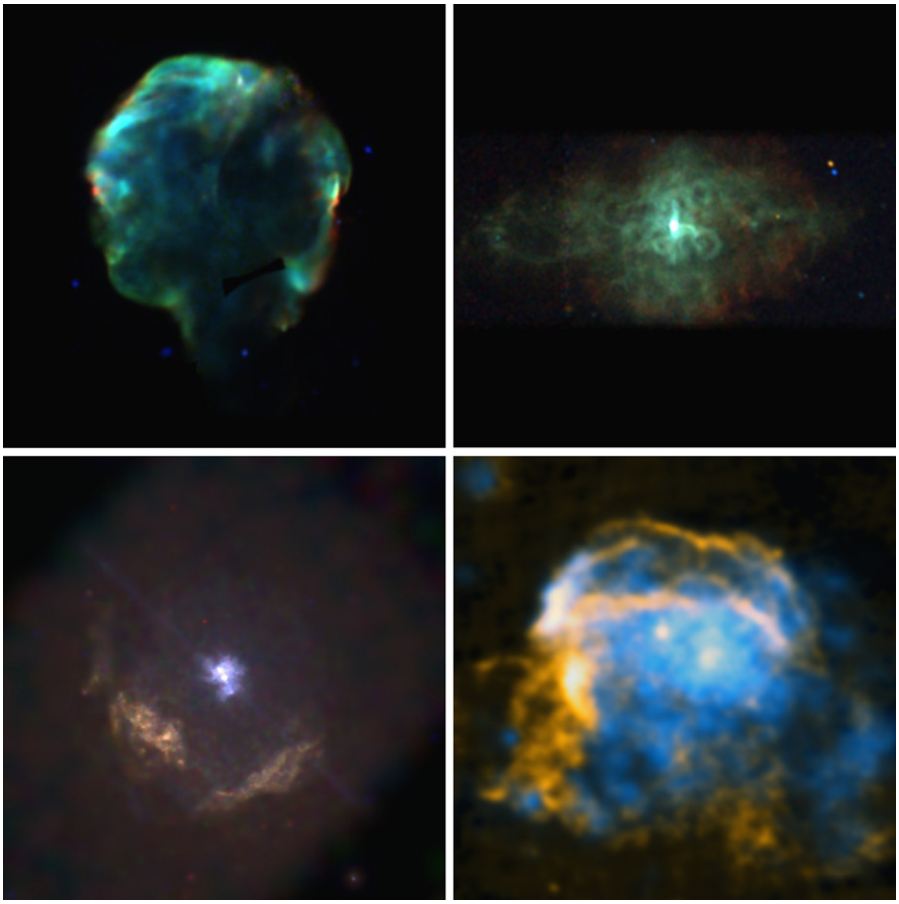

Figure 1.7: Examples of different types of SNRs (taken from Vink 2012). The top row depicts the Cygnus loop (ROSAT, Levenson et al. 1998), a *shell-type* SNR, and 3C58 (Chandra, Slane et al. 2004), a *plerion/pulsar wind nebula*, from left to right. The bottom row shows the *composite* SNR Kes 75 (Chandra, Helfand et al. 2003) with the inner pulsar wind nebula and the outer partial shell on the left, and W28 (X-ray data (ROSAT) in blue, radio data (VLA) in orange, Dubner et al. 2000), a *thermal-composite* SNR, is displayed on the right.

1.5.1 Classification of supernova remnants

Although it would be desirable to classify all SNRs by means of the above defined explosion types (see Section 1.2), especially the emission of old SNRs is mainly caused by the swept-up and shock-heated ambient material and the SN origin cannot easily be determined. This is why an additional classification of SNRs exists that mostly relies on their morphology (Vink 2012). A distinction is made between three different classes: *shell-type* SNRs, *plerions*, and *composite* SNRs (see Fig. 1.7).

Many SNRs are assigned to the first class, since a shell of shock-heated plasma created by the SN blast wave (see Subsection 1.5.2) can often be identified. In case of core-collapse events with rapidly rotating neutron stars (so-called pulsars) as remnants, other morphologies are observed. The energy losses of the rotating neutron star lead to the production of a wind of relativistic electrons and positrons that are further accelerated to ultra-relativistic energies at the wind's termination shock. The relativistic particles form a so-called pulsar wind nebula and emit synchrotron radiation (radio to soft gamma-ray energies) that can be further upscattered to TeV energies by inverse-Compton processes (Gaensler & Slane 2006). Being very bright in the centre and not exhibiting a prominent shell, these SNRs are also called *filled-centre* SNRs or *plerions* (Weiler & Panagia 1978). Although the terms "pulsar wind nebula" and "plerion" are often used interchangeably, especially the remnants with older pulsars that do not show signs of recent supernova activity any more should preferably be named pulsar wind nebulae. Pulsar wind nebulae that are still surrounded by a SNR shell can often be found in case of young pulsars. SNRs with this characteristic morphology are termed *composite* SNRs. Some SNRs that are not additionally powered by a pulsar show an ambivalent structure. While the radio emission indicates a shell-type morphology, the X-ray emission mainly originates from hot plasma in the centre. These SNRs are denoted as *mixed-morphology* or *thermal-composite* SNRs (Rho & Petre 1998; Shelton et al. 1999). For further information about the different characteristics of SNRs and their connection to the different explosion types, the reader is referred to the review of Vink (2012) and references therein.

1.5.2 Evolutionary stages of supernova remnants

The evolution of SNRs is commonly subdivided into several distinct stages (cf. Chevalier 1977; Reynolds 2008; Vink 2012). In the following, the different phases and their characteristic properties are introduced, but the reader has to note that these phases are just a simplified description, into which not all SNRs can easily be categorised.

In phase 1, the mass of the SN ejecta (M_{ej}) is larger than the mass of the swept-up ambient material (M_{sw}). The characteristic explosion velocities of order $10^4\,\mathrm{km\,s^{-1}}$ for SNe Ia and $5000\,\mathrm{km\,s^{-1}}$ for core-collapse SNe are significantly higher than the

prevailing sound speeds in the CSM of roughly $1\,\mathrm{km\,s^{-1}}$ to $10\,\mathrm{km\,s^{-1}}$. This causes the formation of a blast wave that easily reaches Mach numbers of $M \gtrsim 10^3$ (Reynolds 2008). Although this ejecta-dominated phase is often referred to as "free expansion phase", the shock velocity v_s is always smaller than in a real free expansion and the relation $v_s < r_s/t$ with the radius of the outer shock r_s holds. Behind the blast wave ("forward shock"), the ejecta undergo adiabatic cooling. Due to the interaction of the forward shock with the CSM and the associated progressing deceleration, the succeeding parts of the interior ejecta have to slow down abruptly and a so-called "reverse shock" builds up that expands back into the ejecta (from a Langrangian point of view) and reheats them. Both shocks move outwards in radius at early times. Because of the higher densities in the ejecta, the velocity of the reverse shock is usually lower than the velocity of the forward shock. The decrease of ejecta densities during the expansion leads to a "turn over" and the reverse shock starts to move inwards in radius at later times, too (see Fig. 1.8). A contact discontinuity separates the forward shock-heated CSM from the reverse shock-heated ejecta. This surface with discontinuities in mass density and temperature is subject to Rayleigh-Taylor instabilities, and strong turbulence can cause a mixture of shocked ejecta material with the shocked CSM. Depending on the density profile of the ambient medium and the ejecta, the described two-shock structure can persist for hundreds to thousands of years. While the reverse shock might disappear in the centre of the remnant after reheating all the ejecta in situations of perfect spherical symmetry, realistic hydrodynamic simulations usually show reverberations and longer lasting reverse shock modes (cf. Reynolds 2008).

In the subsequent Sedov-Taylor phase, M_{sw} is larger than M_{ej} and radiative losses are negligible. Although the second phase is often called the "adiabatic phase", this term would also be appropriate for the first phase since energy losses are usually not important in phases 1 and 2. But it has to be noted that despite the relative unimportance of radiative losses concerning the total energy budget in the first two evolutionary phases of SNRs, the resulting emission is nevertheless of great observational interest. One example that focuses on the diagnostic value of X-ray lines occurring in SNe Ia remnants is presented in Chapter 4. When all the ejecta have been shocked and the reverberations of the reverse shock have effectively ceased to exist, the SNR evolution can be described by a self-similar one-shock solution (Taylor 1950; Sedov 1959). According to one-dimensional hydrodynamic simulations, the swept-up mass has to be several times larger than the ejected mass until the transition to the Sedov-Taylor stage has been reached. This happens when the expansion parameter $m \equiv v_s t/r_s$ reaches a value of 0.4 (see Fig. 1.8 and Reynolds 2008). SNRs that are in phase 1 or at the beginning of phase 2 are often termed "young" SNRs in the literature.

In phase 3, the "snowplough" phase, the shock velocity is slow enough so that the cooling time scale of the material behind the shock is smaller than the flow time scale. Radiative cooling becomes dynamically significant and the adiabatic approximation does not hold any longer. Due to the radiation losses in the shell of swept-up

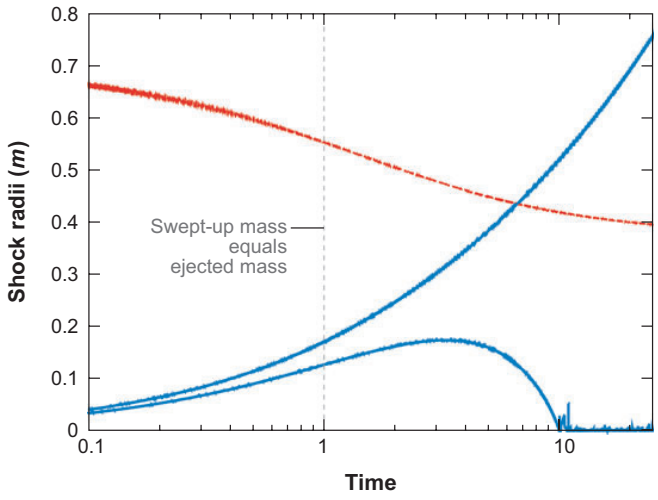

Figure 1.8: Results of a one-dimensional hydrodynamic SNR simulation of the evolution of the radius of forward (upper blue line) and reverse shock (lower blue line), using the harmonic-mean density profile according to Truelove & McKee (1999). The expansion parameter m is also given (red line). The Sedov-Taylor phase is reached at a value of $m = 0.4$ after a gradual transition. Note that the swept-up mass equals the ejected mass much earlier (taken from Reynolds 2008).

material, the shell collapses to a thin and dense layer while the temperature and the pressure in the interior of the SNR still remain high. The further expansion of the shell is pressure-driven and the ambient material is collected as if it was done by a snowplough. If the interior is able to cool, the internal pressure diminishes and the dense shell expands in a momentum-conserving way. Depending on the complexity of the density structure a SNR is evolving into, different parts of a SNR can be in different phases. In regions of higher ambient density the blast wave may already be radiative while the evolution of other parts is still adiabatic (e.g. Vink 2012). In the literature, SNRs with an evolutionary stage at the end of phase 2 or early in phase 3 are denoted as "mature" SNRs.

Phase 4, the merging phase, is reached when the post shock velocities and temperatures become comparable to the respective values of the CSM. By this time, these "old" SNRs are very extended strucures that begin to merge with the ambient material, and finally all the explosion ejecta are mixed back into the interstellar medium.

1.6 Organisation and objectives of this work

As described in the previous sections, many questions regarding SN explosions, their progenitors, and their evolution in the remnant phase still remain open. In this thesis, the main emphasis is on observables in the high-energy regime from

keV to MeV energies that are very indicative with respect to distinct features of suggested SN models. Being directly connected to characteristic nuclear reactions, these observables allow for unambiguous conclusions on certain properties of SNe that are not so easily accessible by observables in other wavelength ranges. In order to study the diagnostic value of these high-energy observables with respect to future observation campaigns, the predictions of different models for certain phases of the SN evolution are compared and detector simulations are performed. The scientific issues that are addressed in this work in connection with SN explosions are shortly summarised in the following.

One of the long-standing questions in astrophysics is the question of the origin of cosmic rays. Although SNRs were already proposed as sources of Galactic cosmic rays in the 1930s (Zwicky 1938), clear evidence for theories of cosmic ray acceleration at SNR shocks is still lacking. Only observations of few SNRs show obvious indications of cosmic ray acceleration processes (e.g. Ackermann et al. 2013), and the overall contribution of SNRs to the total amount of Galactic cosmic rays as well as the detailed properties of the acceleration processes themselves (efficiency, importance of non-linearities, etc.) remain a matter of discussion. In Chapter 2, nuclear de-excitation lines resulting from the interactions of accelerated cosmic ray particles with the ambient material are introduced as a complementary tool for the identification of cosmic ray acceleration sites. The signatures at MeV energies are studied for the case of the Galactic SNR Cassiopeia A, and their detection prospects with respect to future telescope missions in the MeV energy range are discussed.

In contrast to core-collapse SNe, progenitor systems of SNe Ia have not directly been observed so far. Although SNe Ia serve as important tools for observational cosmology (e.g. Riess et al. 1998; Perlmutter et al. 1999) and influence the chemical evolution of galaxies in a major way (Kobayashi & Nomoto 2009), the progenitor question is still debated and several scenarios for the explanation of SNe Ia explosions are proposed (see Subsection 1.3.2). The identification of these scenarios by comparing sophisticated three-dimensional simulations to observations is further complicated by the fact that even conceptually very different models exhibit degeneracies regarding their predicted observables and cannot easily be differentiated (e.g. Röpke et al. 2012). In Chapter 3, two explosion models representing the single- and the double-degenerate progenitor channel are studied with respect to their early-time gamma-ray emission in the MeV energy range. The possibilities of lifting the degeneracies existent in other wavelength regimes by complementary measurements at MeV energies are investigated and different diagnostic tools and observation strategies for future telescope missions are presented.

In addition to the radioactive isotope ^{56}Ni that is the origin of the gamma-ray emission at early times due to its rather short half-life of a few days, also other unstable nuclei with longer half-lives can produce characteristic signatures that emerge in later phases of the SN evolution. If the abundances of these nuclei are sensitive to the prevailing conditions during explosive nucleosynthesis and if the nucleosynthetic conditions differ between certain explosion scenarios, the emission connected to the

decay processes can be used as a viable diagnostic tool. This is elaborated in more detail for the example of the radioactive isotope ^{55}Fe in Chapter 4. The X-ray line emission at 5.9 keV originating from the decay of ^{55}Fe and peaking at several years after explosion is calculated for the two representative SN Ia models introduced in the previous chapter. The detection prospects as well as the potential of this line for drawing conclusions on the underlying explosion model are studied for different current and future X-ray telescopes.

The calculation of observables for different models of SNe Ia relies on the treatment of nuclear reactions during the time of explosive nucleosynthesis. As it is computationally too expensive to run large nuclear reaction networks during the hydrodynamical simulations, the energy release from nuclear reactions is usually determined in an approximate manner and the detailed nucleosynthetic abundances are calculated in a post-processing step (see Subsection 5.2.2). A major source of uncertainties in the calculation of nuclear reactions are reaction rates that are not known with the required accuracy for the temperature and density conditions in SN explosions. In order to study the effect of recent updates of the applied reaction rate libraries with new results from experiment and theory, comparisons with calculations based on previous versions of the reaction rate libraries are drawn in Chapter 5. Furthermore, the possibility to perform in-situ reaction network calculations is implemented into the hydrodynamical code. In order to allow for simulations that are computationally not too expensive, two medium-sized reaction networks are constructed. These networks contain enough isotopes to enable reasonable radiative transfer calculations and also permit comparisons with the post-processing method and optimisations in future simulations. Due to the new availability of a nuclear reaction network in the hydrodynamical code that can easily be adjusted to the respective needs, further refinements concerning the treatment of nuclear flames, for example, come into reach.

2 Nuclear lines as a fingerprint of hadronic cosmic rays

This chapter focuses on the remnant phase of SN explosions and the acceleration processes of cosmic rays (CRs) that are supposed to take place when the SN ejecta are driven into the ambient medium and shock fronts build up. After a general discussion of the high-energy emission that is produced by the resulting interaction processes, nuclear de-excitation lines in the MeV energy range are especially studied as potential signatures of accelerated CR particles. In order to determine the diagnostic value and the detection prospects of these lines, the spectrum of nuclear de-excitation lines is calculated for the Galactic SNR Cassiopeia A. The results presented in the following are based on Summa et al. (2011).

2.1 Overview

Since the discovery of CRs by Victor Hess more than hundred years ago (Hess 1912), these energetic particles and their possible cosmic origins have been subject to intensive studies. The main constituents of CRs arriving at Earth are protons that are accompanied by smaller numbers of electrons and heavier nuclei. By now, particles with energies of more than 10^{20} eV have been detected. CRs seem to play an important role in the generation of magnetic fields and they contribute about one third to the total energy density in the interstellar medium. They are also thought to make up a major fraction of the energy content of explosive environments from stellar to galactic scales (cf. Bell 2013). This underlines the importance of understanding the detailed acceleration, transport, interaction, and emission processes that are related to these energetic particles. For a long time, SNRs have been prime candidates for the acceleration of CRs of Galactic origin with energies up to 10^{15} eV (Baade & Zwicky 1934a; Ginzburg & Syrovatskii 1969), but this proposition is still a matter of intensive discussion and many questions concerning the detailed acceleration mechanisms are still unresolved. Although potential sources of CRs can in principle be observed through their gamma-ray emission at GeV and TeV energies, the ambiguity of leptonic and hadronic acceleration scenarios in this wavelength regime makes it very difficult to identify a certain source as acceleration site of CRs. In this chapter, it is shown that nuclear de-excitation lines at MeV energies provide an additional possibility of testing theories of CR acceleration.

2.2 High-energy emission of supernova remnants

There are four main radiative processes that are thought to contribute to the photon emission of SNRs from keV to TeV energies: synchrotron radiation, non-thermal bremsstrahlung, inverse-Compton scattering, and neutral pion decays. An example of a model that includes the four different contributions in order to explain the spectral energy distribution of the SNR G347.3-0.5 is depicted in Fig. 2.1. While the first three processes result from interactions of electrons (leptonic processes), neutral pions are produced by inelastic scattering of CR ions from thermal protons and therefore have a hadronic origin. The following description of these four radiation processes is based on the review of Reynolds (2008), further details can be found in Sturner et al. (1997); Gaisser et al. (1998); Baring et al. (1999); Houck & Allen (2006). Due to a lack of sufficient sensitivities in the MeV energy range, the photon emission caused by the production of nuclear de-excitations is often discussed only marginally. In Sections 2.5 and 2.6 it is pointed out that especially these emission processes are well-suited for drawing conclusions on CR acceleration scenarios.

2.2.1 Synchrotron radiation

In SNRs, synchrotron processes can generate photons with energies up to a few tens of keV. At these energies, the small overlap with other radiation processes allows for a clear identification of this contribution to the spectral energy distribution of SNRs. An electron of energy E produces a continuous spectrum with a maximum at (Reynolds 2008)

$$h\nu_m = 1.93 \left(\frac{E}{100\,\mathrm{TeV}}\right)^2 \left(\frac{B}{10\,\mu\mathrm{G}}\right)\ \mathrm{keV}. \tag{2.1}$$

Before the maximum emissivity is reached, it rises proportionally to $\nu^{1/3}$, afterwards it drops exponentially. For a power-law electron spectrum of the form $N(E) = KE^{-s}$ (K is a constant), the synchrotron emissivity in photons $\mathrm{erg}^{-1}\,\mathrm{cm}^{-3}\,\mathrm{s}^{-1}$ is given by

$$\frac{\mathrm{d}n_\gamma}{\mathrm{d}E_\gamma\,\mathrm{d}t\,\mathrm{d}V} = \frac{4\pi}{h} c_5(s) \left(8.31 \times 10^{-8}\right)^{\frac{s-1}{2}} K B_\perp^{\frac{s+1}{2}} E_\gamma^{-\frac{1+s}{2}}, \tag{2.2}$$

where $B_\perp$ is the projected magnetic field on the plane of the sky (Reynolds 2008). Tabulated values for $c_5(s)$ can be found in Pacholczyk (1970). Since the synchrotron emissivity is roughly proportional to the product of electron and magnetic energy densities, measurements of the synchrotron emission alone cannot determine these two quantities independently. This is why it is rather difficult to get exact values for these quantities that are very important in the context of CR acceleration theories. Synchrotron radiation at X-ray wavelengths can only be produced by very energetic electrons, so the radiation in the X-ray band provides inferences regarding the high-energy end of the electron spectrum. All known SNRs exhibit X-ray fluxes that

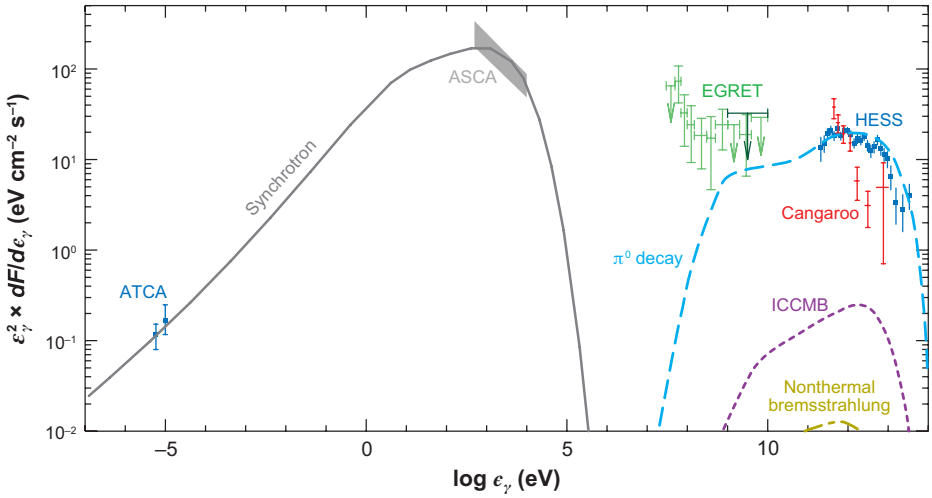

Figure 2.1: Model of the spectral energy distribution of the SNR G347.3-0.5. While data points in light green mark EGRET observations of a nearby source, the dark green point denotes the EGRET upper limit at the location of G347.3-0.5. "ICCMB" labels the contribution from inverse-Compton processes with photons of the cosmic microwave background (taken from Reynolds 2008).

are lower than a simple extrapolation of the electron spectrum required for the explanation of the emission at radio energies would predict. At TeV energies, the electron spectrum steepens since electron acceleration processes reach their limits and high-energy electrons are additionally depleted by effective radiative losses (cf. Reynolds 2008).

2.2.2 Inverse-Compton scattering

In inverse-Compton processes, photons are upscattered in frequency by relativistic electrons. For electrons with Lorentz factor γ, the energy change of the photons is proportional to γ^2 (Reynolds 2008). If the initial energy of photons $E_{\gamma i}$ is significantly smaller than the rest energy of the electron in its rest frame and the condition $4\gamma E_{\gamma i}/m_e c^2 \ll 1$ is fulfilled, the scattering process can be described by the Thomson cross section $\sigma_T = 8\pi r_e^2/3$ where r_e is the classical electron radius. In all other cases, the Klein-Nishina cross section has to be used. For an electron of energy $E = \gamma m_e c^2$ that interacts with an isotropic photon field $\mathrm{d}n_\gamma(E_{\gamma i})/\mathrm{d}V$, the spectrum of outgoing photons in the quantum-mechanical correct form is given by (see e.g. Blumenthal & Gould 1970)

$$\frac{\mathrm{d}n_{\gamma,e}}{\mathrm{d}E_\gamma\,\mathrm{d}t} = \frac{3}{4}\frac{\sigma_T c}{\gamma^2}\frac{m_e c^2}{E_{\gamma i}}\frac{\mathrm{d}n_\gamma(E_{\gamma i})}{\mathrm{d}V}\mathrm{d}E_{\gamma i}\left[2q\ln q + (1+2q)(1-q) + \frac{\Gamma_e^2 q^2 (1-q)}{2(1+\Gamma_e q)}\right] \quad (2.3)$$

with

$$q \equiv \frac{E_\gamma}{4E_{\gamma i}\gamma\left(\gamma - \frac{E_\gamma}{m_e c^2}\right)} \quad \text{and} \quad \Gamma_e \equiv \frac{4\gamma E_{\gamma i}}{m_e c^2}. \tag{2.4}$$

The total photon spectrum can be calculated by integrating over the electron spectrum $N(\gamma) = N(E)\mathrm{d}E/\mathrm{d}\gamma = N(E)m_e c^2$:

$$\frac{\mathrm{d}n_\gamma}{\mathrm{d}E_\gamma\,\mathrm{d}t\,\mathrm{d}V} = \int N(\gamma)\mathrm{d}\gamma \int \frac{\mathrm{d}n_{\gamma,e}}{\mathrm{d}E_\gamma \mathrm{d}t}. \tag{2.5}$$

In the Thomson limit, the total photon spectrum has a shape similar to the initial electron spectrum. If the average energy of incident photons is $\langle E_{\gamma i}\rangle$ and the electron spectrum cuts off at an energy $E_{\max}$, the relation $\nu_{\max} \sim \gamma^2 \langle E_{\gamma i}\rangle$ for the corresponding cut-off frequency of the photon spectrum holds. Below the cut off, the slope of the photon spectrum is the same as for the synchrotron spectrum (see Subsection 2.2.1). Since the local radiation density in the neighbourhood of SNRs is typically an order of magnitude less than that of the cosmic microwave background, the latter is usually the dominant photon field taking part in inverse-Compton processes (cf. Gaisser et al. 1998).

2.2.3 Bremsstrahlung

When electrons interact with the ambient gas, they emit bremsstrahlung. In addition to the thermal continuum provided by low-energy electrons, non-thermal electrons with energies above a few tens of keV produce a power-law photon spectrum with the same index as the initial electron spectrum. Since an electron with energy E emits bremsstrahlung photons up to energies of approximately $E/3$, the synchrotron emission at keV energies and the bremsstrahlung emission at TeV energies are caused by the same population of TeV electrons. While the first contribution is determined by the prevailing magnetic fields, the second is influenced by the ion densities in the ambient medium. The ratio of electron-electron to electron-ion contributions is ~ 0.86 for electron energies above $\sim 10\,\mathrm{MeV}$. The emission of non-relativistic electrons interacting with thermal electrons can usually be neglected (Baring et al. 1999). The bremsstrahlung emission of an electron in an ambient medium consisting mainly of H and He is given by (v_e is the electron velocity, n_H, n_{He}, and n_e are the number densities of H and He in the ambient medium as well as the electron density, Reynolds 2008)

$$\frac{\mathrm{d}n_{\gamma,e}}{\mathrm{d}E_\gamma\,\mathrm{d}t} = v_e\left[(n_{\mathrm{H}} + 4n_{\mathrm{He}})\,\sigma_{e-p}(E, E_\gamma) + n_e\sigma_{e-e}(E, E_\gamma)\right]. \tag{2.6}$$

The Bethe-Heitler cross section σ_{e-p} is proportional to Z^2, this charge dependence leads to the factor $n_{\mathrm{H}} + 4n_{\mathrm{He}}$ in front of σ_{e-p} (Bethe & Heitler 1934). Analytic expressions for σ_{e-e} can be found in Baring et al. (1999).

2.2.4 Neutral pion decays

For proton interactions of the form $p + p \rightarrow \mathrm{X}$ above the total energy threshold of $\sim 1.2\,\mathrm{GeV}$ for the creation of pions, the cross section only varies slightly with energy and is roughly comparable to the geometrical cross section of a proton, $\sigma \sim 10^{-26}\,\mathrm{cm}^{-2}$ (see Dermer 1986). In these interaction processes, mostly pions equally distributed between π^0, π^+, and π^- are produced and isotropically emitted in the target rest frame. In order to produce a neutral pion with energy E_{π^0}, a proton energy of

$$E_{\min}(p) = m_p c^2 + 2E_{\pi^0} + m_{\pi^0} c^2 \left(2 + \frac{m_{\pi^0}}{2m_p}\right) \tag{2.7}$$

is required (Reynolds 2008). For an incident flux $J_p(E)$ of energetic protons that interact with a thermal H gas of number density n_{H}, the spectrum of the produced π^0 is given by (Reynolds 2008)

$$Q_{\pi^0}(E_{\pi^0}) = 4\pi n_{\mathrm{H}} \int\limits_{E_{\min}(p)}^{\infty} \mathrm{d}E_p J_p(E) \frac{\mathrm{d}\sigma(E_p, E_{\pi^0})}{\mathrm{d}E_{\pi^0}}. \tag{2.8}$$

All details of strong-interaction physics are incorporated in the differential cross section $\mathrm{d}\sigma(E_p, E_{\pi^0})/\mathrm{d}E_{\pi^0}$. The minimum pion energy that is needed for the production of a photon of energy E_γ amounts to (Reynolds 2008)

$$E_{\min}(\pi^0) = E_\gamma + \frac{m_{\pi^0}^2 c^4}{4E_\gamma}. \tag{2.9}$$

The photon spectrum resulting from neutral pion decays ($\pi^0 \rightarrow \gamma + \gamma$) can be calculated to be (p_{π^0} is the pion momentum, cf. Reynolds 2008)

$$\frac{\mathrm{d}n_\gamma}{\mathrm{d}E_\gamma\,\mathrm{d}t\,\mathrm{d}V} = 2f \int\limits_{E_{\min}(\pi^0)}^{\infty} \mathrm{d}E_{\pi^0} \frac{Q_{\pi^0}(E_{\pi^0})}{p_{\pi^0}}. \tag{2.10}$$

The factor f is introduced to account for heavier isotopes than H in the populations of accelerated and target particles. Thereby, it is assumed that the energy dependence of the pion production by heavier particles is similar to the case when protons interact with protons. For an isotropic distribution of neutral pions, the photon spectrum is symmetric and peaks at an energy of $m_{\pi^0}/2 \approx 68\,\mathrm{MeV}$.

2.3 Supernova remnants as sites of cosmic ray acceleration

To a first approximation, the differential energy spectrum of CRs can be described by a power law with an overall spectral index of -2.8. However, a closer look reveals

a characteristic "knee-ankle" structure of the spectrum (see Fig. 2.2). After a power-law slope of -2.7 from GeV energies up to a few PeV, the spectrum steepens to a spectral index of -3.1. This feature is often referred to as the "knee" of the CR spectrum. At roughly 1 EeV, the spectrum flattens again until it turns over and terminates at a few 100 EeV, comparable to an "ankle" at a few EeV (see Nagano & Watson 2000). Since the Lamor radius of a proton with energies above the "ankle" is much larger than our Galaxy, CRs of these energies are thought to have an extragalactic origin, while CRs with energies below the "knee" with respective smaller Lamor radii must originate within the Galaxy. The exact location of the transition point from CRs of Galactic to CRs of extragalactic origins is still a matter of debate, but there are indications that the composition of CRs changes around the "knee" (e.g. Hörandel 2008). Due to the smaller Lamor radii of heavier nuclei with higher charges compared to protons of the same energy, these heavier nuclei diffuse less easily away from the sites of CR acceleration and can be accelerated to higher energies even in our Galaxy. But also additional populations of protons that are accelerated beyond the "knee" within the Galaxy may be needed to explain the CR spectrum (Hillas 2005, 2006). Except for the particles of highest energies, most CRs are deflected by interstellar or intergalactic magnetic fields and deliver no directional information about their source. This is why the identification of sources of CRs mainly relies on observations of electromagnetic radiation that is produced by the accelerated particles near the acceleration sites (see below and also Section 2.2).

The arguments in favour of SNRs as dominant sources of Galactic CRs exhibiting a constant slope of -2.7 over many decades up to the "knee" can be summarised as follows. With a Galactic CR density of 1–2 $\mathrm{eV\,cm^{-3}}$ (Webber 1998) and a time of ~ 15 Myr that CRs of GeV energies need on average to diffuse out of the Galaxy (Yanasak et al. 2001), the required total power of the Galactic CR production results in $10^{41}\,\mathrm{erg\,s^{-1}}$ (cf. Ginzburg & Syrovatskij 1967). The only candidates known for being able to provide such amounts of energy are SN explosions. They have an average kinetic explosion energy[1] of $\sim 10^{51}$ erg, a frequency of 2–3 per century in our Galaxy (Tammann et al. 1994), and their total power amounts to $\sim 10^{42}\,\mathrm{erg\,s^{-1}}$. To account for the CRs of Galactic origin, SNe must therefore transfer $\sim 10\,\%$ of the explosion energy into the acceleration processes of particles. Nevertheless, it has to be noted that because of the steepness of the spectrum the largest contribution to the CR energy density comes from CRs with low energies. Since low energy CRs are shielded from the solar system by the solar wind, this part of the spectrum is least known and this uncertainty of course enters the determination of the total CR energy density.

Although it is commonly believed that SNRs are the most promising sites for the acceleration of Galactic CRs, the detailed acceleration mechanisms and the time during the evolution of SNRs when CR acceleration takes place most efficiently are still a matter of discussion. Besides the general view that CR acceleration processes mainly occur in the earlier phases of SNR evolution (e.g. Vink 2012),

[1] The energy contribution of neutrinos is not considered here.

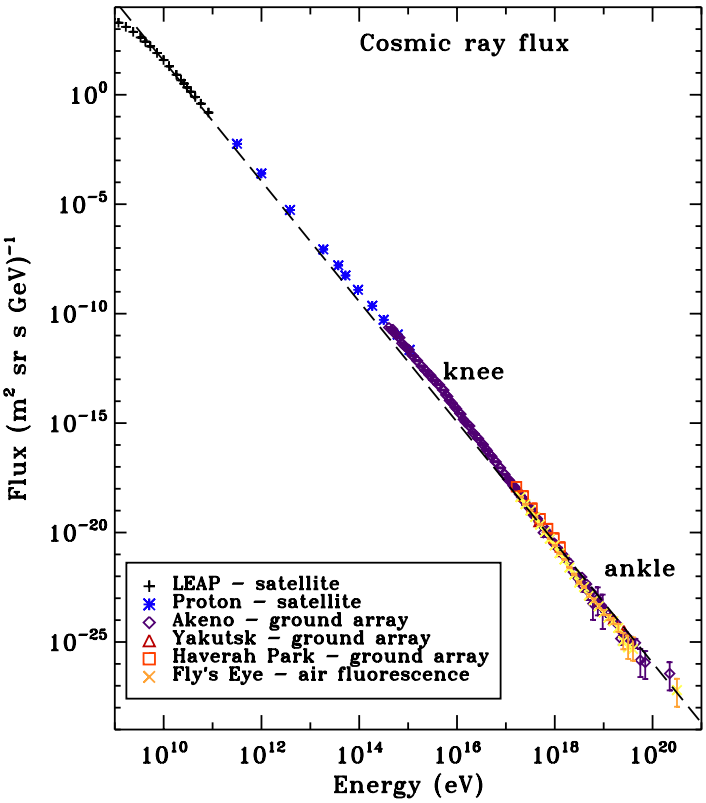

Figure 2.2: Particle fluxes of CRs as observed by different instruments in dependence on the particle energy (taken from Helder et al. 2012). The dashed line represents a slope of −2.8.

other theories suggest collective effects as main contributors for the acceleration of Galactic CRs. Multiple SNR and stellar wind shocks in active star-forming regions could in principle provide mechanisms for the generation of particles with energies up to $\sim 1\,\mathrm{EeV}$ (see e.g. Bykov & Fleishman 1992; Parizot et al. 2004).

Especially the detection of non-thermal emission from SNRs points towards the existence of particle acceleration processes (for current reviews of this field see Reynolds 2008; Hinton & Hofmann 2009; Helder et al. 2012), although non-thermal radio and X-ray synchrotron emission in first place only give direct evidence for the acceleration of electrons. The likewise detected gamma-ray emission of SNRs could be produced by inverse-Compton processes of energetic electrons (leptonic emission scenario) or the decay of pions that are produced by the interaction processes of accelerated protons (hadronic emission scenario). For many sources (see also Section 2.4), it is difficult to give preference to one of these scenarios for the explanation of the observed gamma-ray emission, but recent observations indicate a dominant contribution of pion processes at least for the high-energy emission of a number of sources (e.g. Giordano et al. 2012; Ackermann et al. 2013). Also a study

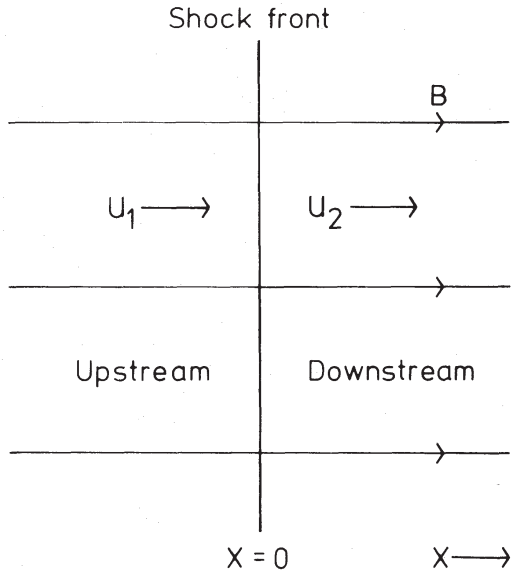

Figure 2.3: Schematic representation of a parallel shock viewed in the shock rest frame (taken from Bell 1978a). The variables defined in the text are also indicated.

of visible light emitted by H atoms in the shock region of the remnant of SN 1006 suggests the existence of protons with very high velocities (Nikolić et al. 2013).

In 1949, Fermi suggested a mechanism for the acceleration of charged particles colliding with clouds in the interstellar medium (Fermi 1949). Scattering processes with the turbulent magnetic field structures within the clouds isotropise the CRs and, due to the fact that head-on collisions are on average more frequent, a net acceleration occurs. This so-called second order Fermi process where the energy increase $\Delta E/E$ is proportional to $(v_c/c)^2$ (v_c is the velocity of the moving cloud) could be important for CR acceleration in older SNRs (see e.g. Ostrowski 1999), but it is generally thought that the acceleration of particles is a result of a faster first order Fermi process that operates in the vicinity of shocks (Krymskii 1977; Axford et al. 1977; Bell 1978a,b; Blandford & Ostriker 1978). According to this mechanism that is often denoted as "diffusive shock acceleration", charged particles scatter off magnetic field fluctuations on both sides of the shock and repeatedly traverse the shock front. The faster the shock velocity is, the larger the net energy gain for each crossing of the shock, and the relation $\Delta E/E \propto v_s/c$ (v_s is the shock velocity) holds. The resulting CR spectrum can be calculated either by solving the Boltzmann equation for a CR distribution near a shock (macroscopic approach) or by applying the statistics of a random walk to a single particle (microscopic approach, see Drury 1983).

According to the microscopic approach first introduced by Bell (1978a,b), the resulting distribution of shock accelerated particles can be derived as described in the following. The calculation is preceded by several assumptions. First, the ions

and electrons accelerated by the Fermi mechanism are "test particles" that do not have sufficient pressure to influence the hydrodynamics of the shocked plasma. The shock is assumed to be planar, the magnetic field lines are parallel to the shock normal. Second, the velocities of the test particles are thought to be significantly larger than the (non-relativistic) shock speed. Due to the small-angle scattering off magnetic field fluctuations, the particle distributions are assumed to be isotropic in both the upstream and the downstream plasma frames. In this so-called "diffusion approximation", the particles are also isotropic in the shock rest frame. In case of relativistic shocks, the diffusion approximation breaks down and strong anisotropy effects have to be accounted for (Kirk & Schneider 1987; Achterberg et al. 2001).

Here, the velocities of the up- and downstream flow in the shock rest frame are denoted by u_1 and u_2 (see Fig. 2.3). The flux of particles that are advected with the downstream flow is nu_2 (in the diffusion approximation, the number density n of particles with velocity v in the local fluid frame is constant downstream). For an isotropic distribution, the number of particles crossing the shock front per unit time from upstream to downstream is half the number of particles moving towards the shock. With an average projected velocity of half the shock velocity, the respective flux amounts to $nv/4$. Thus the probability of particles not returning to the shock is $nu_2/(nv/4) = 4u_2/v$ and the probability of crossing the shock again is accordingly

$$P_{\mathrm{cross}} = 1 - \frac{4u_2}{v}. \tag{2.11}$$

The average change in a particle's momentum with respect to the local fluid frame can be determined to (e.g. Schure et al. 2012)

$$\Delta p = \frac{2}{3v} p \left(u_1 - u_2\right). \tag{2.12}$$

For a complete cycle around the shock front, this result has to be multiplied with a factor of 2. The number of particles still present at the shock after k cycles is

$$N = N_0 \left(1 - \frac{4u_2}{v}\right)^k, \tag{2.13}$$

and the momentum gain amounts to

$$p = p_0 \left[1 + \frac{4}{3v}\left(u_1 - u_2\right)\right]^k \tag{2.14}$$

where N_0 and p_0 are the respective initial values. Eliminating k and using $v \gg u_1,\, u_2$ gives

$$\frac{\ln\left(\frac{N}{N_0}\right)}{\ln\left(\frac{p}{p_0}\right)} = \frac{k \ln\left(1 - \frac{4u_2}{v}\right)}{k \ln\left(1 + \frac{4}{3v}\left(u_1 - u_2\right)\right)} \approx \frac{-\frac{4u_2}{v}}{\frac{4}{3v}\left(u_1 - u_2\right)} = -\frac{3}{r-1} \tag{2.15}$$

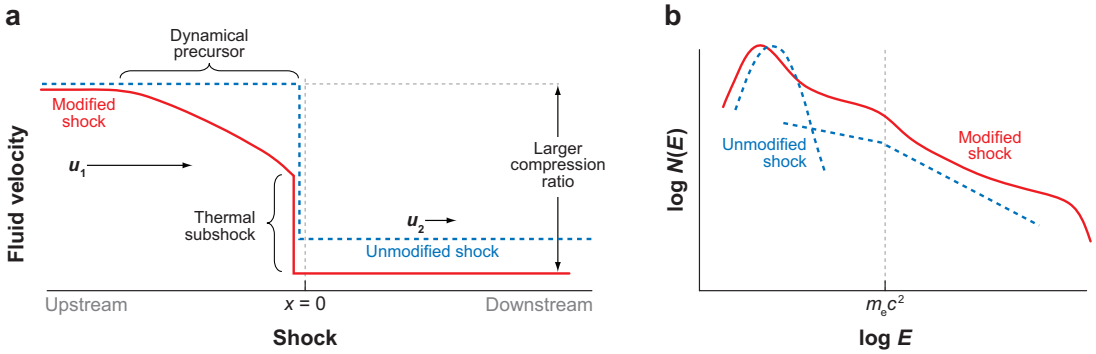

Figure 2.4: a) Schematic comparison of a modified (red lines) and an unmodified (dotted blue lines) shock. b) Corresponding particle energy distributions for both shock types. The different contributions of thermal and non-thermal particles as well as the transition from non-relativistic to relativistic energies can more easily be identified in case of the unmodified shock (taken from Reynolds 2008).

with the compression ratio $r = u_1/u_2$. The number of particles as a function of momentum can be derived to

$$\frac{N}{N_0} = \left(\frac{p}{p_0}\right)^{-\frac{3}{r-1}}, \tag{2.16}$$

which results in a differential energy spectrum of

$$N(\mathrm{E})\mathrm{d}E \propto E^{-\frac{r+2}{r-1}}\mathrm{d}E \tag{2.17}$$

for relativistic energies. For typical high-Mach number shocks with a compression ratio of $r = 4$, the spectrum declines with a power-law index of -2. The corresponding power-law index for non-relativistic CRs is -1. More details on diffusive shock acceleration processes are summarised in Drury (1983); Blandford & Eichler (1987); Jones & Ellison (1991); Malkov & O'C Drury (2001); Schure et al. (2012); Bell (2013) and can also be found in the original publications cited above.

The derivation shows that the natural solution for the energy spectrum of non-thermal CR ions and electrons is a power-law distribution. The small number of key assumptions that go into the simplest version of the shock acceleration theory introduced above underlines the universality of this mechanism and its broad applicability in diverse astrophysical environments where strong shocks exist. Although the predicted CR spectrum is slightly flatter than the measured spectrum of $N(E) \propto E^{-2.7}$ for Galactic CRs, the deviation might be explained by propagation effects of CRs through the Galaxy and the agreement between observations and the theory introduced above is remarkably close.

One of the open questions regarding the Fermi acceleration process concerns the injection of particles that reach sufficient velocities to get back to the unshocked

medium. While it is often assumed that these particles originate from the high-velocity tail of the Maxwellian velocity distribution, computer simulations also indicate the existence of non-thermal distributions of particles directly behind the shock that may fulfill this requirement (cf. Bykov & Uvarov 1999; Riquelme & Spitkovsky 2008).

The process of diffusive shock acceleration gets more complicated when the pressure of the accelerated particles cannot be neglected any more and non-linear effects become important (cf. Caprioli et al. 2008; Vink 2012). Since particles scattered upstream of the shock decelerate the inflowing material and generate a so-called precursor region (see Fig. 2.4), the compression ratio at the main shock can be reduced, even though the overall compression ratio can increase beyond 4. So, depending on their energy, the diffusing particles experience different compression ratios. While high-energy particles with gyro radii larger than the size of the precursor region are exposed to the total compression ratio, particles with lower energies only sample smaller values of this ratio. This results in an energy spectrum with a steeper spectral index at lower energies. For higher energies the spectrum is flatter than that of the test particle calculation and approaches a limiting index of -1.5 (Malkov 1997). Although there is observational evidence of steeper particle spectra at lower energies (see Vink 2012), other processes have been introduced that may possibly counteract a flattening at higher energies (e.g. Morlino et al. 2007; Zirakashvili & Ptuskin 2008).

Since acceleration speed and maximum energy of particles participating in a Fermi process increase for higher magnetic fields and stronger magnetic turbulence, the interaction of streaming CRs with turbulent magnetic fields and the accompanying amplification effects are an active field of research. Due to resonant or non-resonant instabilities of the magnetic field, CR currents can lead to significant enhancements of the magnetic field strenghts, which in turn allow particle acceleration to higher maximum energies (cf. Lucek & Bell 2000; Caprioli et al. 2008). This is why the study of nonlinearities and amplification effects in case of acceleration mechanisms is fundamental to the understanding of the origin of CRs. For a more thorough discussion of these aspects the reader is referred to Drury (1983); Blandford & Eichler (1987); Jones & Ellison (1991); Malkov & O'C Drury (2001); Schure et al. (2012); Bell (2013). A comparison of theory to recent observational results can be found in Hillas (2005); Reynolds (2008); Hinton & Hofmann (2009); Helder et al. (2012).

2.4 The supernova remnant Cassiopeia A

Cassiopeia A (Cas A) is one of the youngest known Galactic SNRs. Since it is one of the best-studied SNRs in our Galaxy where many observational data are available, Cas A is chosen as example for the subsequent discussion. The remnant's expansion rate indicates an explosion date of around 1680 AD (Thorstensen et al. 2001; Fesen

et al. 2006) and it is probably linked to a SN observed by the English astronomer Flamsteed at that time (Ashworth 1980). Based on a combination of Doppler shifts and proper motions, the distance of Cas A can be estimated to $3.4^{+0.3}_{-0.1}$ kpc. For this value, the angular size of $2.5'$ corresponds to a physical size of 2.34 pc (Reed et al. 1995). By the use of optical spectra obtained from distant light echoes of the original blast it can be shown that Cas A was a Type IIb SN (cf. Section 1.2). The explosion of the $\sim 15\,M_\odot$ main-sequence star is thought to have originated from the collapse of a red supergiant star that lost most of its H envelope and mainly consisted of a bare He core at the time of explosion (Krause et al. 2008).

The characteristic two-shock structure that usually develops during the evolution of SNRs (see Subsection 1.5.2) can also be observed in case of Cas A (see Fig. 2.5). The emission at most wavelengths is dominated by a $30''$ thick "bright ring" where the ejecta are heated and ionised when they encounter Cas A's reverse shock. X-ray studies of this shell show a composition of undiluted ejecta rich in O, Si, S, and Fe (Willingale et al. 2002; Laming & Hwang 2003; Lazendic et al. 2006). Faint X-ray filaments outside of the shell mark the location of the forward shock where non-thermal X-ray synchrotron radiation is produced by shock-accelerated electrons (Gotthelf et al. 2001; Vink & Laming 2003). The forward shock driven by the initial blast wave expands at roughly $5000\,\mathrm{km\,s^{-1}}$, the reverse shock moves at roughly half the rate of the forward shock (Gotthelf et al. 2001; DeLaney & Rudnick 2003). Measurements by BeppoSAX (Vink et al. 2001), INTEGRAL (Renaud et al. 2006), and Suzaku (Maeda et al. 2009) show a hard X-ray continuum (photon index[2] of ~ 3) extending up to 100 keV. Due to the limited angular resolution of these instruments, a precise localisation of the origin of this radiation cannot be given.

Being the brightest radio source in our Galaxy, Cas A has been extensively observed in this wavelength regime after its first detection in 1948 (e.g. Ryle & Smith 1948; Bell et al. 1975; Tuffs 1986; Braun et al. 1987; Anderson et al. 1991; Kassim et al. 1995). According to these observations, the main part of the radio emission comes from a region that roughly coincides with the bright shell visible in X-rays. The radio spectrum can be described by a power-law $J(\nu) \sim \nu^{-\alpha}$ with a spectral index of $\alpha = 0.77$ (Baars et al. 1977). A faint outer radio plateau is found near the outer thin X-ray edges where the forward shock propagates in the circumstellar material. Besides the large-scale structures, several hundreds of compact and bright radio knots with steeper spectra can be identified in the radio shell (Anderson et al. 1991).

Due to the vast dilution by the expansion of the ejecta after the SN explosion, the prevailing magnetic fields in the ejecta should be rather weak. With significantly lower magnetic field strengths than those in the interstellar medium the forward

[2]For a power-law spectrum of an astrophysical source, the *spectral index* α is defined by $F_\nu \propto \nu^\alpha$ where F_ν is the flux per unit frequency. In X-ray and gamma-ray astronomy, often the number of photons per unit energy interval is considered. In this case, power-law spectra are defined by $N(E) \propto E^{-\Gamma}$ with the *photon index* Γ. Photon index and spectral index are related by $\Gamma = 1 - \alpha$.

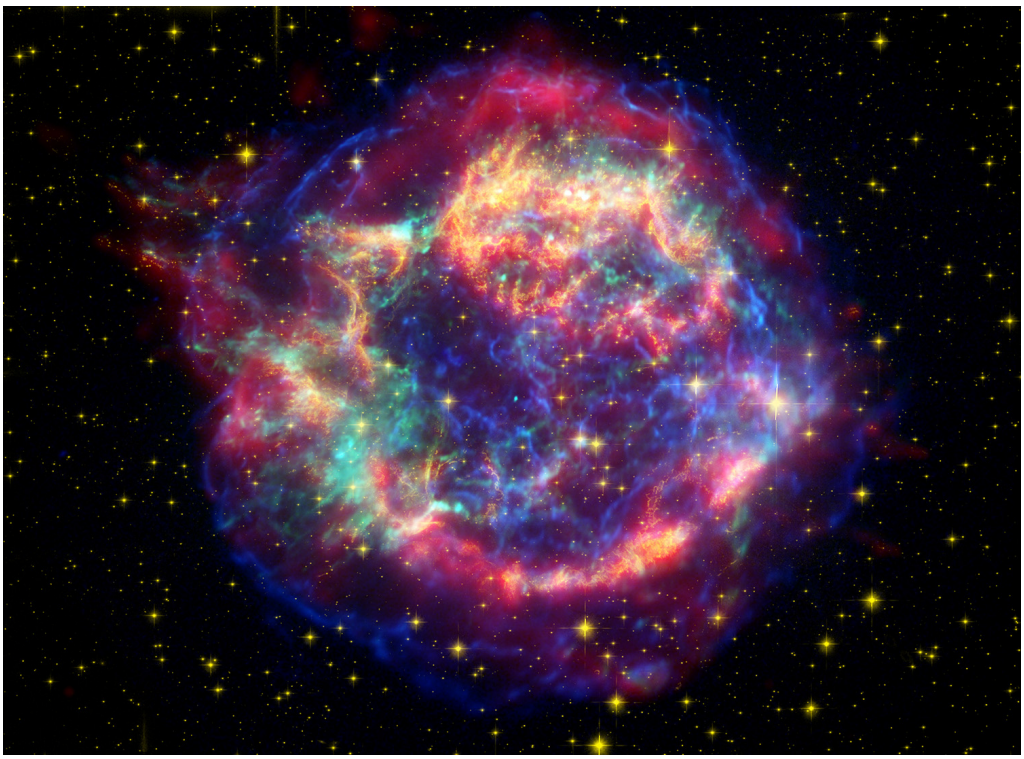

Figure 2.5: False-colour picture of the SNR Cas A. Infrared data from the Spitzer Space Telescope are coloured in red and visible data from the Hubble Space Telescope in yellow. X-ray data from the Chandra X-ray observatory are indicated in green and blue. While the Spitzer Space Telescope reveals warm dust of several 100 K in the outer shell, the Hubble Space Telescope sees filamentary structures of hot gases of about 10^4 K. The hot gases observed by Chandra have temperatures up to 10^6 K. The turquoise dot at the centre of the remnant is Cas A's neutron star as observed by Chandra (Credit: NASA/JPL-Caltech/O. Krause (Steward Observatory)).

shock interacts with, the reverse shock does not seem to be an efficient site of particle acceleration a priori. However, the existence of the inner shell in the X-ray and radio wavelength regime can be explained quite naturally by the fact that electrons are also accelerated at the reverse shock (Uchiyama & Aharonian 2008; Helder & Vink 2008). This contradiction is resolved when the amplification processes described in the last paragraph of Section 2.3 are taken into account. Although often applied to the forward shock region, these effects occur in an equal manner at the reverse shock site and should in principle allow for an efficient acceleration of CRs (Ellison et al. 2005). According to the observations cited above, Cas A is a unique object for studying particle acceleration at the reverse shock side.

Therefore, gamma-ray emission (see also Section 2.3) can also be expected for both the forward shock and reverse shock region, even though the resolution of current

gamma-ray telescopes does not permit a separation between these two acceleration sites. The initial observation of energetic gamma-ray emission from Cas A is reported by the HEGRA telescopes (Aharonian et al. 2001), making the SNR the first to be verified in TeV gamma rays. Observations by MAGIC and VERITAS confirm these results (Albert et al. 2007; Humensky 2008). They report energy spectra with a photon index of 2.4–2.6 and maximum photon energies of $\sim 5\,\mathrm{TeV}$. Recent observations with Fermi-LAT in the GeV range show a relatively flat energy distribution in the energy range of 0.5 GeV–50 GeV with a spectral index of roughly 2.0 (Abdo et al. 2010). Taking into consideration the gamma-ray data from GeV to TeV energies of Cas A, neither a leptonic nor a hadronic emission scenario can be ruled out. A combination of non-thermal bremsstrahlung and inverse-Compton emission on the one hand as well as neutral pion decays on the other hand could be responsible for the measured spectrum (Abdo et al. 2010, see also Fig. 2.6). Attempts to model the broadband spectral energy distributions of Cas A with leptonic and/or hadronic emission scenarios seem to favour at least an additional hadronic component for the explanation of the multi-wavelength data (Araya & Cui 2010; Zirakashvili et al. 2013), but the lack of data at sub-GeV and multi-TeV energies on the one hand and the rather large uncertainties in many model parameters on the other hand do not allow for drawing firm conclusions.

2.5 Nuclear de-excitation lines

As a consequence of the inelastic scattering of energetic particles on heavier nuclei as well as spallation reactions, the resulting product nuclei are often in an excited state. Besides the direct excitation of nuclear levels, also excited secondary nuclei can be produced. Furthermore, the production of radioactive species leads to decays into excited levels of other nuclei[3]. Many of these excited levels decay by the emission of gamma-ray photons in the energy range from 1 MeV to 20 MeV. The spectral structure of the gamma rays is determined by both the composition and the energy spectrum of the energetic particles and by the respective properties of the target nuclei in the ambient medium. The production of nuclear de-excitation lines is expected for many astrophysical sites, examples are solar flares, accreting black holes, gamma-ray bursts, and SN explosions. The detection of such lines gives a direct handle on many astrophysical processes that otherwise can only be studied indirectly, and it provides an unambiguous proof of the presence of CRs in the interstellar medium or in localised objects.

Especially CRs with energies less than 100 MeV are well-suited for being observed in gamma rays, because in that energy regime the gamma-ray fluxes due to nuclear de-excitations are the dominant energy loss mechanism. For CRs with higher energies, the gamma-ray fluxes owing to p–p and p–α collisions followed by π^0 desintegration

[3]The direct production of radioactive isotopes in SNe Ia and the resulting gamma-ray emission by de-excitation processes at early times after explosion are discussed in Chapter 3.

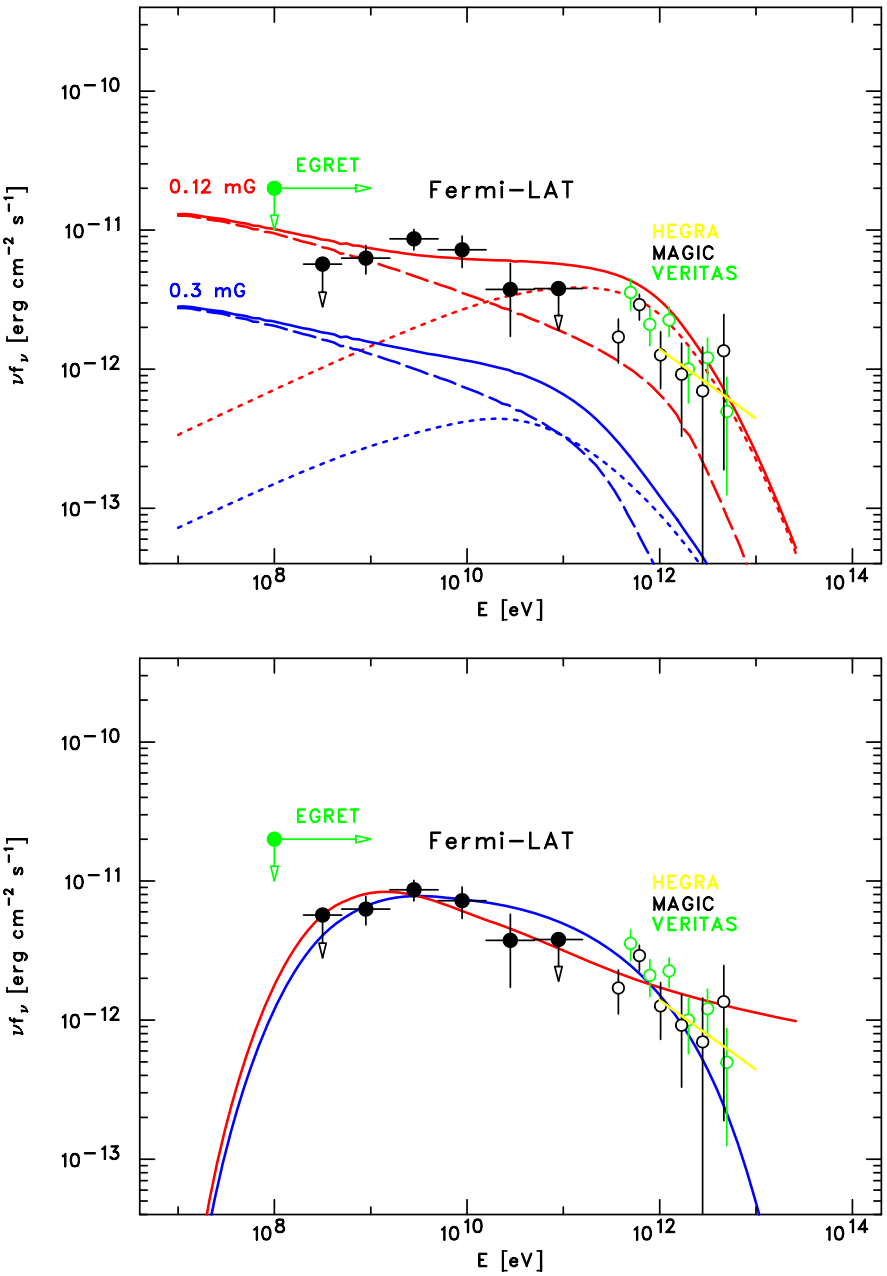

Figure 2.6: Leptonic and hadronic models of the high-energy emission of Cassiopeia A (taken from Abdo et al. 2010). *Upper panel:* Leptonic emission models assuming magnetic fields of $B = 0.12\,\mathrm{mG}$ (blue) and $B = 0.3\,\mathrm{mG}$ (red). The bremsstrahlung components (dashed lines) and the contributions due to inverse-Compton processes (dotted lines) are also indicated. *Lower panel:* Hadronic emission models for proton spectra with a power-law index of -2.1 and a cut-off energy of 10 TeV (blue) and a power-law index of -2.3 without a cut off (red).

are expected to be significantly higher (Meneguzzi & Reeves 1975). This is why the observation of gamma-ray lines below 100 MeV in principle offers the opportunity to reveal the origin of CRs and the validity of hadronic emission models for SNRs.

The basic ingredients for determining the profile of a gamma-ray line from energetic particle interactions can be summarised as follows. According to Ramaty et al. (1979), the probability of photon emission per second into solid angle $\mathrm{d}(\cos\theta_0)\,\mathrm{d}\phi_0$ can be written as (the z-axis is chosen in the direction of the incident particle)

$$\begin{aligned}\mathrm{d}P_\gamma = n_i v \frac{\mathrm{d}\sigma}{\mathrm{d}\Omega^*}(E,\theta_r^*)\,\mathrm{d}(\cos\theta_r^*)\,\mathrm{d}\phi_r \\ \times\, g(E,\theta_r^*,\theta_0,\phi_r-\phi_0)\,\mathrm{d}(\cos\theta_0)\,\mathrm{d}\phi_0.\end{aligned} \tag{2.18}$$

In the centre-of-mass frame, the interaction produces an excited nucleus with recoil velocity in $\mathrm{d}(\cos\theta_r^*)\,\mathrm{d}\phi_r$. The energy of the incident particle before the interaction is denoted by E, n_i is the number density of the target particles. The incident particle's velocity is ν, $\mathrm{d}\sigma/\mathrm{d}\Omega^*$ is the centre-of-mass differential cross section, and g is the angular distribution of the resulting gamma rays. The azimuth angles measured in the (x,y)-plane are ϕ_r and ϕ_0, θ_r^* and θ_0 are polar angles given with respect to the z-axis. To finally determine the gamma-ray spectrum, Equation 2.18 can be integrated over $\cos\theta_r^*$, ϕ_r, $\cos\theta_0$, and E by using the Monte Carlo simulation technique. By choosing random numbers (uniformly distributed between 0 and 1), the integrations can be carried out by solving for $\cos\theta_r^*$, ϕ_r, $\cos\theta_0$, and E from the equations

$$R_1 = \frac{1}{\sigma(E)} \int_{-1}^{\cos\theta_r^*} \frac{\mathrm{d}\sigma}{\mathrm{d}\Omega^*}\mathrm{d}\Omega^*, \tag{2.19}$$

$$R_2 = \frac{\phi_r}{2\pi}, \tag{2.20}$$

$$R_3 = C \int_0^E v N_p(E')\sigma(E')\mathrm{d}E', \tag{2.21}$$

$$R_4 = \frac{1}{2}(1+\cos\theta_0). \tag{2.22}$$

Here $N_p(E)$ is the number of incident particles per unit energy, C is a normalisation constant. The probability of observing gamma rays of energies between E_γ and $E_\gamma + \Delta E_\gamma$ is then proportional to the sum of all angular distributions g for which E_γ is in range. For a detailed description of the outlined methods above and a deeper insight into the different reaction types as well as the derivation of line production cross sections, the reader is referred to Ramaty et al. (1979) and Kozlovsky et al. (2002) and references therein.

2.6 Nuclear de-excitation line spectrum of Cassiopeia A

In order to get a first estimate of the expected line fluxes for the case of Cas A, the interaction of a proton with a ^{12}C target and the resulting gamma-ray line at 4.4 MeV are investigated. If the gamma-ray emission of Cas A is modelled by a fit based on hadronic interactions and subsequent π^0-decays, the best-fit proton acceleration spectrum can be determined to $Q_p(p) \propto p^{-2.3}$. The respective energy content of the accelerated protons corresponds to $\sim 2\,\%$ of the kinetic energy of the SNR and amounts to $W_p = \int_{10\,\mathrm{MeV}/c} Q_p p\,\mathrm{d}p = 4 \times 10^{49}\,\mathrm{erg}$ (cf. Abdo et al. 2010). For an extrapolation of the high-energy proton spectrum as denoted above down to the MeV energy range, the gamma-ray flux emitted in the 4.4 MeV de-excitation line of ^{12}C is approximately given by

$$F_\gamma = \frac{1}{4\pi d^2} n_\mathrm{C} \int Q_P(p)\sigma(p)v(p)\mathrm{d}p \tag{2.23}$$

where $n_\mathrm{C} \sim 10\,\mathrm{cm}^{-3}$ is the adopted mean density of carbon atoms in the interaction region (see Laming & Hwang 2003), v denotes the velocity of the accelerated protons and σ the cross section for the inelastic scattering processes. In this estimate, line broadening effects or additional contributions from unresolved gamma-ray lines in heavy nuclei and lines from long-term radioactive nuclei are not taken into account. With the distance of $d = 3.4\,\mathrm{kpc}$ to Cas A and the cross section for the reaction $^{12}\mathrm{C}(p,p')^{12}\mathrm{C}^*$ from Ramaty et al. (1979), the flux at 4.4 MeV can be calculated to be $F_\gamma \sim 10^{-6}\,\mathrm{cm}^{-2}\,\mathrm{s}^{-1}$. Such a line flux is slightly below the sensitivity limit of the last operating mission in that energy regime, the COMPTEL experiment, for which a line flux sensitivity of $\sim 10^{-5}\,\mathrm{cm}^{-2}\,\mathrm{s}^{-1}$ is reported (Iyudin et al. 1995). According to an analysis of the MeV continuum emission from Cas A, there only exists an upper limit of $1.4 \times 10^{-5}\,\mathrm{cm}^{-2}\,\mathrm{s}^{-1}$ in the energy range from 3 MeV to 10 MeV (Strong et al. 2000). This is why a future gamma-ray mission with enhanced sensitivity in the MeV range is needed to get definite results regarding the detection of de-excitation lines and thus the existence of CR acceleration processes in Cas A.

For the calculation of the whole gamma-ray line spectrum (see Fig. 2.7), the Monte-Carlo code initially developed by Ramaty et al. (1979)[4] (see also Section 2.5) is applied to the specific case of Cas A. Due to the fact that the Monte-Carlo code is one-dimensional, spherical symmetry and a homogeneous distribution of the SN ejecta are assumed. Therefore, the calculated spectrum of nuclear de-excitation lines represents averaged fluxes that do not take into account inhomogeneities or variations of the abundances in the ejecta. In order to obtain a well-resolved spectrum, the Monte-Carlo simulation is performed with 10^6 photons.

In addition to the ingredients already mentioned above, the calculation is based on the following assumptions. Since electron acceleration to multi-TeV energies is

[4] `http://lheawww.gsfc.nasa.gov/users/ramaty/code.htm`

Table 2.1: Mean measured abundance mass ratios and rms scatter respectively upper limits according to the results of Willingale et al. (2002), Docenko & Sunyaev (2010), and Chevalier & Kirshner (1979). The mass ratios are given relative to solar values. To faciliate the comparison, the data from Chevalier & Kirshner (1979) for H and He are indicated relative to Si, too.

ratio	mean	rms
H/Si	$< 2.29 \times 10^{-5}$	-
He/Si	$< 4.93 \times 10^{-3}$	-
C/Si	1.76	0.88
O/Si	1.69	1.37
Ne/Si	0.24	0.37
Mg/Si	0.16	0.15
S/Si	1.25	0.24
Ar/Si	1.38	0.48
Ca/Si	1.46	0.68
FeL/Si	0.19	0.65
FeK/Si	0.60	0.51
Ni/Si	1.67	5.52

likely to take place mainly at the reverse shock within the SN ejecta (e.g. Helder & Vink 2008), the acceleration of CRs is also assigned to this site in the Monte-Carlo simulations. Furthermore, the chemical composition of the accelerated CRs is taken from Engelmann et al. (1990). For the spectrum of the accelerated particles, a power law with index -2.3 is considered (see above) and the accelerated particles are assumed to be isotropic in the interaction region. The composition of the ambient gas is in fact a mixture of both massive Wolf-Rayet winds and SN ejecta (cf. Lingenfelter & Higdon 2007). For the detailed abundances, the results from X-ray spectroscopy given in Table 2.1 are used. The data for H and He are inferred from optical measurements by Chevalier & Kirshner (1979). The resulting mass is in line with the Wolf-Rayet-SN scenario, i.e. there is no room for additional amounts of H that would enhance the pion versus the nuclear de-excitation yields. The abundances defined in the input file of the Monte-Carlo code are normalised to H in case of the ambient gas. The accelerated particles are normalised to the proton abundance and all species have the given abundance at the same energy per nucleon.

Besides the consideration of the target particle recoils, unresolved gamma rays from heavy nuclei and lines from long-term radioactive nuclei are also included in the Monte-Carlo simulations. Therefore, a significant broadening of the lines can be seen in the resulting spectrum depicted in Fig. 2.7. Due to the elemental enrichment of the ambient medium in the progenitor star's Wolf-Rayet phase, the line fluxes are additionally enhanced. The detailed line characteristics of course rely on the precise

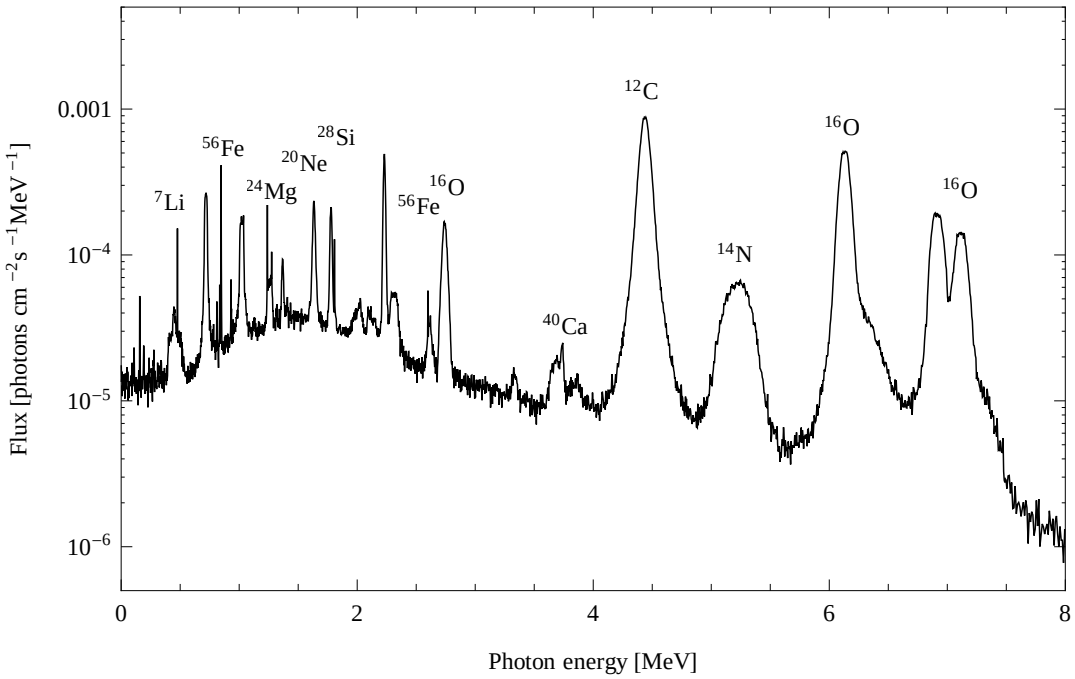

Figure 2.7: Calculated nuclear de-excitation line spectrum of Cas A by using the assumptions described in the text. 10^6 photons are binned into energy intervals of widths ranging from 2 keV to 5 keV as described in Ramaty et al. (1979). For example, the flux of the ^{12}C line at 4.4 MeV is at the edge of the sensitivity of COMPTEL (cf. Iyudin et al. 1995). Note that the continuum component caused by non-thermal electron bremsstrahlung is not taken into consideration here (taken from Summa et al. 2011).

knowledge about the composition of the SN ejecta, but the peculiar properties of the gamma-ray spectrum are defined on the one hand by the natural process of element synthesis in the progenitor star and on the other hand by the nucleosynthesis processes taking place during the SN explosion. In case of Cas A (cf. Fig. 2.7), the flux of the C and O lines in the 4–6 MeV band dominates the fluxes of the lines in the Ne-Fe group (1–3 MeV).

Regarding the calculation of the nuclear de-excitation line spectrum of Cas A introduced above, the extrapolation of the proton spectrum obtained from high-energy measurements down to the MeV range has to be discussed further. Although it is commonly believed that the spectra of non-thermal particles are quenched below GeV energies by strong Coulomb losses, the observations of solar flares with steep spectra indicate that there are mechanisms where these losses are not as important as previously thought. Relating to this argument, also the results of simulations concerning the acceleration processes of CRs in evolving SNRs should be taken into account. According to sophisticated non-linear models of CR acceleration developed by Berezhko & Völk (1997, 2000), the shape of the proton momentum spectrum at

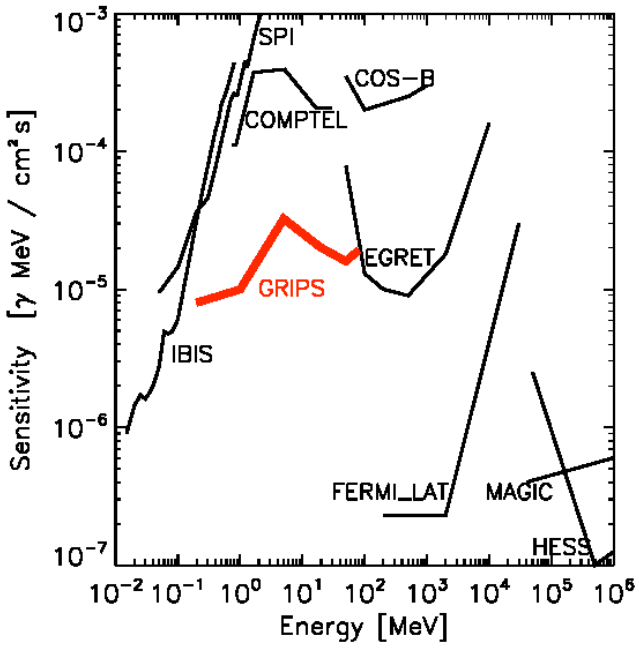

Figure 2.8: Sensitivities of different former and current detection instruments in the high-energy regime (black lines), revealing a gap in the MeV range. The estimated sensitivity of the proposed GRIPS mission is shown in red. The curves are for an exposure of 10^6 s, $\Delta E = E$, and an E^{-2} spectrum (taken from Greiner et al. 2012).

the shock front depends on the magnitude of the injection rate. While the overall proton spectrum is close to a pure power law in the entire momentum range down to MeV at low injection rates, it tends to be only slightly steeper in the low-energy part ($p \ll mc$) than in the high-energy part for high injection rates. These results are further supported by a study of Berezhko et al. (2003). Applying the non-linear kinetic model approach to the specific case of Cas A and using the data of recent observations, the authors were able to confirm the described shape of the proton acceleration spectra. This is why the assumption that an in-situ CR spectrum at MeV energies is as steep as at higher energies seems to be quite reasonable and theoretically motivated. Furthermore, it has to be noted that a slightly different approach where the small variation in the slope of the proton spectrum for high injection rates is taken into consideration only leads to minor differences in the absolute line fluxes compared to the calculation method introduced above (cf. Summa 2011).

From the calculations and statements in the previous paragraphs, the following conclusions can be drawn. If CRs are accelerated due to the interaction with shocks in the SNR Cas A as indicated by the strong emission at GeV and TeV energies, the unique signatures of nuclear de-excitation lines offer the possibility of gauging models of CR production as well as transport and interaction scenarios. Apart from

providing direct information about the efficiency and the dominant locations of CR acceleration by the total fluxes and the abundances inferred from discrete lines, gamma-ray measurements in the MeV energy range could also be used to determine the yields of spallation products from nuclear collisions. Since these spallation processes affect the abundances of the cosmologically relevant light elements such as Li, Be, and B, this provides a new assessment of their primordial abundances.

The predicted fluxes of the most prominent C and O lines are marginally too low for a detection with the last instrument with enhanced sensitivity in the MeV energy range, the COMPTEL mission. But they would clearly be detectable by a future MeV mission with sensitivities comparable to those of the proposed GRIPS mission (see Greiner et al. 2012 and Fig. 2.8). New possibilities for precision spectroscopy in this energy regime will offer the opportunity to verify or falsify the hadronic acceleration models in SNRs, being a crucial test for the theory of CR acceleration. Due to the evident "sensitivity gap" at MeV energies (cf. Fig. 2.8), an important sector of the high-energy emission of astrophysical objects currently remains unexplored (see also Chapter 3). This underlines the need for and the importance of a future gamma-ray telescope in the MeV energy range.

3 Gamma-ray diagnostics of Type Ia supernovae

In this chapter, focus is placed on SNe of Type Ia and the gamma-ray emission that is produced in the first weeks after explosion. The gamma-ray observables are modelled for two explosion scenarios that are representatives of the two mostly discussed progenitor channels. Diagnostic tools for a distinction of the two SNe Ia models as well as the detection prospects with future telescope missions in the MeV energy range are discussed. The results presented in the following sections are based on Summa et al. (2013).

3.1 Overview

The importance of SNe Ia in astrophysics is mirrored by their influence on a variety of different research fields. Besides their relevance for measuring cosmological distances (see e.g. Riess et al. 1998; Perlmutter et al. 1999 and the discussion in Subsection 1.3.1), the nucleosynthesis processes during the explosion have a major impact on the chemical evolution of galaxies (cf. Kobayashi & Nomoto 2009). Furthermore, SNe Ia are important for the understanding of star formation and galaxy dynamics (e.g. Scannapieco et al. 2008) and they are thought to be possible sources of galactic positrons (cf. Weidenspointner et al. 2006; Prantzos et al. 2011). But the inherent significance of SNe Ia for all these different branches of astrophysics is contrasted by the fact that many questions regarding the detailed progenitor and explosion scenarios still remain open. Although it is generally agreed that SNe Ia are the result of thermonuclear explosions of C/O WDs, a large variety of evolutionary channels has been proposed that may lead to such an explosion (see Subsection 1.3.2). In this chapter, the gamma-ray line and continuum emission of SNe Ia are studied in order to analyse the relevance of observations in this energy range for the distinction of different explosion models. For this aim to be achieved, for the first time the results of three-dimensional explosion and radiative transfer simulations are used to predict the expected gamma-ray emission of SNe Ia as accurately as possible. Only in a fully three-dimensional approach all multi-dimensional effects of the explosion physics can be taken into account and the distribution of the radioactive isotopes and the surrounding ejecta material can be described realistically. In view of the sensitivity of the gamma-ray emission to peculiarities of these distributions (cf. Section 3.2), a three-dimensional treatment of the explosion

event is also a requirement for a thorough investigation of line-of-sight effects due to different viewing angles towards the SN.

3.2 Gamma-ray emission of Type Ia supernovae

The gamma-ray emission of SNe Ia is dominated by the lines of the decay chain $^{56}\mathrm{Ni} \rightarrow {}^{56}\mathrm{Co} \rightarrow {}^{56}\mathrm{Fe}$. The radionuclei in the expanding SN envelope decay and subsequently de-excite by the emission of gamma rays. At early times after the explosion, the gamma-ray photons interact with the ejected material, undergo Compton scatterings down to X-ray energies, ensuing photoelectric absorptions as well as pair production events, and also power the emission in other wavelength regimes (see also Subsection 1.3.1). During the further expansion of the SN ejecta, the opacity decreases and the photons are no longer completely trapped. Some of the photons begin to escape without scattering and the resulting lines are Doppler-broadened by the velocity spread of the radionuclei in the expanding nebula. The rise time of the gamma-ray emission therefore depends on the kinematics of the ejecta, the distribution and the mass and density profile of the radioactive isotopes. When the ejected material becomes optically thin to gamma-ray photons, the line fluxes are proportional to the decay curves of the isotopes and their total production yields. While the emissivity in the optical or infrared wavelength regime depends strongly on the complex opacity structure which in turn depends on the detailed atomic level populations and the chemical composition, the emissivities of gamma-ray lines are directly determined by their branching ratios and radioactive half-lives. Furthermore, only a few rather simple interaction processes like pair-production, Compton scattering, and photoelectric absorption have to be taken into account for the radiative transfer calculations. This is why especially the emission in the gamma-ray regime is well-suited for getting a direct handle on the mass-velocity distribution of the explosion products (cf. Milne et al. 2004).

Due to these very promising properties, numerous theoretical efforts (mostly one-dimensional) have been taken to investigate the gamma-ray emission of SNe Ia (see for example Clayton et al. 1969; Clayton 1974; Ambwani & Sutherland 1988; Chan & Lingenfelter 1988, 1990, 1991; Burrows & The 1990; Müller et al. 1991; Höflich et al. 1992; Kumagai & Nomoto 1997; Gómez-Gomar et al. 1998; Höflich et al. 1998; Sim & Mazzali 2008; Kromer et al. 2010; Maeda et al. 2012). However, the low sensitivities or the non-existence of detection instruments in this energy range have made a thorough analysis of the MeV emission very difficult up to now. Therefore, in this chapter the additional benefits of the analysis of gamma-ray spectra towards a more sound theoretical understanding of SNe Ia are explored in the context of the detection limits of proposed next generation gamma-ray observatories. For that purpose, full detector simulations of the proposed MeV satellite GRIPS (Greiner et al. 2012) are used to discuss the detection prospects of the gamma-ray emission of SNe Ia.

3.3 Three-dimensional simulations of Type Ia supernova explosions

In the following, the focus is on two main branches of suggested SN Ia progenitor models: The explosion of a near-Chandrasekhar mass WD and the violent merger of two lower-mass WDs. The first model represents the single-degenerate scenario where a WD accretes mass from a stellar companion until it reaches the Chandrasekhar mass limit and explodes. The second model is attributed to the double-degenerate scenario. Here, energy losses due to the emission of gravitational waves in a binary system of two WDs lead to a merger and a subsequent thermonuclear explosion (cf. Subsection 1.3.2). Although there are significant differences in the total mass and the ejecta structure, the predicted optical observables of both models are similar to those of normal SNe Ia (Mazzali et al. 2007; Kasen et al. 2009; Blondin et al. 2011; Pakmor et al. 2012b; Röpke et al. 2012; Sim et al. 2013) and a clear distinction between the two competing explosion scenarios based on the optical emission alone seems to be difficult (e.g. Röpke et al. 2012). Further possibilities for distinguishing SNe Ia explosion models by means of their gamma-ray emission would therefore provide an additional tool to answer the question of the progenitors of SNe Ia. In the next two paragraphs, the applied three-dimensional explosion and radiative transfer simulations are introduced.

3.3.1 Explosion models

In the first simulation, the gamma-ray emission is calculated for the explosion of a near-Chandrasekhar mass WD as a delayed detonation (cf. Khokhlov 1991 and Subsection 1.3.2). Here, the nuclear burning proceeds in two different stages. An initial subsonic deflagration phase is followed by a supersonic detonation phase, and both phases are characterised by different burning products. While iron group elements are mainly produced during the deflagration phase, the remaining fuel is mostly burned to intermediate mass elements during the detonation phase since the energy release of the deflagration mode leads to an expansion of the star and hence to lower densities. In order to allow for conclusions concerning the gamma-ray emission of the major part of SNe Ia, the so-called N100 model is used. This model produces optical observables that are similar to those of "normal" SNe Ia and belongs to a larger set of three-dimensional delayed-detonation simulations carried out with the thermonuclear SN code Leafs (see Seitenzahl et al. 2013b). For a detailed description of the simulation techniques, the reader is referred to Reinecke et al. (1999); Röpke & Hillebrandt (2005); Schmidt et al. (2006); Röpke & Niemeyer (2007).

The general properties of the N100 model can be summarised as follows. For the initial setup, an isothermal non-rotating WD in hydrostatic equilibrium with a central density of $\rho_c = 2.9 \times 10^9\,\mathrm{g\,cm^{-3}}$ is constructed and a chemical composition con-

sisting of 47.5 % ^{12}C, 50.0 % ^{16}O, and 2.5 % ^{22}Ne by mass is assumed. This results in an electron fraction that is comparable to that of a zero-age main sequence star like the Sun and amounts to $Y_e = 0.498864$. To ignite the initial deflagration, 100 spherical sparks are placed randomly in the central area of the WD (cf. Seitenzahl et al. 2013b). Following the results of Woosley et al. (2009), the transition of the flame to a detonation is initiated in every grid cell where the conditions of a fuel density in the range of $(0.6 - 0.7) \times 10^7\,\mathrm{g\,cm^{-3}}$ and of turbulent velocity fluctuations greater than $10^8\,\mathrm{cm\,s^{-1}}$ persisting for sufficiently long time at sufficiently large flame areas are fulfilled. The deflagration and detonation fronts are described as separate discontinuities comparting the material in burned and unburned phases. The propagation of the different burning modes is traced with a level-set scheme (Reinecke et al. 1999; Osher & Sethian 1988; Smiljanovski et al. 1997). To allow for a simulation up to the homologous expansion phase of the ejecta, which is reached roughly 100 s after the explosion, the inner and outer regions of the WD are discretised with two grids of different structure and resolution. Here, the moving mesh technique developed by Röpke (2005); Röpke et al. (2006b) is applied. The total grid size amounts to $512 \times 512 \times 512$ cells.

During the simulation, 10^6 tracer particles reproducing the underlying density profile of the WD record the thermodynamic conditions during the explosion. The information provided by the tracer particles is then used for the calculation of the detailed isotopic abundances with a reaction network of 384 nuclides in a subsequent post-processing step (cf. Travaglio et al. 2004; Röpke et al. 2006a; Seitenzahl et al. 2010). With a kinetic energy of 1.45×10^{51} erg and a total mass of $1.40\,\mathrm{M_\odot}$ of the ejecta, the N100 model produces $0.604\,\mathrm{M_\odot}$ of ^{56}Ni. Roughly half of the ^{56}Ni is located in the inner $0.3\,\mathrm{M_\odot}$ at velocities below $4000\,\mathrm{km\,s^{-1}}$. The other half is more or less isotropically but inhomogeneously distributed within the remainder of the inner $\sim 1.2\,\mathrm{M_\odot}$ up to velocities of $12,000\,\mathrm{km\,s^{-1}}$ (see Fig. 3.1). The yield distributions produced by this method then act as input for the calculations of light curves and spectra with the radiative transfer code (see Subsection 3.3.2).

The second simulation describes the violent merger of a $1.1\,\mathrm{M_\odot}$ and a $0.9\,\mathrm{M_\odot}$ WD (cf. Pakmor et al. 2012b). Similar to the delayed-detonation scenario described above, this model reproduces the features of "normal" SNe Ia at optical wavelengths reasonably well (Röpke et al. 2012). The inspiral and the merger of the two WDs, which are constructed from a total of 1.8×10^6 particles of equal mass, are modelled with a modified version of the SPH code Gadget (Pakmor et al. 2012a). After an initial relaxation phase, the distance between the WDs is slowly decreased according to the method of Dan et al. (2011). When the first particle of the less massive (secondary) WD reaches the Lagrangian point between the two objects, the actual simulation starts. As more and more material from the secondary WD is accreted and heated up on the surface of the primary, hot spots form and the ignition of C burning can be triggered. Microscopic detonation simulations show that a detonation is initiated in such a hot spot if the temperature exceeds $2.5 \times 10^9\,\mathrm{K}$ and density values of about $2 \times 10^6\,\mathrm{g\,cm^{-3}}$ are reached (Seitenzahl et al. 2009a). If these conditions are

fulfilled in a hot spot, the actual simulation is mapped to a uniform Cartesian grid with $768 \times 768 \times 768$ cells and a total box size of 4×10^9 cm. The simulation of the detonation flame is then performed with the LEAFS code and the detonation is ignited at the cell with the highest temperature. For additional information about the simulation details, the reader is referred to Pakmor et al. (2012b).

The isotopic abundances in the ejecta are calculated again in a post-processing step by the use of the tracer particle method and a large nuclear reaction network as described above. The initial chemical composition of the WDs is assumed to be the same as in the delayed-detonation model (47.5 % ^{12}C, 50.0 % ^{16}O, and 2.5 % ^{22}Ne by mass). With an asymptotic kinetic explosion energy of 1.7×10^{51} erg and a combined initial mass of 2.0 $M_\odot$, the produced mass of ^{56}Ni amounts to 0.616 $M_\odot$ (see Fig. 3.1). In contrast to the results of the delayed-detonation model N100, the ^{56}Ni is mainly found at velocities below $\sim 10,000\,\mathrm{km\,s^{-1}}$. Since the delayed explosion of the secondary WD into the already burned remains of the primary excavates a region virtually free of iron group elements at low velocity, the ^{56}Ni is much more asymmetrically distributed than in the delayed-detonation model (cf. Fig. 3.1).

3.3.2 Radiative transfer

In order to follow the emission, propagation, and interaction of the gamma-ray photons, the isotopic abundance distributions determined by the tracer particle method are mapped to a $50 \times 50 \times 50$ Cartesian grid and the resulting gamma-ray emission is calculated with the Monte Carlo radiative transfer code ARTIS (Sim 2007; Kromer & Sim 2009). Monte Carlo methods allow for an efficient simulation of the transport microphysics since even complicated physical processes can be treated easily (cf. Ambwani & Sutherland 1988). The main aspects of the underlying calculation method can be described as follows. Because of several advantages regarding the simulation technique (see e.g. Lucy 1999), the radiation field is divided into so-called "Monte Carlo quanta". Instead of single photons, these quanta represent indivisible parcels of larger amounts of energy. Initially, the quanta start as so-called pellets of radioactive material. Other nuclei apart from ^{56}Ni, ^{56}Co, ^{52}Fe, and ^{48}Cr are not taken into account in ARTIS since they are not important at early times after explosion. Following the laws of radioactive decay, the pellets are converted to mono-chromatic gamma-ray packets that are emitted into randomly chosen directions. Thereby, an isotropic emission in the comoving coordinate frame is assumed and the frequencies are sampled randomly according to the respective branching ratios. Until the gamma-ray packets leave the ejecta or are removed from the gamma-ray regime due to interaction processes, their propagation is followed in frequency, three-dimensional space, and time.

Besides Compton scattering, the most dominant interaction channel of gamma-ray photons in the encountered energy ranges (Milne et al. 2004), photoelectric absorption and pair production are taken into consideration as basic interaction

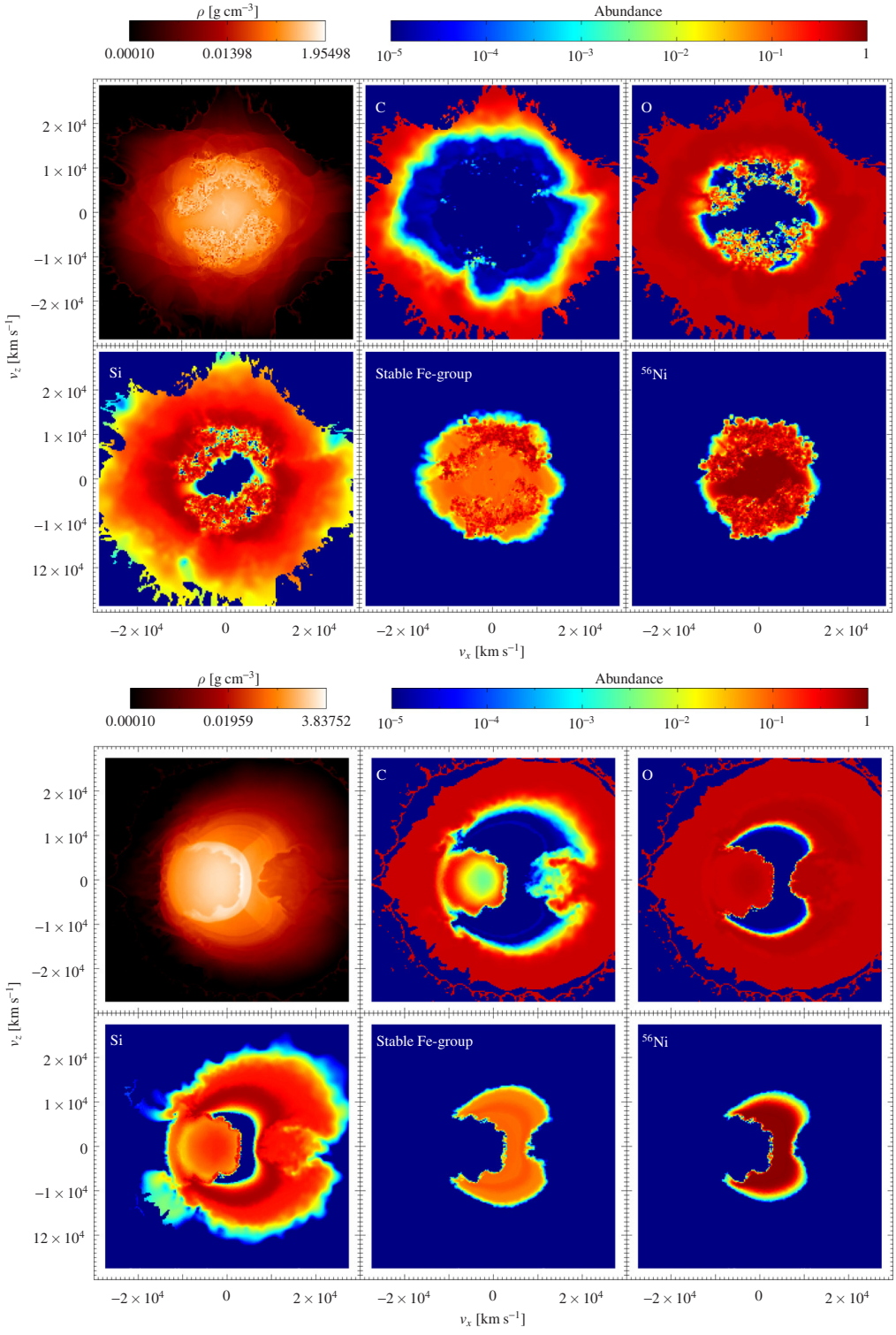

Figure 3.1: Slices through the delayed-detonation model N100 (upper panel) and the violent merger model (lower panel) in the xz-plane showing the density (top left in each panel) and the abundance distribution of selected species at 100 s after explosion (taken from Röpke et al. 2012).

processes. The occurrence of a certain interaction type is sampled randomly in accordance with the ratios of the cross sections of individual interaction processes to the total cross section. Throughout the simulation it is assumed that positrons (for example from pair production or nuclear decays) annihilate in situ and directly lead to the production of two gamma-ray photons at 0.511 MeV (cf. Milne et al. 2004), therefore the positron fraction is always zero. The gamma-ray packets that escape from the ejecta are binned in frequency, time, and direction. For the calculation of the gamma-ray emission from the explosion event, light-travel times are additionally taken into account. Further details on the employed Monte Carlo radiative transfer scheme can be found in Lucy (2005); Sim (2007); Sim & Mazzali (2008); Kromer & Sim (2009).

3.4 Gamma-ray observables of Type Ia supernova explosion models

Although the Chandrasekhar mass delayed detonation and the violent merger are very different with respect to their total mass and the ejecta structure, both models produce the same mass of ^{56}Ni ($\sim 0.6\,M_\odot$) and have similar optical properties. A comparison of the simulated and the measured optical spectra for the recently observed SN 2011fe shows that a direct conclusion on the underlying explosion scenario cannot easily be given (Röpke et al. 2012). In the following, the gamma-ray emission of the two models is further investigated and the connections between distinct observable features and certain characteristics of the explosion models are discussed.

3.4.1 Gamma-ray spectra

The spectral evolution of the angle-averaged gamma-ray emission for the delayed-detonation and violent merger model can be inferred from Figs. 3.2 and 3.3. Both here and hereafter, photon fluxes are always normalised to a distance of 1 Mpc. The spectra of both models are dominated by lines of the decay chain $^{56}\mathrm{Ni} \rightarrow {}^{56}\mathrm{Co} \rightarrow {}^{56}\mathrm{Fe}$. The variations of the line fluxes with time can be understood if the different half-lives of ^{56}Ni (6.1 d) and ^{56}Co (77.2 d) are taken into account. For example, the ^{56}Ni lines at 0.812 MeV or 1.562 MeV are clearly visible at early epochs. According to the decreasing amounts of ^{56}Ni, these lines vanish in the spectra at later times. At these epochs, the spectra are dominated by strong emission lines of ^{56}Co and a continuum contribution caused by Compton scattering processes of line photons. The efficiency of Compton scattering processes is mainly affected by the column density of target electrons. The energies of gamma-ray photons in the MeV range are significantly higher than the respective binding energies of electrons in atoms. This is why nearly all electrons, regardless if they are in bound or unbound state, are possible targets of Compton scattering processes. Compared to the continuum

fluxes, the line fluxes increase with time since the expansion of the ejecta leads to a reduction of the optical depths.

In addition to these common features in the spectral evolution, both models also exhibit distinct properties. At 20.1 d and 34.9 d after the explosion, two prominent lines of ^{56}Ni at 0.158 MeV and 0.270 MeV can only be identified in case of the delayed-detonation model. In the merger model, these two lines are nearly totally degraded and vanish in the background of continuum emission. This difference between the two models emerges because of the energy sensitivity of the Compton cross section. Due to the decline of the cross section with increasing photon energy, especially line photons at low energies experience many Compton down-scatterings. Furthermore, these low-energy lines are further contaminated by photons that are likewise down-scattered from higher energies. These effects directly connect the occurrence of low-energy lines of ^{56}Ni to the distribution of the radioactive material. Only if a significant amount of ^{56}Ni is located at small optical depths, the two lines at 0.158 MeV and 0.270 MeV can build up. This is the case for the delayed-detonation model where much more ^{56}Ni is situated at higher velocities than in the merger model (see Fig. 3.1). Since the amount of material surrounding the ^{56}Ni regions is smaller in the delayed-detonation model, the corresponding column densities are lower than in the merger scenario, and the gamma-ray emission of the delayed-detonation model evolves faster. While this property cannot easily be inferred from measurements in other wavelength regimes (see Röpke et al. 2012), it is clearly mirrored in the evolution of the gamma-ray emission. Additionally, the merger model displays a softer spectrum due to the larger optical depths outside the ^{56}Ni region leading to more efficient Compton down-scattering. Since iron group elements are confined to lower velocities in the merger, there are fewer photoelectric absorption processes than in the delayed-detonation model and the softening of the spectrum is further enhanced.

The shape of the gamma-ray spectra is of course influenced by the line of sight towards the explosion event. Besides the angle-averaged spectra, Fig. 3.3 illustrates the effects of different viewing angles for the maximum-light epochs of the two models in gamma rays. It can be seen that the strongest lines of the delayed-detonation model do not show much variation. In the merger model, the dependence on the viewing angle is more prominent and the asymmetric structure of the ejecta causes spectral features of varying magnitude. In particular in the continuum, part of the effect is obscured by Monte Carlo noise. This problem can be avoided by using hardness ratios and broadband light curves (see below). It has to be noted that the spread of the gamma-ray spectra can prevent a distinction of the two models for certain viewing angles. In face of viewing-angle effects, especially the low-energy range of the spectra seems to be quite promising concerning a distinction of the two models. The higher column densities due to the larger total mass of the merger model lead to more effective Compton down-scattering processes than in the delayed-detonation model. Therefore, prominent low-energy lines of ^{56}Ni cannot form and serve as distinguishing feature between the two models.

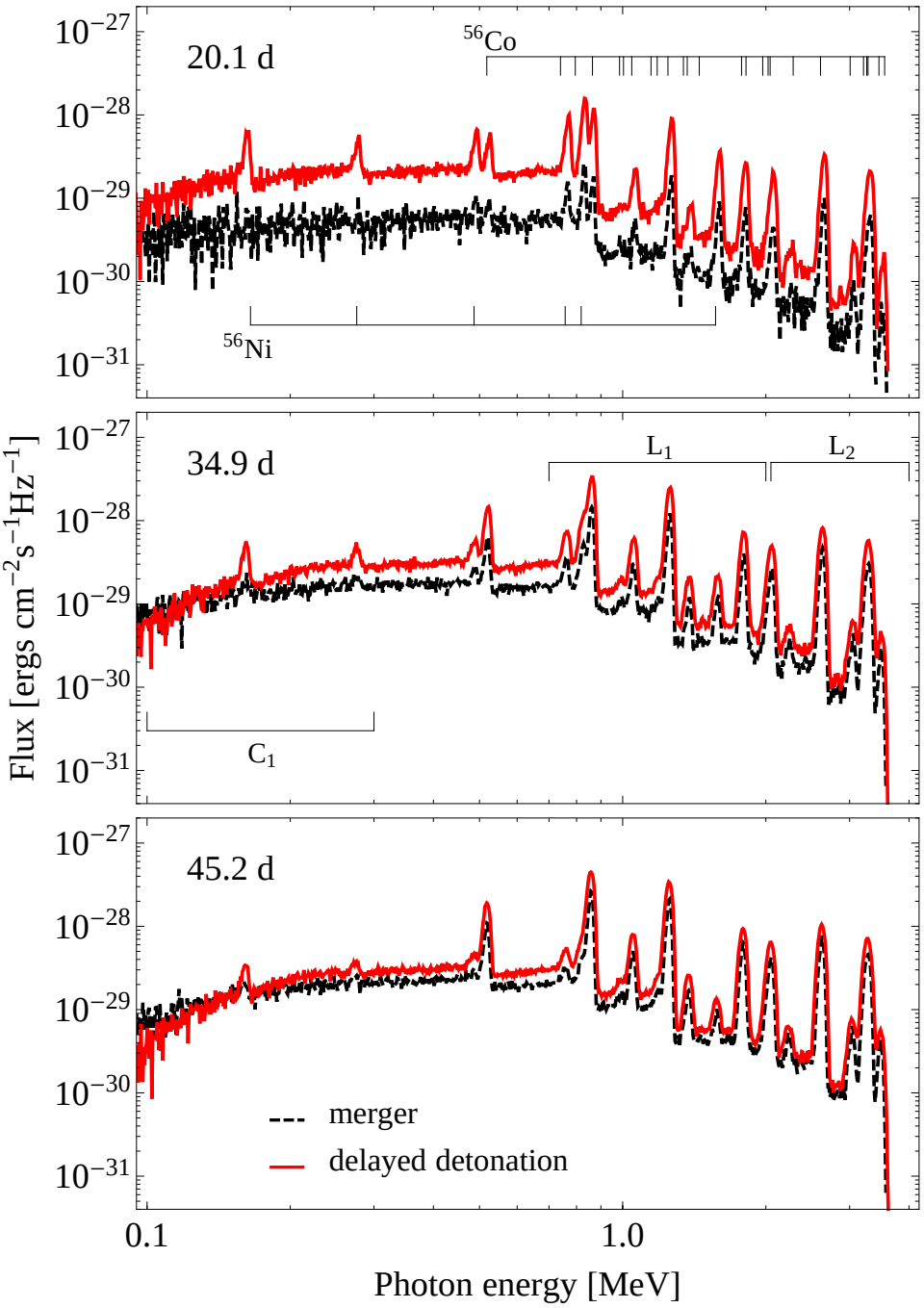

Figure 3.2: Temporal evolution of the gamma-ray emission from the delayed-detonation (red) and the violent merger model (dashed black). The different epochs after the explosion are indicated in the upper left of each panel. The ^{56}Ni and ^{56}Co emission lines are depicted in the first panel, the flux bands discussed in Subsections 3.4.3 and 3.4.4 can be inferred from the second panel (taken from Summa et al. 2013).

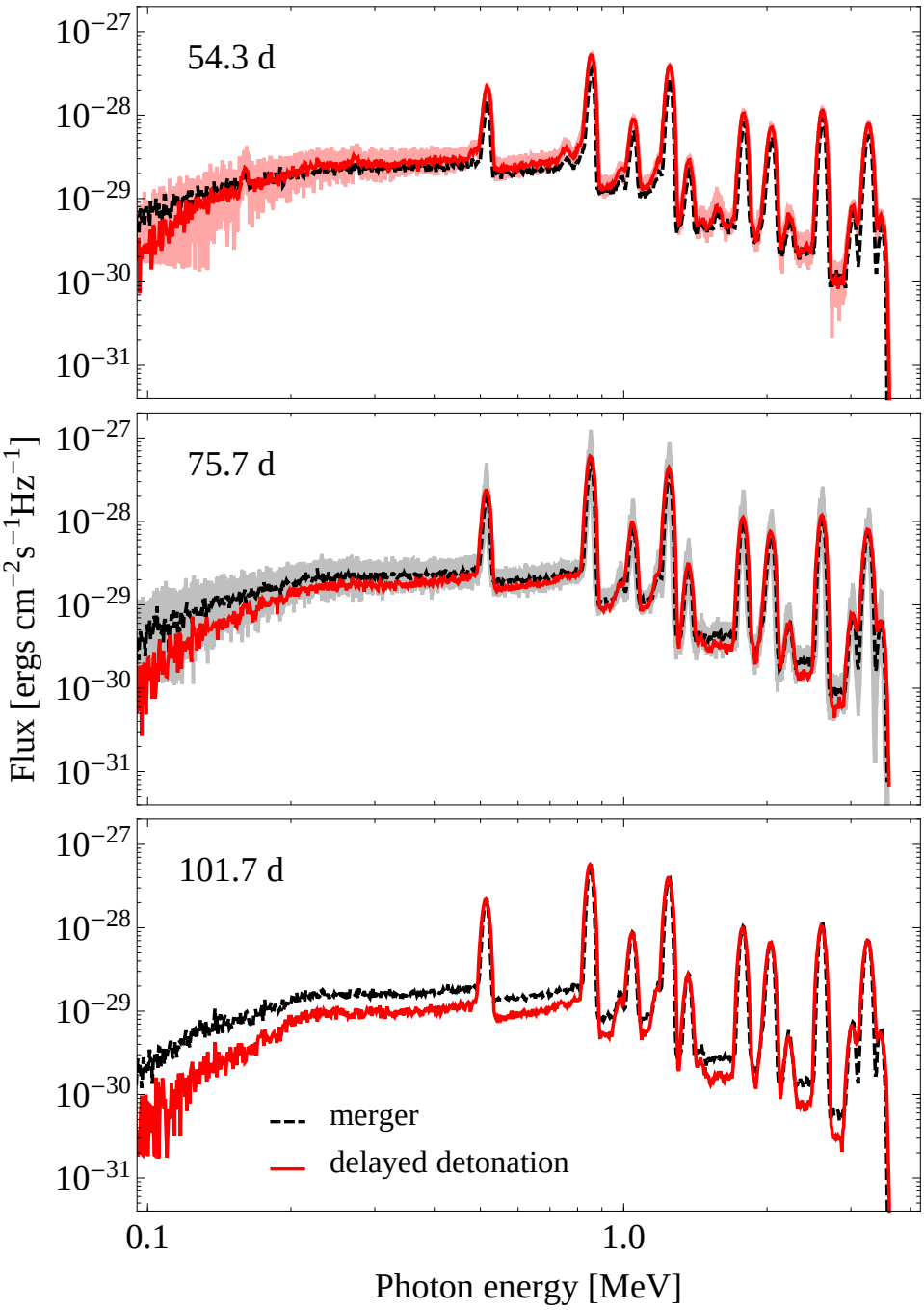

Figure 3.3: Temporal evolution of the gamma-ray emission from the delayed-detonation (red) and the violent merger model (dashed black). The different epochs after the explosion are indicated in the upper left of each panel. The spectral spread due to different viewing angles is shown for the maximum-light epochs of the two models in gamma rays and indicated in light red and grey (taken from Summa et al. 2013).

3.4.2 Light curves

A comparison of the bolometric (energy range from 0.05 MeV to 4.0 MeV) gamma-ray light curve of the two models shows that the merger model reaches its maximum flux values significantly later than the delayed-detonation model (see Fig. 3.4, upper panel). While the delayed-detonation model yields a peak photon flux of $1.82 \times 10^{-2}\,\mathrm{cm^{-2}\,s^{-1}}$ at 54.3 d, the violent merger model arrives at a maximum flux of $1.43 \times 10^{-2}\,\mathrm{cm^{-2}\,s^{-1}}$ at 75.7 d after the explosion. In analogy to the differences in the temporal evolution of the gamma-ray spectra, this behaviour can be accounted for by the different amounts of material above the radioactive isotopes. Since the masses of the produced ^{56}Ni are nearly equal in both models, the transport of gamma-ray photons is, to first order, only sensitive to the respective column densities. Due to the larger total mass in the merger, the gamma-ray emission is delayed and a lower (angle-averaged) peak flux than in the delayed-detonation model is reached. Furthermore, late-time measurements of gamma-ray luminosities are well-suited for unambiguously determining the explosion yield of ^{56}Ni. According to Sim & Mazzali (2008), the gamma-ray luminosity in the optical thin limit is given by

$$L_\gamma(t \geq t_{\mathrm{thin}}) \approx 1.23 \times 10^{43} \frac{M_{\mathrm{Ni}}}{\mathrm{M}_\odot} \exp\left(-\frac{t}{t_{\mathrm{Co}}}\right) \mathrm{erg\,s^{-1}} \tag{3.1}$$

with the lifetime t_{Co} of ^{56}Co. If the distance to the SN is known, M_{Ni}, the mass of ^{56}Ni, can easily be calculated. In case of the delayed-detonation and the violent merger model, the equality of the ^{56}Ni masses is reflected by the convergence of the bolometric gamma-ray light curves at late times (see Fig. 3.4).

The effects of different lines of sight have also to be discussed in case of light curve measurements. As can be inferred from Fig. 3.4, the merger model exhibits a much larger spread of photon fluxes than the delayed-detonation model. Similar to the properties of the gamma-ray spectra of the merger model, this is a result of the asymmetric ejecta distribution. Nevertheless, a distinction of the two models is still possible. Characteristic features such as the different times of maximum flux or the different early time evolution of the light curves allow conclusions on the underlying explosion model. These differences in the evolution of the light curves have their origin in the different total masses of the two explosion scenarios. Due to the larger total mass of the merger model, there is more efficient photon trapping at earlier times. This results in a delayed rise of the photon flux and a flux peak occurring at later times.

For comparison, the bolometric UVOIR light curves are shown in Fig. 3.4, too. It is evident that a distinction between the delayed-detonation and the merger model is simply not possible for many viewing angles. Thus, the advantages of the bolometric gamma-ray light curves become apparent. Although the flux spread due to different lines of sight towards the SN is comparable to that of UVOIR light curves, especially early time measurements and the determination of the maximum fluxes are very promising with respect to a clear distinction of the explosion models. This makes

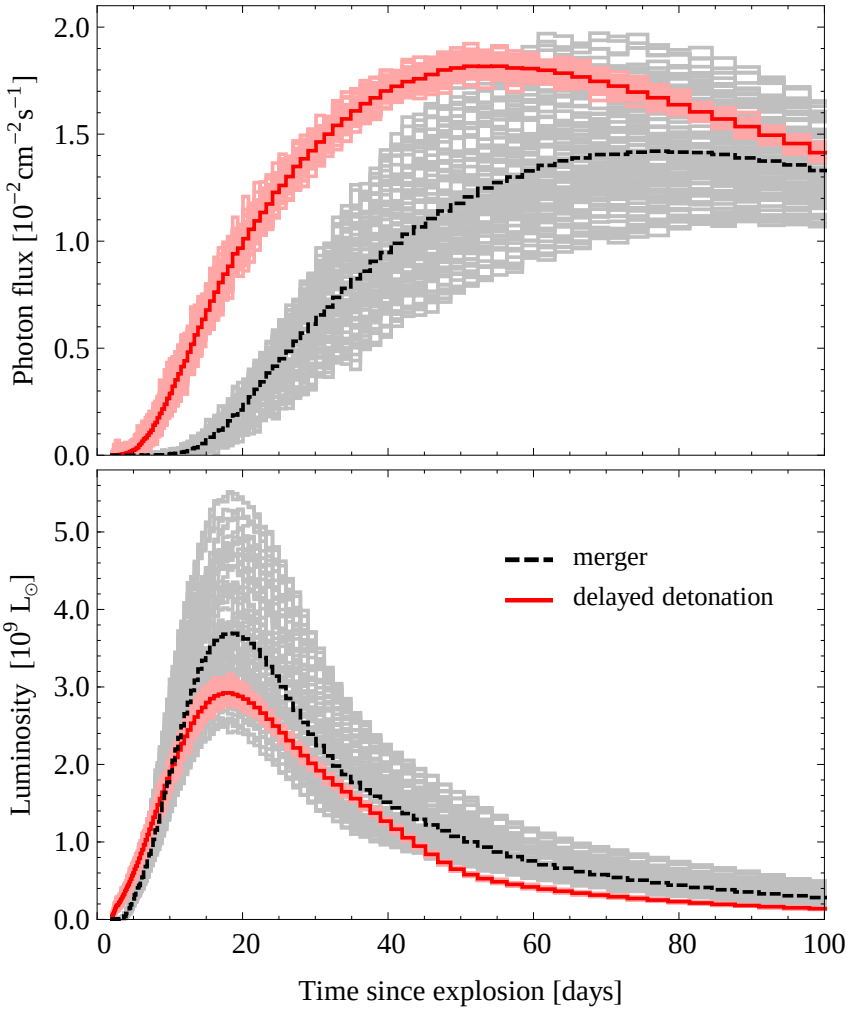

Figure 3.4: Bolometric gamma-ray light curve (upper panel) and bolometric UVOIR light curve (lower panel) for the delayed-detonation (red) and the violent merger model (dashed black). The spread of photon fluxes resp. luminosities due to different viewing angles is indicated in light red and grey. All values are normalised to a distance of 1 Mpc to the explosion event (taken from Summa et al. 2013).

gamma-ray observations of SNe Ia an important complementary tool in addition to studies in other wavelength ranges.

3.4.3 Line ratios

Besides the analysis of spectral lines and light curves, additional diagnostics such as line and hardness ratios can be applied for the study of the gamma-ray emission of SNe Ia (cf. Höflich et al. 1998; Gómez-Gomar et al. 1998; Sim & Mazzali 2008). In contrast to absolute flux values, which always depend on the accuracy of distance measurements, flux ratios can also be determined if the exact distance to the SN is not known and they are therefore not subject to this limitation. In accordance with Sim & Mazzali (2008), two characteristic peak-intensity line ratios are defined that are investigated further in the following. $R_1 = F(0.847\,\mathrm{MeV})/F(2.598\,\mathrm{MeV})$ denotes the ratio of two ^{56}Co lines, $R_2 = F(0.158\,\mathrm{MeV})/F(0.847\,\mathrm{MeV})$ is the ratio of a ^{56}Ni and a ^{56}Co line. The temporal evolution of these two line ratios for the delayed-detonation and the merger model is depicted in Fig. 3.5.

Similar to gamma-ray spectra and light curves, flux ratios are affected by the same mechanisms described in the previous paragraph. At early times before the optically thin limit, line ratios depend on the amount of material above the emission region. The higher the column density of electrons is, the more interaction processes of gamma-ray photons take place. Since Compton scatterings are the dominant interaction processes in the MeV energy range, the decisive factor is thereby the energy sensitivity of the Compton cross section. If two lines belong to the same radioactive isotope, the ratio of the two lines is simply determined by the opacities at the respective line energies.

An example of such a line ratio is R_1, its evolution with time for both explosion models is depicted in the upper panel of Fig. 3.5. Due to a higher abundance of ^{56}Ni and hence of ^{56}Co at lower optical depths, the line ratio R_1 reaches significantly larger values shortly after explosion in the delayed-detonation scenario. In the merger model, the radioactive material is behind much more opacity, which results in a lower value of R_1. As a consequence of the same mass of initially produced ^{56}Ni, the line ratios of the two models start to converge when the ejecta become more and more dilute at later times after explosion. It has to be noted that it is not necessary to choose two specific lines to get information about intrinsic model characteristics. The requirement for the diagnostic validity of an R_1-type line ratio is a selection of two lines that present a sufficient spread between their line energies, since only then the energy sensitivity of the Compton cross section leads to a pronounced observable effect (see also Sim & Mazzali 2008).

If a line ratio consists of two lines from different isotopes, the evolution of the line ratio is further determined by the different half-lives of the isotopes. This is shown for the line ratio R_2 in the lower panel of Fig. 3.5. Due to the longer half-life of ^{56}Co, the line at 0.847 MeV strengthens whereas the 0.158 MeV line of ^{56}Ni fades

away at later times. Therefore, R_2 decreases with time. The diagnostic value of R_2 is additionally based on the different origins of the two lines. While the 0.847 MeV line originates from the total abundance of ^{56}Co in the ejected material, only the ^{56}Ni in the outer shells can be responsible for the emission at 0.158 MeV. Due to the increasing Compton cross section at smaller energies (see also the discussion in Subsection 3.4.1), nearly all line photons at higher optical depths undergo Compton scattering processes, suffer from energy losses, and cannot contribute to the total line flux at 0.158 MeV. Indicating a larger deposit of ^{56}Ni in the outer layers, R_2 clearly reflects the different distributions of this isotope in the two models.

Because of its low energy, the ^{56}Ni line at 0.158 MeV is also very sensitive to photoelectric absorption processes. Photoelectric opacities are influenced by the compositional structure of the ejecta above the radioactive material and especially ratios of low-energy ^{56}Ni lines to ^{56}Co lines are very appropriate for studying the composition of SNe Ia. The identification of distinct abundance features of course relies on the quality of the available gamma-ray data and therefore depends on the distance of the explosion event (see also Section 3.5).

3.4.4 Hardness ratios

If the quality of gamma-ray data does not allow for a detailed study of spectral lines, hardness ratios are an additional tool that can be used to infer information about the underlying explosion scenario. Instead of a ratio of discrete line intensities, the fluxes in broader energy bands are compared. Although being a coarser method for investigating the gamma-ray emission of SNe Ia, hardness ratios are especially useful in this energy regime. In contrast to other wavelength ranges, the loss of information is minimised by the relative simplicity of gamma-ray spectra and the small number of factors that influence gamma-ray emission processes. For the following discussion, the hardness ratios $H_1 = C_1/L_1$ and $H_2 = L_1/L_2$ are defined in analogy to Sim & Mazzali (2008). C_1 denotes the energy band from 0.1 MeV to 0.3 MeV, the energy bands from 0.7 MeV to 2.0 MeV and 2.0 MeV to 4.0 MeV are labelled with L_1 and L_2. While C_1 is dominated by continuum emission from Compton down-scattering and photo-absorption processes, pronounced lines of ^{56}Co can be found in L_1 and L_2. At higher photon energies, the importance of continuum processes decreases.

As it is the case with line ratios, the determining factor for hardness ratios is the energy dependence of the Compton cross section (see Fig. 3.6). By definition, the hardness ratio H_1 compares the strength of the continuum emission in C_1 to that of the discrete lines in L_1. Since more radioactive material is located at higher optical depths in the merger model, the contribution of continuum emission is stronger. This directly translates into a higher H_1 value of the merger model than of the delayed-detonation model. In analogy to the line ratio R_2, H_1 is sensitive to the column density of target electrons above the radioactive material. Due to the enhanced rate of photo-absorption processes in the energy band C_1, the hardness ratio H_1 also

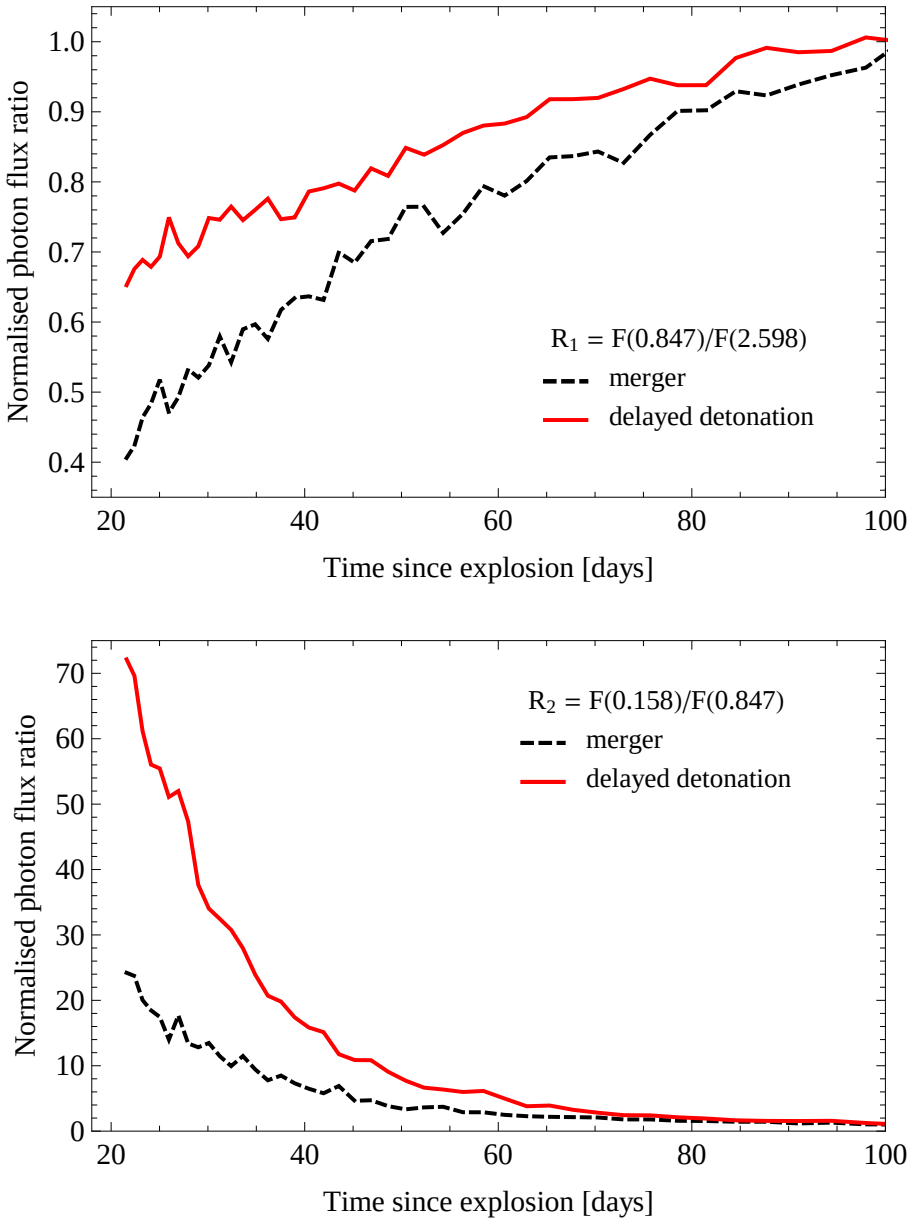

Figure 3.5: Peak line flux ratios of the gamma-ray emission from the delayed-detonation (red) and the violent merger model (dashed black). In the upper panel, the line ratio $R_1 = F(0.847\,\mathrm{MeV})/F(2.598\,\mathrm{MeV})$ of two ^{56}Co lines is depicted. In the lower panel, the line ratio $R_2 = F(0.158\,\mathrm{MeV})/F(0.847\,\mathrm{MeV})$ of a ^{56} Ni and a ^{56}Co line is illustrated. The peak flux ratios are normalised to the optically thin limit (taken from Summa et al. 2013).

mirrors the different compositions of the ejecta to a certain extent. Representing the flux ratio of two line-dominated energy bands, the hardness ratio H_2 is comparable to the line ratio R_1. H_2 is mainly determined by the ratio of the Compton cross sections in the two energy bands L_1 and L_2. Both hardness ratios are well-suited for discriminating the two explosion models. Particularly in view of more distant explosion events, hardness ratios in general offer an alternative opportunity to study the gamma-ray emission of SNe Ia.

As can be inferred from the results shown in Figs. 3.5 and 3.6, line as well as hardness ratios are very suitable as additional diagnostic tools regarding the distinction between the delayed-detonation model and the violent merger model on the basis of their gamma-ray emission. These ratios are mainly influenced by two factors. On the one hand, they are directly linked to the distribution of ^{56}Ni in the ejecta. On the other hand, due to interaction processes of gamma-ray photons such as photo-absorption or Compton scattering, the ratios show a dependence on the column density of target electrons in the material surrounding the radioactive isotopes. This manifests itself in a sensitivity of line and hardness ratios to different compositions and masses of the outer ejecta layers. Of course, possible degeneracies because of line-of-sight effects have to be taken into account. But as can be seen in the upper panel of Fig. 3.6, hardness ratios are very robust in distinguishing the two different explosion models and, especially at later times, interferences do not play a considerable role with respect to the model distinction. If it is difficult to resolve single emission lines accurately, hardness ratios and broadband light curve measurements can provide the best chances of revealing certain features of the underlying explosion model. In order to discuss the diagnostic value of gamma-ray observables in the context of future observations, the results of dedicated detector simulations of the proposed MeV satellite GRIPS are presented in the following section.

3.5 Detection prospects

Although the diagnostic importance of gamma-ray emission in the MeV energy range is evident for many astrophysical objects and processes, the last mission with high sensitivities at these energies was the COMPTEL instrument aboard the CGRO satellite in the mid-1990s. Since then, no successor mission with sensitivities comparable to the sensitivities of instruments in the neighbouring wavelength regimes has been launched. One of the proposals to close the sensitivity gap at MeV energies is the GRIPS (Gamma-Ray Imaging, Polarimetry and Spectroscopy) mission providing a sensitivity enhancement of a factor of 40 compared to COMPTEL (Greiner et al. 2009, 2012 and see also Section 2.6). In this section, the example of GRIPS is used as a prototype for next-generation missions in the MeV energy range and the prospects for the detection of gamma-ray emission from SNe Ia in the near future are studied.

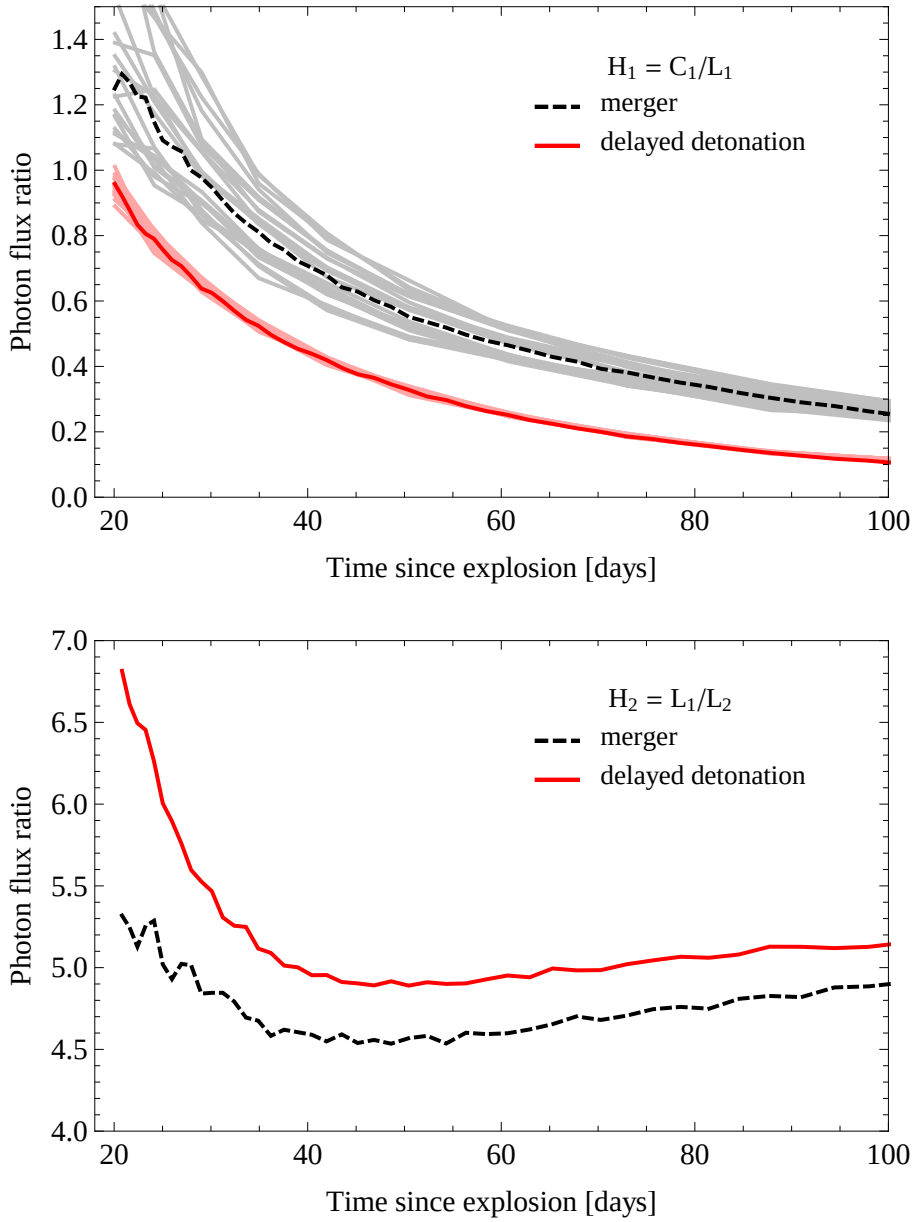

Figure 3.6: Hardness ratios of the gamma-ray emission from the delayed-detonation (red) and the violent merger model (dashed black). The ratio $H_1 = C_1/L_1$ is shown in the upper panel, the ratio $H_2 = L_1/L_2$ is displayed on the right. For an illustration of the sensitivity to viewing-angle effects, H_1 is shown for different lines of sight in light red and grey in the upper panel (taken from Summa et al. 2013).

3.5.1 The GRIPS mission

Being sensitive to photon energies from 0.2 MeV to 80 MeV, the GRIPS mission aims for the search of gamma-ray bursts and blazars, the study of particle acceleration and radiation processes in a variety of cosmic sources (cf. Chapter 2), and the exploration of SN explosion and nucleosynthesis mechanisms. The main instrument aboard the suggested GRIPS satellite is the Gamma-Ray Monitor (GRM, see also Fig. 3.7). It consists of two separate detectors with an effective area of 195 cm^2 and an energy resolution of 17 keV at 1.8 MeV. The detection principle of this combined Compton scattering and pair creation telescope can be summarised as follows. The first detector where the initial interaction of the incoming gamma-ray photons takes place is the so-called tracker made of silicon strips. Except for the entrance surface, the tracker is surrounded by a second detector composed of $LaBr_3$ scintillator material. This calorimeter is responsible for the energy determination of the secondary particles arising from the interaction processes of the gamma-ray photons in the tracker. If a Compton scattering event takes place in the tracker, the incident gamma-ray photon interacts with an electron and the energy and the position of the electron are measured. The scattered photon is recorded in the calorimeter and its energy and its interaction point can be reconstructed. With the use of these data, the determination of the direction and the energy of the incident gamma-ray photon is possible (see also Fig. 3.8). If a pair creation event takes place in the tracker, a conversion of the incident gamma-ray photon into an electron-positron pair occurs in the tracker and the original direction of the gamma-ray photon can be calculated from the tracked directions of the electron-positron pair. Both detectors, the tracker and the calorimeter, are used to measure the energy of the two secondary particles. With these data, the energy of the incident photon can be determined.

To simulate GRIPS measurements of gamma-ray emission from SNe Ia, the MEGAlib software package developed by Zoglauer et al. (2006) is used. Being adjusted to the specific setup of the GRM instrument (see Greiner et al. 2012), this package is based on the Geant4 toolkit (Agostinelli et al. 2003) and calculates the passage of gamma rays and other particles through the detector by taking into account all possible particle interactions and decays. In order to determine the detector response to an incident gamma-ray photon, the energy deposits of the (secondary) particles in sensitive elements such as silicon strips and scintillator crystals are simulated. Additionally, instrumental effects such as energy resolution or noise suppression thresholds enter the calculation. Events that pass the trigger criteria of coincident hits in the silicon strip detector and the calorimeter are further investigated with a dedicated event reconstruction algorithm. If the algorithm cannot reconstruct an event as a valid Compton scattering or pair creation event, the event is rejected and not considered to be part of a detection of a gamma-ray photon. If an event can be reconstructed as Compton scattering process, the direction of the incident gamma-ray photon is constrained to a circle around the direction of the scattered photon.

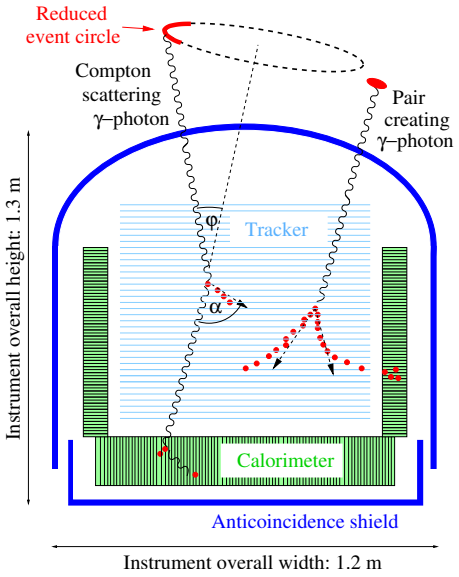

Figure 3.7: Baseline design and measurement principle of the GRM detector that consists of three main parts. In the first subsystem, the tracker, the primary interaction (Compton scattering or pair creation) of the incident gamma-ray photons takes place. The resulting secondaries are stopped and measured in the surrounding second subsystem, the calorimeter. The third subsystem, the anticoincidence shield, recognises particles impinging on the detector (taken from Andritschke 2006).

To ensure that the reconstructed events are compatible with the source position of the photons, several selection criteria are applied. First, a minimum distance between the circle and the source position of less than 2° is required. Second, if the Compton scattering plane can be determined (this is the case for recoil electrons leaving a track in the silicon detector), the rotation angle around the direction of the scattered photon has to be within 30° from the source position.

For an accurate simulation of the detection of gamma-ray photons with GRIPS, all possible radiation backgrounds have to be studied thoroughly. According to Boggs (2006), two components dominate the background emission for a Compton telescope at a low-inclination low Earth orbit: the backgrounds from diffuse cosmic photons and albedo photons produced in the Earth's atmosphere. Both backgrounds are included in the MEGAlib simulations, the respective models and data sets can be found in Gruber et al. (1999) and Mizuno et al. (2004); Ajello et al. (2008). The generated background photons are processed in a way similar to the simulation and selection methods described above. The reconstructed background events and the source events resulting from the predicted spectra of the two explosion models are added. To obtain the final gamma-ray spectra, the same background subtraction methods as for real observations are applied.

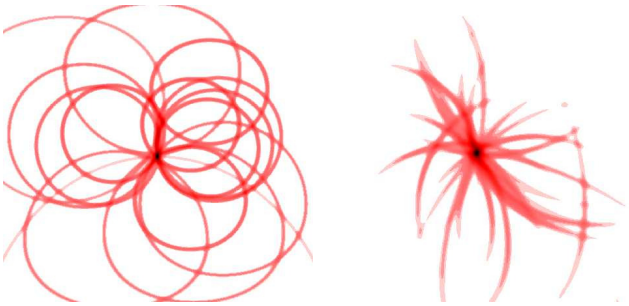

Figure 3.8: Examples of two different Compton event types in the GRM detector. If the energy of the Compton recoil electron is not sufficient to produce a track, the origin of the incident gamma-ray photon can only be restricted to a cone (left). For events with a measured electron track, the origin can be determined to an arc of the cone-section (right, taken from Andritschke 2006).

3.5.2 Results of detector simulations

In view of the sensitivity range of GRIPS, the definition of the hardness ratio H_1 is slightly modified for the detector simulations presented in the following and the ratio $H_1^* = C_1^*/L_1$ is used instead. Here, C_1^* denotes the energy band from 0.2 MeV to 0.4 MeV. Nevertheless, all conclusions drawn in Subsection 3.4.4 concerning H_1 also hold for H_1^*.

In Fig. 3.9, the simulation results for the measured gamma-ray spectra at 25 d after the explosion are shown for the delayed-detonation and the violent merger model. In order to allow for reasonable studies of the time evolution of the spectra, an exposure time of 10^5 s is chosen. Such a time interval corresponds to roughly 5 d in the all-sky scanning mode of GRIPS. For larger source distances, background fluctuations and limited event statistics especially in the high-energy part of the spectrum complicate accurate measurements and affect the validity of line and hardness ratios. In case of the GRIPS instrument, the two explosion models can be distinguished best by the application of the hardness ratio H_1^* (see Fig. 3.10). According to the simulations, a model distinction is possible up to a source distance of 5 Mpc to 7 Mpc. In Fig. 3.11, the results of simulated light curve measurements are depicted. For a SN at a distance of 1 Mpc, the accurate determination of the light curve easily allows inferences on the underlying explosion model. Further investigations of light curve measurements show that a distinction of the two explosion scenarios should be feasible with GRIPS up to source distances of 10 Mpc.

In addition to the simulations with exposure times of 10^5 s (see above), the detector response is also calculated for a significantly longer exposure time of 10^6 s. Due to the time variability of the spectra, such an observation has to be performed in on-axis pointing mode and requires roughly 12 d. As can be seen in Fig. 3.12, for such exposure times the strongest lines at medium and higher energies can still be

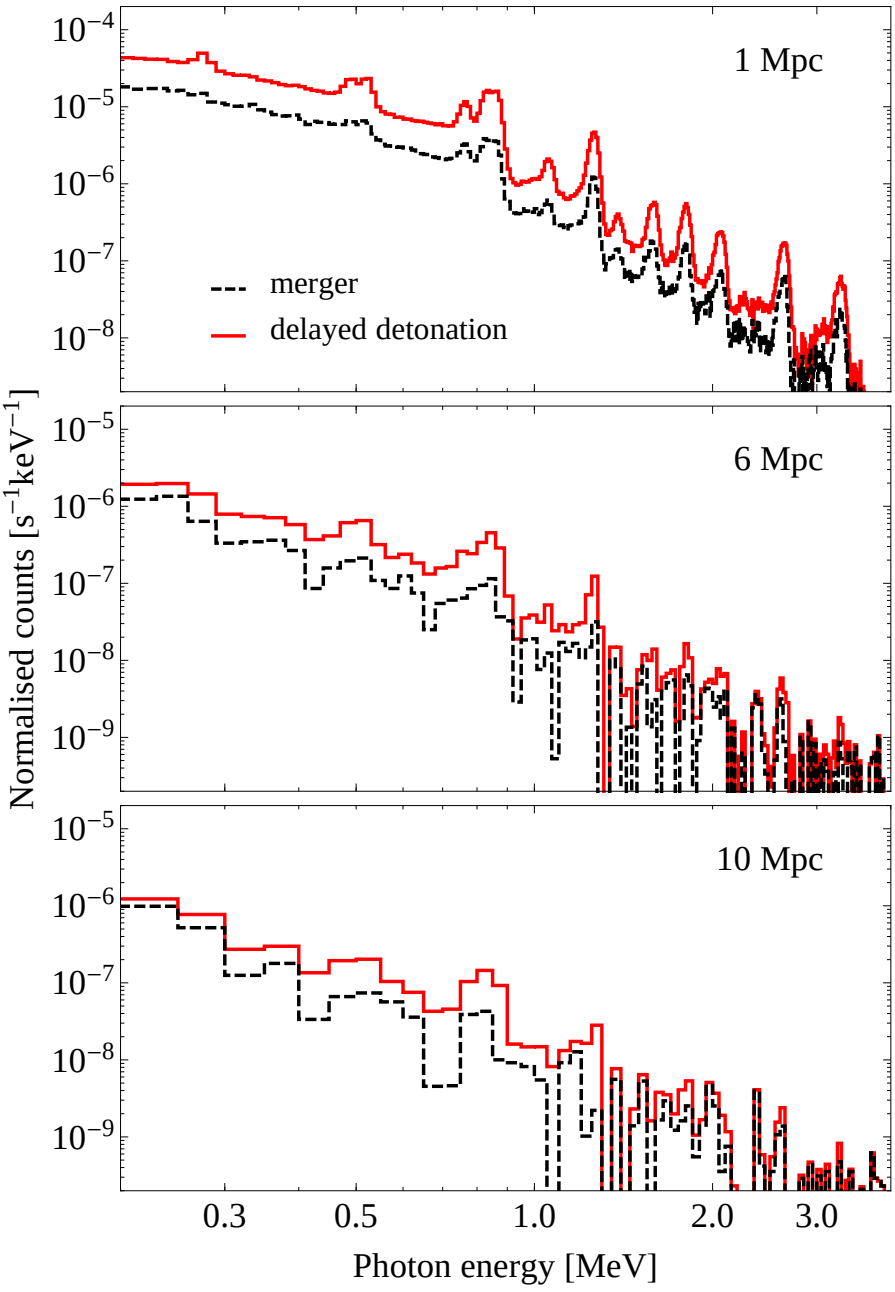

Figure 3.9: Simulated detector response for the GRM instrument aboard GRIPS using an exposure time of 10^5 s. For different distances to the source (indicated in the upper right), a comparison of the simulated angle-averaged gamma-ray spectra of the delayed-detonation (red) and the violent merger model (dashed black) at 25 d after explosion is shown (taken from Summa et al. 2013).

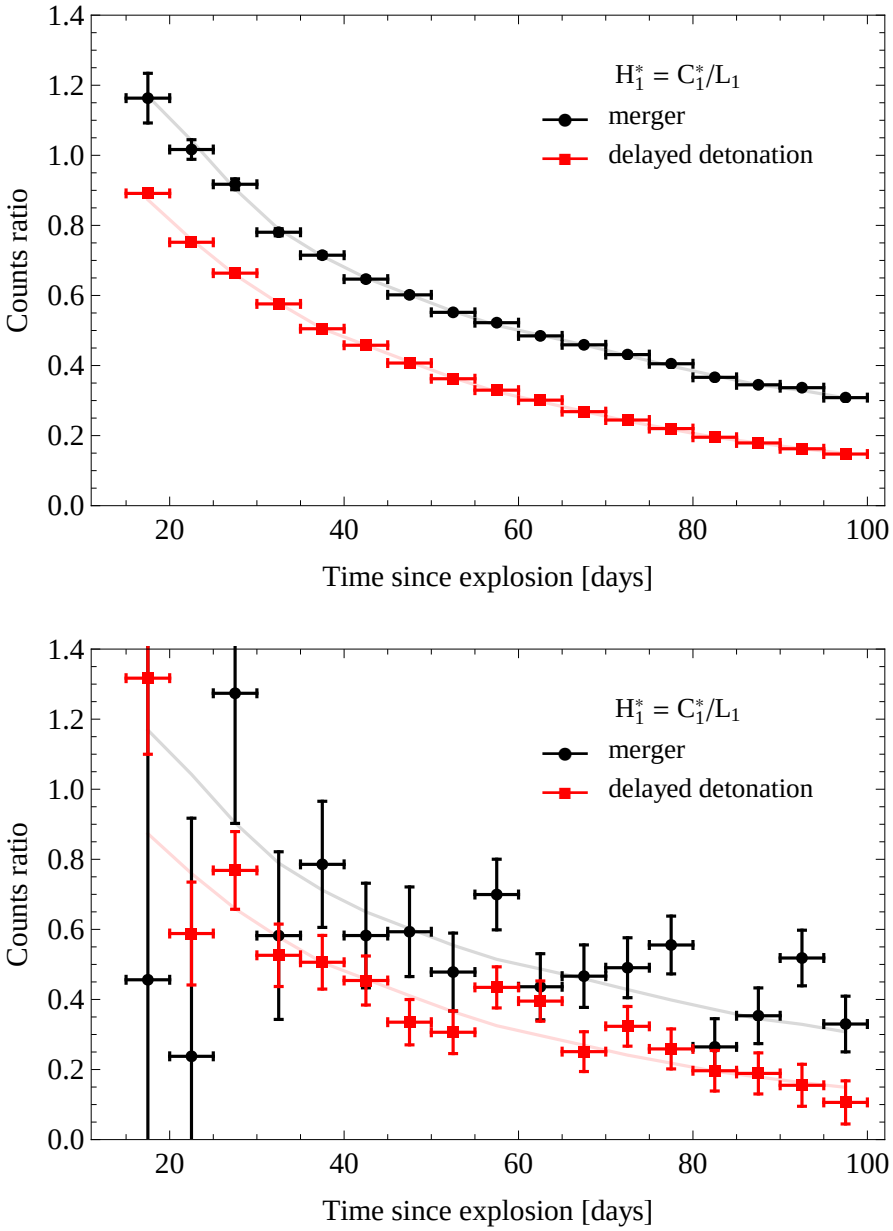

Figure 3.10: Simulation results for hardness ratio measurements with the GRM instrument for the delayed-detonation (red) and the violent merger model (black) and an exposure time of 10^5 s. In the upper panel, a source distance of 1 Mpc is assumed, the lower panel shows the results for a source distance of 5 Mpc. In order to take into account the sensitivity limits of GRIPS, C_1 here denotes the energy band from 0.2 MeV to 0.4 MeV. The solid lines show the results in case of ideal measurements without background fluctuations and statistical errors (taken from Summa et al. 2013).

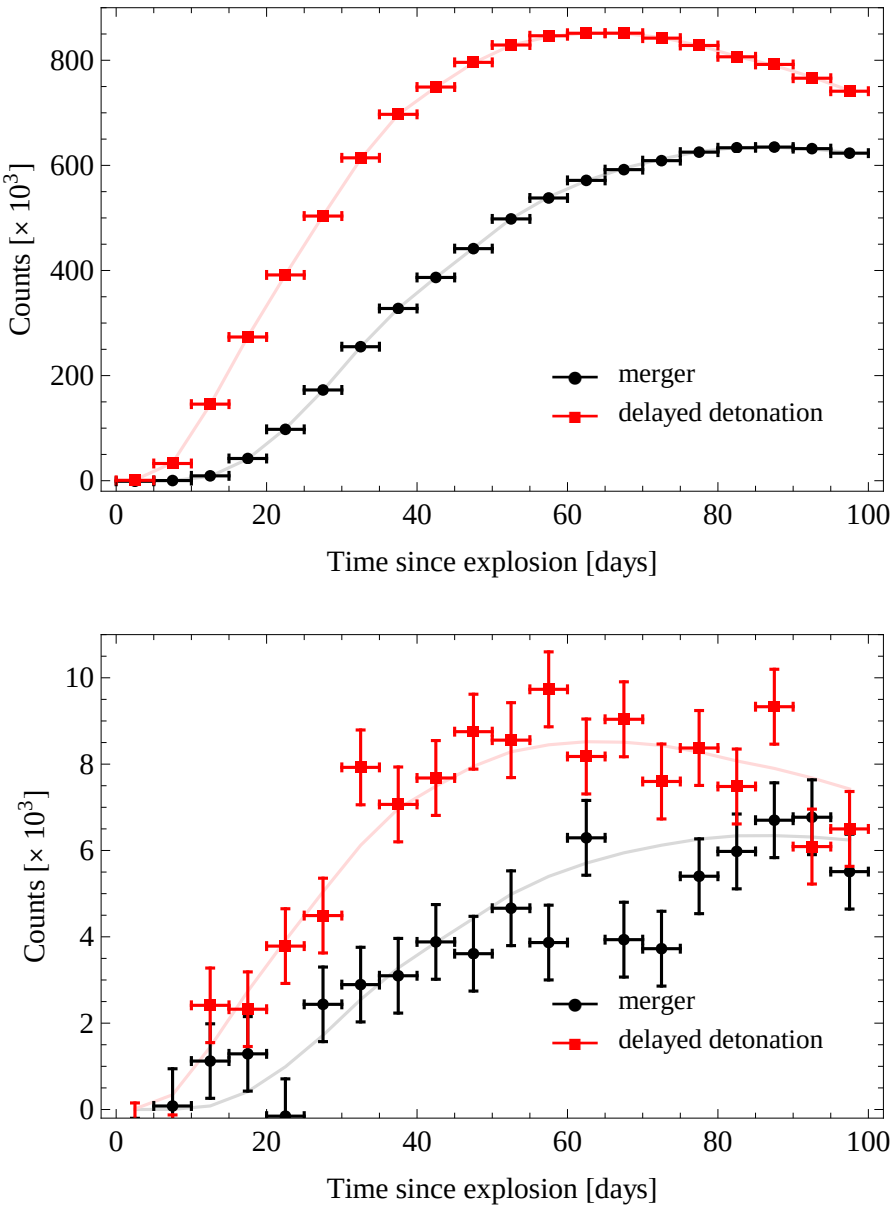

Figure 3.11: Simulation results for light curve measurements with the GRM instrument for the delayed-detonation (red) and the violent merger model (black) and an exposure time of 10^5 s. In the upper panel, a source distance of 1 Mpc is assumed, the lower panel shows the results for a source distance of 10 Mpc. The solid lines show the results in case of ideal measurements without background fluctuations and statistical errors (taken from Summa et al. 2013).

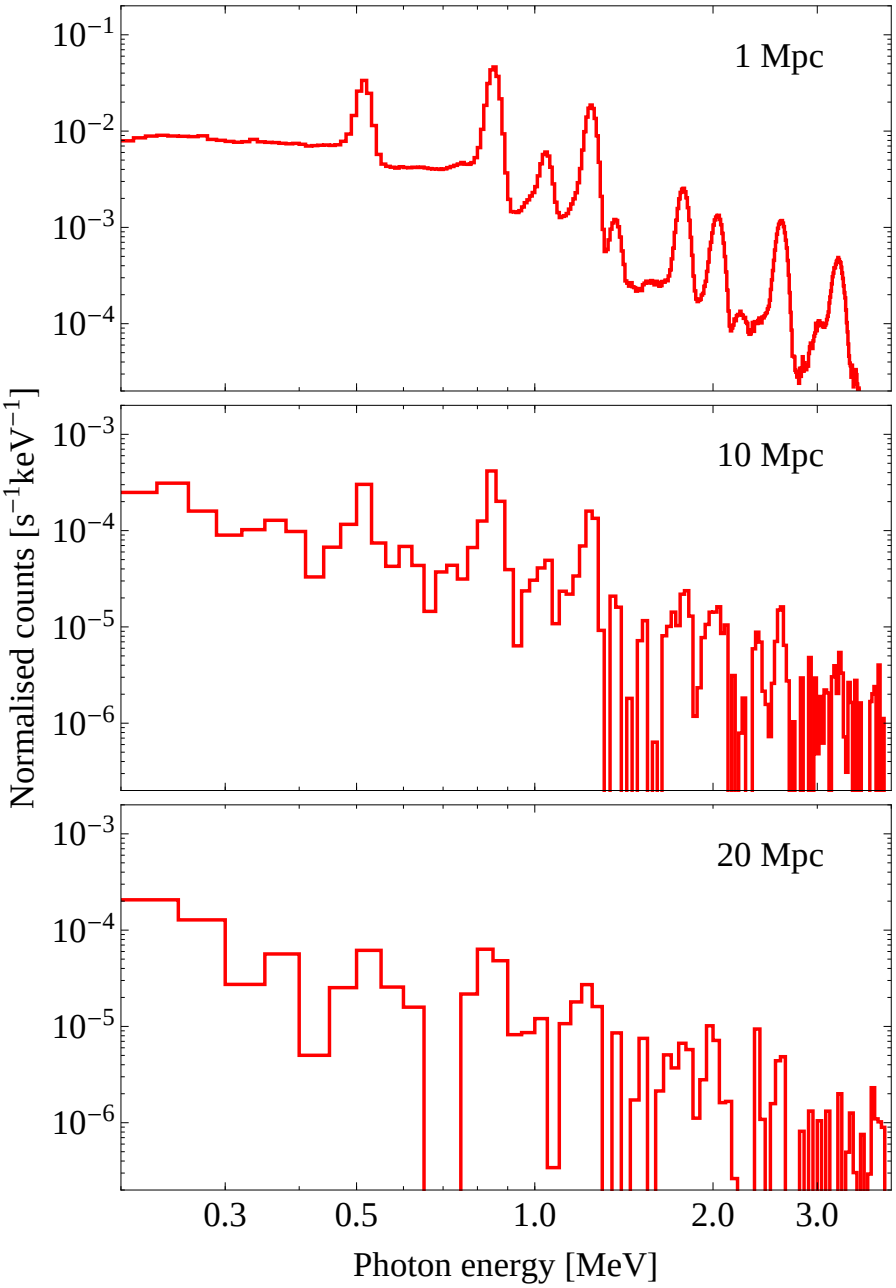

Figure 3.12: Simulated detector response for the GRM instrument aboard GRIPS for an exposure time of 10^6 s. For different distances to the source (indicated in the upper right), the simulated angle-averaged spectrum of the delayed-detonation model at 60 d after explosion is shown (taken from Summa et al. 2013).

resolved for sources at distances of 20 Mpc and more. The low-energy range of the measured spectra is dominated by background fluctuations at larger distances. Although the spectral resolution decreases with increasing source distances, line and hardness ratios still prove to be valuable diagnostic tools. According to the detector simulations for an exposure time of 10^6 s, the two explosion models can be distinguished up to SNe at 10 Mpc by the usage of H_1^*. With light curve measurements, this maximum distance for model distinctions can further be enlarged to ~ 16 Mpc. Therefore, a detection instrument like GRIPS will even allow for promising studies of the gamma-ray emission of SNe Ia in the Virgo cluster. It has to be noted that the success of such investigations is always limited by the accuracy of the applied background models. This results in a typical uncertainty of a factor of three (cf. Ajello et al. 2008) and especially the observations of more distant sources have to be discussed thoroughly with respect to these background effects. But even low-resolution spectra of distant explosion events lead to characteristic light curve shapes that allow for a discrimination of the two models. If the evolution of the gamma-ray emission can be followed over an extended period of time and if the flux maximum can be determined to a precision of about 5 d, bolometric measurements are sufficient.

Even though the chances of unambiguous conclusions on the explosion model decrease for SNe Ia at larger distances, the detection statistics of SNe Ia in the gamma-ray regime will be significantly extended with a future MeV gamma-ray telescope. Only one SN Ia has been detected in gamma rays up to now (Milne et al. 2004), but with sensitivities comparable to that of the proposed GRIPS mission, also SNe Ia at distances beyond 20 Mpc can be observed at MeV energies. As can be inferred from Figs. 3.9 and 3.12, the sensitivity of GRIPS below 300 keV is limited. This concerns especially the two lines of ^{56}Ni at 0.158 MeV and 0.270 MeV, which provide a distinct feature of the delayed-detonation model. But the disadvantage of the GRIPS mission can be compensated by using the data of the ASTRO-H mission (cf. Takahashi et al. 2010). This instrument, which is supposed to be launched in 2015, covers the respective energy range with sufficient sensitivity and reaches distance limits comparable to those of GRIPS (Maeda et al. 2012).

The analysis of the detector response simulations presented above shows that a detection of gamma-ray emission should easily be possible for the recently observed SN 2011fe at a distance of 6.4 Mpc. Although a certain explosion scenario can exhibit other variations besides viewing-angle effects (typical examples are additional rotation and mixing effects or modifications of details in the explosion mechanism), which can in turn lead to additional spreads of gamma-ray fluxes, the delayed-detonation and the violent merger model, which represent two different progenitor classes, leave unique imprints on the gamma-ray emission. If both models produce the same amount of ^{56}Ni, a higher total ejecta mass surrounding the radioactive material in the violent merger model is unavoidable. This leads to systematic effects that can clearly be seen in the gamma-ray observables as discussed in the previous paragraphs. With the study of the gamma-ray emission of SNe Ia, the degeneracy

different explosion models show concerning their optical observables (see e.g. Röpke et al. 2012 for the case of SN 2011fe) could certainly be removed. This again underlines the importance of a realisation of future missions like GRIPS and ASTRO-H with enhanced sensitivities in the MeV energy range (see also Chapter 2). Having been almost unexplored up to now, the emission at MeV energies provides a unique window towards a better understanding of progenitor scenarios of SNe Ia and can be used to reduce the parameter space of current three-dimensional model concepts.

4 X-ray diagnostics of Type Ia supernovae: The radioactive decay of ^{55}Fe

After a detailed investigation of the diagnostic value of the prompt gamma-ray emission from SNe Ia in Chapter 3, this chapter concentrates on the X-ray line emission that arises from the radioactive decay of ^{55}Fe a few years after explosion. As discussed in the following, this isotope is directly linked to intrinsic properties of SNe Ia models. This is why observations of this line allow for constraints on the underlying explosion scenario and provide a complementary tool in order to shed light on the progenitors of SNe Ia. The results presented in this chapter are based on Seitenzahl et al. 2014.

4.1 Overview

In addition to the gamma-ray emission in the MeV energy range, distinctive features of SNe Ia can also be found in the X-ray regime. In this chapter, it is shown that the abundance of ^{55}Fe is very sensitive to the prevailing conditions at the time of explosive nucleosynthesis and can directly be deduced from the measurement of a prominent X-ray line at 5.9 keV. This allows for conclusions on the temperature and density evolution during the nucleosynthesis processes and therefore on the underlying explosion scenario of SNe Ia. Similar to the previous chapter, the same two explosion models representing the single-degenerate and the double-degenerate channel are discussed: a delayed-detonation of a near-Chandrasekhar mass WD and a violent merger of two WDs with a sub-Chandrasekhar mass primary. After a detailed consideration of explosive nucleosynthesis and the production of ^{55}Fe in SNe Ia, the radiative transfer calculations for the X-ray emission of the three-dimensional explosion models are introduced. In order to determine the detectability of the X-ray line at 5.9 keV, different processes contributing to the continuum emission in this energy range have to be taken into account. The results of thorough detector simulations of current and future X-ray telescopes concerning the X-ray line emission of SNe Ia are presented in the last paragraph of this chapter and the most promising observing strategies for the detection of the 5.9 keV line and the possibilities for a distinction of different explosion models are examined.

4.2 Explosive nucleosynthesis in Type Ia supernova explosions

4.2.1 Fundamental processes

Nucleosynthesis processes can occur under different conditions and on different time scales. In general, two main regimes of nuclear burning are distinguished. In the first case, nucleosynthesis proceeds during the hydrostatic burning stages of stellar evolution on long time scales (see Section 1.4), whereas the second case is characterised by significantly shorter time scales and higher temperatures during explosive events. Even though many reactions are the same in both cases, the time scales of explosive processes are often shorter than many beta-decay half-lives of unstable nuclei. This is why the knowledge of the nuclear cross sections of these nuclei plays an important role for the calculation of nucleosynthesis processes in explosive environments. Depending on the temperature, intermediate mass nuclei up to heavy nuclei are produced in explosive burning. The burning regimes that are relevant for the thermonuclear explosion of a C/O WD and the composition of the explosion ejecta are briefly introduced in the following. Further details on explosive nucleosynthesis can be found in Arnett (1996) and Hirsch & Page (1998).

In addition to the different burning regimes, there are two equilibrium stages that are often discussed. For temperatures above $\sim 5 \times 10^9$ K, the so-called nuclear statistical equilibrium (NSE) is reached. All nuclear rates governed by strong and electromagnetic forces are in balance, only the weak interaction rates do not participate in the equilibrium. In this case, the abundance $Y_i = n_i/(\rho N_A)$ of each nucleus (n_i is the number density of nuclei per unit volume and N_A Avogadro's number) is only determined by the temperature T, the density ρ, the nuclear binding energy B_i, and the partition function (Hirsch & Page 1998)

$$G_i = \sum_j \left[\left(2J_j^i + 1 \right) \exp\left(-E_j^i / \left(kT \right) \right) \right]. \tag{4.1}$$

The abundance Y_i can be derived from the relation $\mu_i = Z_i\mu_p + N_i\mu_n$ for chemical potentials in a thermal equilibrium and results in (cf. Hirsch & Page 1998)

$$Y_i = \left(\rho N_A\right)^{A_i - 1} \frac{G_i}{2^{A_i}} A^{\frac{3}{2}} \left(\frac{2\pi\hbar^2}{m_u kT} \right)^{\frac{3}{2}(A_i - 1)} \exp\left(\frac{B_i}{kT} \right) Y_p^{Z_i} Y_n^{N_i} \tag{4.2}$$

where J^i, Z_i, and N_i denote spin, proton number, and neutron number of the nuclei i; A_i is the mass number and defined as $A_i = Z_i + N_i$. The subscripts n und p indicate neutrons and protons, respectively. Furthermore, mass conservation $\sum_i A_i Y_i = 1$ and charge neutrality $\sum_i Z_i Y_i = Y_e$ are assumed. Quasi-equilibrium (QSE) stages can exist if only clusters of neighbouring nuclei are in relative equilibrium via neutron and proton reactions, but the abundances in distinct clusters are different with respect to other regions of nuclei and thus to the values during NSE.

In mass zones with temperatures above $\sim 1.9 \times 10^9$ K, explosive C burning takes place and the main burning products are ^{20}Ne, ^{23}Na, and different isotopes of Mg. At temperatures of $\sim 2.1 \times 10^9$ K, Ne burning starts and ^{16}O, ^{28}Si, and ^{24}Mg are produced abundantly. Temperatures in excess of $\sim 3.3 \times 10^9$ K mark the onset of O burning and QSE stages for mass numbers between 28 and 45 are reached. Due to smaller energy releases and cross sections for reactions starting from closed shell nuclei with Z or $N = 20$, the path to heavier nuclei is still blocked and a full NSE with prominent abundances in the Fe-group cannot be achieved (see also Hirsch & Page 1998). The main products of O burning are ^{28}Si, ^{32}S, ^{34}S, ^{36}Ar, ^{38}Ar, and ^{40}Ca with traces of ^{56}Ni and ^{54}Fe. Within the QSE cluster, the abundances are determined by the fractions of alpha particles, protons, and neutrons (see also below). For temperatures in the range of $4.0 - 5.0 \times 10^9$ K, explosive Si burning starts. If the temperature exceeds $\sim 5.0 \times 10^9$ K, the available energies of the nuclei are sufficient to overcome all Coulomb barriers and NSE is attained. If the electron fraction Y_e is ~ 0.5, the doubly magic isotope ^{56}Ni with the largest binding energy per nucleon for $N = Z$ is predominantly synthesised besides smaller fractions of other Fe-group nuclei.

Depending on the prevailing temperatures and densities, different Si burning regimes (complete and incomplete Si burning) as well as freeze-out[1] conditions (normal and alpha-rich freeze-out) are distinguished. If temperatures and densities are high enough, complete Si burning and a normal freeze-out of the reactions after the explosive nucleosynthesis occur. The resulting abundances are in full NSE and can be completely described by Equation 4.2. If densities are too low, an alpha-rich freeze-out is caused. At falling temperatures, the triple-alpha reaction $^4\mathrm{He}(2\alpha,\gamma)^{12}\mathrm{C}$ and the reaction $^4\mathrm{He}(\alpha n,\gamma)^9\mathrm{Be}$ are not able to maintain NSE between light nuclei (n, p, ^{4}He) and intermediate mass nuclei beyond $A = 12$. Since the corresponding reaction rates show a quadratic dependence on the density, the fast expansion and cooling processes of explosive events lead to a large abundance of alpha particles after the freeze-out of charged particles. The abundances in clusters of QSE are shifted to heavier nuclei and instead of ^{56}Ni, ^{57}Ni or ^{58}Ni, the isotopes ^{60}Zn, ^{61}Zn, and ^{62}Zn are produced (Hix & Thielemann 1999). While the remaining fraction of alpha particles increases, the fraction of the dominant NSE nuclei is depleted. If temperatures are in the range of $4.0 - 5.0 \times 10^9$ K, they are too low to go beyond the proton magic number $Z = 20$ by nuclear reactions and Si burning is incomplete. In addition to unprocessed fuel nuclei like ^{28}Si and ^{32}S, the alpha-nuclei ^{36}Ar and ^{40}Ca are most abundant. Since the bottle neck due to the magic proton number can be partially circumvented, ^{56}Ni and ^{54}Fe are still the dominant species in the Fe-group. They are accompanied by smaller fractions of ^{52}Fe, ^{58}Ni, ^{55}Co, and ^{57}Ni.

In SN Ia explosions, typical temperatures between 10^9 K and 10^{10} K are reached.

[1]This term marks the time when temperatures become too low for an equilibrium between forward and backward reactions, NSE cannot be maintained any more and the abundance pattern "freezes out". The final abundances can be approximated by an NSE abundance at an appropriately chosen freeze-out temperature.

Since at densities above $\sim 10^8\,\mathrm{g\,cm^{-3}}$ and temperatures above $\sim 5.0 \times 10^9\,\mathrm{K}$ the state of NSE is attained (see above), nucleosynthetic yields are independent of the previous thermodynamic evolution. Detailed reaction rates only take effect again when the matter cools and the NSE state is left (Bravo & Martínez-Pinedo 2012). The type of the combustion front determines the temperatures that are relevant for the nuclear reactions. In case of a supersonic detonation, the fuel is shock-heated to temperatures $\gtrsim 2 \times 10^9\,\mathrm{K}$ before the nucleosynthesis processes start. The exact temperature value depends on the prevailing densities. In case of a subsonic deflagration, the combustion temperature within the flame can be set by two different mechanisms. For temperatures below a critical value of $\sim 2 - 5 \times 10^9\,\mathrm{K}$, heat diffusion from the hot ashes defines the temperature in the unburnt material. For temperatures above this value, the burning time scale is shorter than the diffusion time scale and the energy release by nuclear reactions is the dominant contribution (cf. Bravo & Martínez-Pinedo 2012).

The different explosive nucleosynthetic processes and the temperature and density conditions are shown in Fig. 4.1 for the example of a one-dimensional delayed-detonation model of a Chandrasekhar mass WD (Bravo & Martínez-Pinedo 2012). In this model, the central $0.4\,\mathrm{M_\odot}$ reach the conditions for NSE. While freeze-out is "normal" for the inner $0.16\,\mathrm{M_\odot}$, the outer $0.24\,\mathrm{M_\odot}$ in the central part fulfill the conditions for alpha-rich freeze-out. The temperatures and densities in the neighbouring $0.7\,\mathrm{M_\odot}$ allow for Si burning, and the conditions for QSE are reached in the Fe group. At larger distances from the centre of the WD, smaller amounts of material only undergo O and Ne burning. At the outer edges, temperatures and densities are too low for nuclear reactions beyond C burning. After the transition of the subsonic deflagration to a supersonic detonation, the fast propagation of the nuclear flame does not allow for a relaxation of the structure of the WD before most of the remaining fuel is burnt. This is reflected by the shorter distances between the star marks indicating mass shells of $0.1\,\mathrm{M_\odot}$ in Lagrangian mass coordinates between $4.0 \times 10^9\,\mathrm{K}$ and $5.5 \times 10^9\,\mathrm{K}$ (see Fig. 4.1).

4.2.2 Production mechanisms of ^{55}Fe

Most of the ^{55}Fe present in the ejecta of SNe Ia after explosive nucleosynthesis is not produced as "primary" ^{55}Fe, but as a decay product of ^{55}Co (e.g. Truran et al. 1967). ^{55}Co has a half-life of 17.5 h and for electron fractions $Y_e \lesssim 0.5$ it is mainly produced by two distinct processes: normal freeze-out from NSE and incomplete Si burning. Since a low mass fraction of alpha particles is required for such a normal freeze-out ($\lesssim 1\,\%$, cf. Woosley et al. 1973, and see also above), the preceding explosive nuclear burning has to proceed at relatively low entropy and therefore at high density ($\rho \gtrsim 3 \times 10^8\,\mathrm{g\,cm^{-3}}$, e.g. Thielemann et al. 1986; Bravo & Martínez-Pinedo 2012). This is the case for the delayed-detonation model already introduced in Subsection 3.3.1 where the densities are sufficiently high for a realisation of a normal freeze-out process.

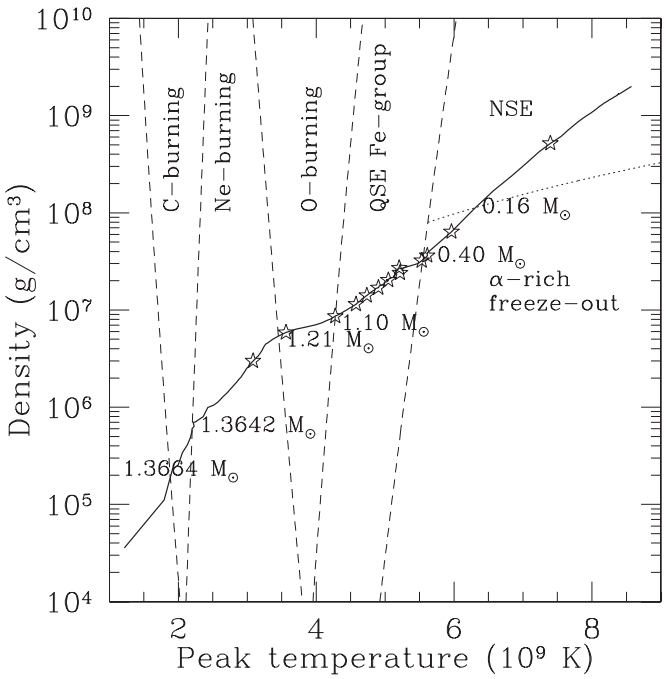

Figure 4.1: Peak temperatures and densities at each mass shell of the WD during the SN explosion as a function of the Lagrangian mass coordinate (solid line). The centre of the WD is located at the top right, the surface at the bottom left end. Star marks denote every mass shell of $0.1\,M_\odot$. The regions of different nucleosynthetic processes are approximately indicated by dashed and dotted lines. At the intersections of these lines with the solid line, the Lagrangian mass coordinate is additionally given (taken from Bravo & Martínez-Pinedo 2012).

In the violent merger model (see Subsection 3.3.1), the situation is different. Due to the lower mass of the primary WD and the resulting lower peak densities, ^{55}Co is mainly synthesised by incomplete Si burning. Nearly all of the ^{55}Co that is present in NSE at such low densities is destroyed by the reaction $^{55}\mathrm{Co(p,\gamma)}^{56}$Ni in the subsequent alpha-rich freeze-out (cf. Jordan et al. 2003). The different conditions during freeze-out are mirrored in the ^{55}Co yields of the two models. While $1.33 \times 10^{-2}\,M_\odot$ are produced in the delayed-detonation model, only $3.73 \times 10^{-3}\,M_\odot$ of ^{55}Co can be found in the ejecta of the violent merger model. According to Parikh et al. (2013), the production ratio of ^{55}Co to ^{56}Ni is rather insensitive to uncertainties in the nuclear reaction rates. This is why the prediction of distinct ^{55}Co yields for the two explosion models is very robust. At equal masses of ^{56}Ni, the abundance of ^{55}Co is significantly higher in the delayed-detonation model. This pronounced difference between the two models also influences the predicted behaviour of late time bolometric light curves of SNe Ia (Seitenzahl et al. 2009b, 2011; Röpke et al. 2012). Since ^{55}Fe decays to the stable isotope ^{55}Mn that is predominantly synthesised in SNe Ia, the solar abundance of ^{55}Mn can also be used to draw conclusions

on the relative fractions of near-Chandrasekhar mass and sub-Chandrasekhar mass progenitor channels in the Galaxy (see Seitenzahl et al. 2013a).

4.3 Radiative transfer simulations

In this chapter, the focus is on the X-ray line emission that is related to the radioactive decay of ^{55}Fe. This isotope decays by electron capture to ^{55}Mn with a half-life of 2.7 yr. When the daughter nuclei ^{55}Mn relaxes to eliminate K-shell vacancies, the difference in energy is dominantly released by the emission of Auger electrons with a probability of $\sim 60\,\%$. Additionally, a doublet of K_α lines with energies of 5.888 keV (8.2 %) and 5.899 keV (16.2 %) is produced (Browne & Firestone 1986). The idea of using the X-ray emission processes connected to electron capture radioactivity as a diagnostic of SN nucleosynthesis was already introduced by Leising (2001). In the case of SN 1987A, a search for the ^{55}Mn K_α line in 400 ks of Chandra/ACIS data only resulted in upper limits (Leising 2006). By the application of one-dimensional models it could be shown that the amount of produced ^{55}Co is significantly higher for SNe Ia than for core-collapse events (Leising 2001). In the following, the production of ^{55}Fe is studied for the first time with a fully three-dimensional treatment of the explosion hydrodynamics. This allows for a realistic description of the distribution of the radioactive isotopes in the ejecta and enables radiative transfer calculations taking into account different lines of sight to the explosion event.

In order to determine the respective line fluxes, the results of the two hydrodynamical simulations already introduced in Chapter 3 are used. The two explosion models – a delayed-detonation of near-Chandrasekhar mass WD and a violent merger of two WDs with a sub-Chandrasekhar mass primary – are chosen as illustrative examples that underline the dependence of the ^{55}Fe yield on the different freeze-out processes and therefore on the explosion scenario and primary WD mass. The photon flux (photons $\mathrm{cm}^{-2}\,\mathrm{s}^{-1}$) of the 5.9 keV Mn K_α line[2] at time t relative to the explosion is

$$F(t,\mathbf{n}) = \frac{p_\gamma \ln 2}{4\pi D^2 m_{55} t_{1/2}} \exp\left(-\frac{t \ln 2}{t_{1/2}}\right) \times \int_V \rho(\mathbf{r},t)\, X^0_{55}(\mathbf{r},t)\, e^{-\tau(\mathbf{r},t,\mathbf{n})}\, \mathrm{d}V. \tag{4.3}$$

The observer orientation is specified by the unit vector $\mathbf{n}$, D is the distance of the SN, and the integral runs over the entire volume of the ejecta. The half-life of ^{55}Fe is denoted by $t_{1/2} = 2.7\,\mathrm{yr}$, the probability per ^{55}Fe decay of producing a 5.9 keV Mn K_α photon is assumed to be $p_\gamma = 0.244$ (Browne & Firestone 1986). The mass density of the ejecta at position $\mathbf{r}$ is given by ρ, m_{55} is the atomic mass of ^{55}Co and

[2]Due to the fact that the energy difference between the two lines at 5.888 keV and 5.899 keV cannot be resolved by current and planned X-ray telescopes, the line doublet is considered one X-ray line at 5.9 keV hereinafter.

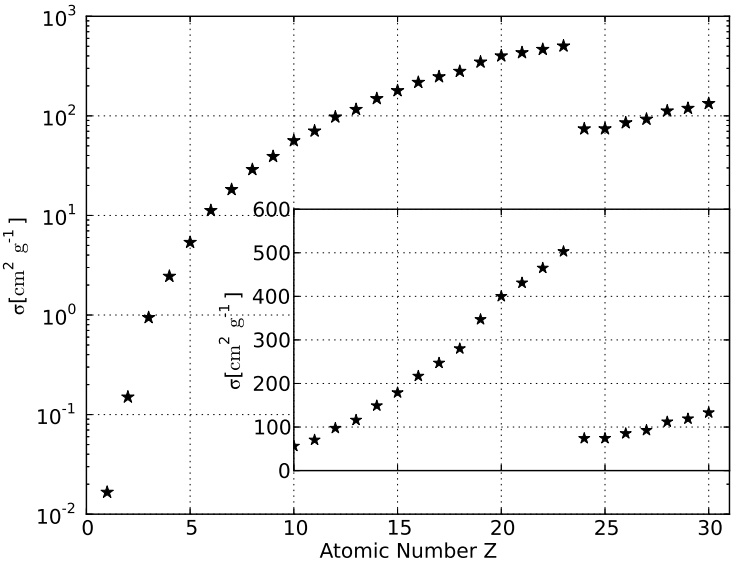

Figure 4.2: Photo-absorption cross sections for the elements H to Zn at photon energies of 5.9 keV as a function of atomic number Z. The data are taken from Henke et al. (1993). The inset shows the cross sections on a linear scale for $Z \geq 10$. Since incoherent scatterings only contribute significantly for H that is not found abundantly in the ejecta of SNe Ia, these processes are neglected (taken from Seitenzahl et al. 2014).

X_{55}^0 is the sum of the mass fractions of ^{55}Co and ^{55}Fe at $t = 0$, i.e. immediately after the explosion. Since the half-life of ^{55}Co is orders of magnitude shorter than that of ^{55}Fe (see above), the decay of ^{55}Co to ^{55}Fe is treated as effectively instantaneous. The optical depth for the X-ray line photons is given by

$$\tau(\mathbf{r}, t, \mathbf{n}) = \sum_{Z=1}^{30} \sigma_Z \int_{\mathbf{r}}^{\infty} \rho(\mathbf{r}', t)\, X_Z(\mathbf{r}', t)\, \mathrm{d}s, \tag{4.4}$$

where X_Z is the mass fraction of the element with atomic number Z. For the photo-absorption cross section σ_Z (cm^2 g^{-1}) at 5.9 keV the results from Henke et al. (1993) are used (see also Fig. 4.2). The integral runs from the starting point $\mathbf{r}$ to the outer edge of the ejecta along the ray defined by $\mathrm{d}\mathbf{r}' = \mathbf{r} + \mathbf{n}\,\mathrm{d}s$. Since electron scattering is relatively unimportant at several years after explosion, it is assumed that photo-absorption is the dominant contribution to the opacity (see also below). To evaluate Equations 4.3 and 4.4, the respective properties are extracted from the hydrodynamical explosion models. With the use of the ensemble of nucleosynthesis tracer particles at the final state of the explosion simulations at $t = 100$ s, the distributions of density and composition are reconstructed on uniform Cartesian grids by a smoothed-particle-hydrodynamics-like algorithm (cf. Kromer et al. 2010). For the further evolution of the ejecta, a homologous expansion law is adopted.

The results of the radiative transport calculations for the two different explosion

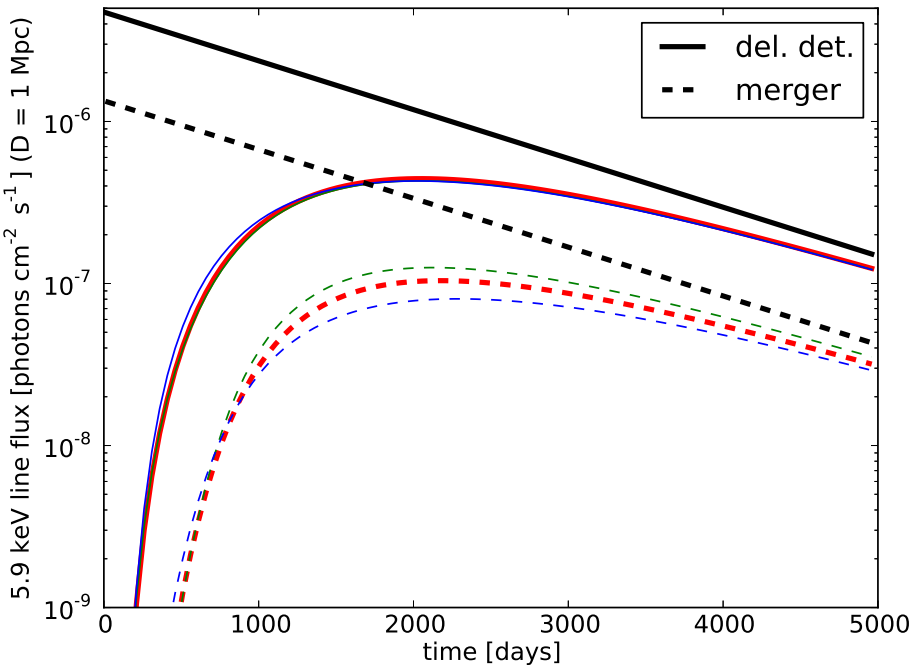

Figure 4.3: X-ray line flux at 5.9 keV for the delayed-detonation (solid lines) and the violent merger model (dashed lines). The line flux is normalised to a distance of 1 Mpc. Three orthogonal lines of sight are indicated with different colours in each case. The black lines denote the optically thin limit where no absorption effects have been taken into account (taken from Seitenzahl et al. 2014).

scenarios can be inferred from Fig. 4.3. Compared to the violent merger model, the flux of the 5.9 keV line in the delayed-detonation model is significantly enhanced due to the larger amount of synthesised ^{55}Co. Both models show a similar evolution of the X-ray line flux. Since the photoelectric opacity of the ejecta is quite large at early times and the half-life of ^{55}Fe is relatively long, the maximum fluxes are reached at $\sim$ 2100 d. Therefore, the optimal time frame for X-ray observations of the 5.9 keV emission line is between five and six years after the explosion. The comparison of the results to the optically thin limit (see Fig. 4.3) indicates that attenuation effects play an important role until roughly 5000 d, and also mirrors the time evolution of the photoelectric opacity.

In Fig. 4.3, the colour-coded set of curves for each model refers to three orthogonal lines of sight to the SN. While being negligible for the delayed-detonation model, different viewing angles have a moderate effect on the line fluxes of the violent merger model. Due to the asymmetric ejecta structure and the inhomogeneous distribution of the radioactive isotopes, the spread between the flux values for different lines of sight is larger. In contrast to their gamma-ray emission (see Section 3.4 and Summa et al. 2013), the two models do not exhibit a degeneracy concerning the flux of the 5.9 keV X-ray emission line.

4.4 Observability of the 5.9 keV line

In order to assess the diagnostic value of the 5.9 keV emission line in light of current and future X-ray observatories, thorough detector simulations are performed and the results regarding the necessary exposure times and the possibilities for a distinction of the two explosion scenarios are discussed in the following. Besides the expected signal from the 5.9 keV X-ray line, the respective instrumental backgrounds and X-ray continuum contributions have to be taken into account.

4.4.1 X-ray continuum emission at keV energies

Concerning the X-ray continuum emission of SNe, there are two major sources: fast electrons in the SN interior that produce bremsstrahlung emission and the interaction of the ejecta with the surrounding CSM resulting in thermal and non-thermal emission processes.

The bremsstrahlung contribution of fast electrons in SN explosions is intensively discussed by Clayton & The (1991). Originating from Compton-scattering events with the primary gamma-ray photons of the radioactive isotopes in the ejecta, the recoil electrons scatter from ions during their deceleration to thermal energies within the SN interior and produce bremsstrahlung photons. The X-ray luminosity due to this mechanism dominates that of down-scattered primary gamma-ray photons for energies below 20 keV and is most intense in the first few weeks after the explosion (see Clayton & The 1991). At these times, the energy deposition due to the decay of the radioactive isotopes ^{56}Ni and ^{56}Co is still large. Additionally, the production of fast electrons in the outer edges of the ejecta that dominate the emission around 5.9 keV is more efficient than at later times when the ejecta become more and more dilute and the Compton optical depth decreases. An extrapolation of the results of Clayton & The (1991) to the epochs of interest concerning the detection of the 5.9 keV X-ray line ($\sim$ 2100 d after the explosion) shows that the internal bremsstrahlung contribution is completely negligible. This conclusion is further supported by the results of a study by Immler et al. (2006).

A second possible contribution to the continuum emission at keV energies arises from the interaction processes of the ejecta with the surrounding CSM. There thermal and non-thermal emission processes can occur. But the non-thermal emission of particles that are accelerated at SN shocks is usually supposed to be very small at a few years after the explosion. According to simulations of the time evolution of non-thermal particle distributions in SNRs, it can be shown that the resulting emission of these particles strongly rises after a few hundred years and reaches its maximum after several thousand years (Sturner et al. 1997; Caprioli 2012). This is why X-ray spectra of young SNRs are normally dominated by thermal emission processes at the epochs of interest for the detection of the 5.9 keV line (see also Badenes 2010), and only this thermal emission component is taken into consideration in the subsequent

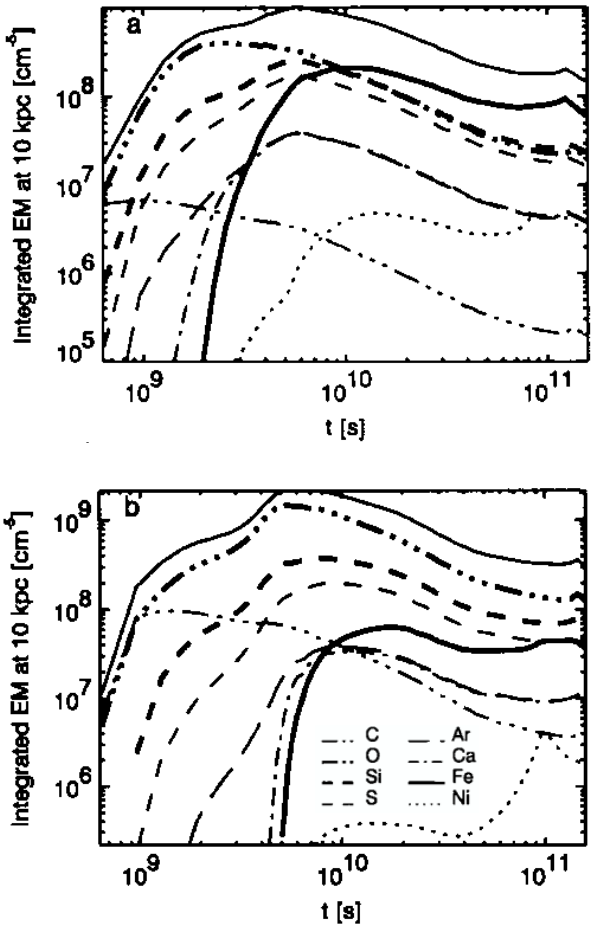

Figure 4.4: Temporal evolution of the emission measure for the ejecta structure of two one-dimensional delayed-detonation models. The values are normalised for a distance of 10 kpc to the SN. While the different line styles indicate the contributions from different chemical elements, the total emission measure is given by the upper thin solid line (adapted from Badenes et al. 2003).

discussion. The intensity of the thermal X-ray emission from the interaction of the ejecta with the CSM depends on the strengths of forward and reverse shocks that build up when the SN material is driven into the ambient medium. As more and more heated and compressed material is accumulated, the X-ray radiation in the shocked regions increases. Following hydrodynamical simulations that assume typical densities for the CSM, the X-ray luminosity is maximal at several hundred years after the explosion (Badenes et al. 2003). This is confirmed by observations that only set upper limits for the thermal X-ray emission of SNe Ia at early times (e.g. Hughes et al. 2007).

In order to take into account the effects of CSM interaction concerning the detectability of the 5.9 keV line, an analytic model of the X-ray continuum emission

of the form

$$\mathrm{d}F(\nu, T) = \text{const.} \times (kT)^{-\frac{1}{2}} \exp\left(\frac{h\nu}{kT}\right) \mathrm{d}\nu \int\limits_{V_{\mathrm{sh}}} n_e n_i \, \mathrm{d}V \tag{4.5}$$

is adopted (e.g. Padmanabhan 2000, but see also Immler et al. 2006; Hughes et al. 2007). The normalisation of the bremsstrahlung flux is defined by the so-called emission measure

$$\mathrm{EM} = \int\limits_{V_{\mathrm{sh}}} n_e n_i \, \mathrm{d}V \tag{4.6}$$

with the volume of the shocked and emitting material V_{sh}, the electron density n_e, and the ion density n_i. Furthermore, a value of $kT = 10\,\mathrm{keV}$ (Fransson et al. 1996; Immler et al. 2006) and an ambient medium with a constant density of $\rho_{\mathrm{AM}} = 10^{-24}\,\mathrm{g\,cm^{-3}}$ are assumed. For such a density that is typical in most regions of the Galaxy and the Magellanic Clouds, hydrodynamical simulations of SN shock interactions result in emission measures of roughly $10^{51}\,\mathrm{cm^{-3}}$ to $10^{52}\,\mathrm{cm^{-3}}$ at six years after the explosion (see Fig. 4.4 and Badenes et al. 2003). Only a rare subclass of SNe Ia shows indications of a strong CSM interaction at early times. In these cases, the CSM the SN shock front is driven into may previously have been enriched by ejected material of the progenitor system (Russell & Immler 2012; Silverman et al. 2013). This additionally justifies the preceding assumptions concerning the ambient medium as well as the emission measure. In the following, an emission measure of $10^{51}\,\mathrm{cm^{-3}}$ is used. The emission line and the thermal bremsstrahlung fluxes are corrected for a Galactic neutral hydrogen column density (cf. Wilms et al. 2000) in the direction of M101. The value of $N_H = 1.8 \times 10^{20}\,\mathrm{cm^{-2}}$ (Kalberla et al. 2005) is typical of an observation that does not point towards the Galactic disk. However, the results do not rely on the exact value of N_H since absorption effects at photon energies of 5.9 keV can be neglected for column densities below $\sim 10^{22}\,\mathrm{cm^{-2}}$.

4.4.2 Detector simulations

In general, the detection significance S/σ_s is defined as

$$\frac{S}{\sigma_s} = r_s \frac{\sqrt{\delta t}}{\sqrt{r_s + 2r_b}} \tag{4.7}$$

where r_s is the source count rate, r_b the background count rate, which includes both instrumental background and continuum count rates, and δt the exposure time (Bradt 2004). The detector simulations are performed for several current and future X-ray telescopes: Chandra/ACIS, eROSITA, XMM-Newton/pn, NuSTAR, and Astro-H/SXS. The respective effective areas, redistribution matrix functions, and background count rates are inferred from Chandra X-ray Center (2012); Boller (2011); Read & Ponman (2003); Harrison et al. (2010) and Astro-H Mission (2013).

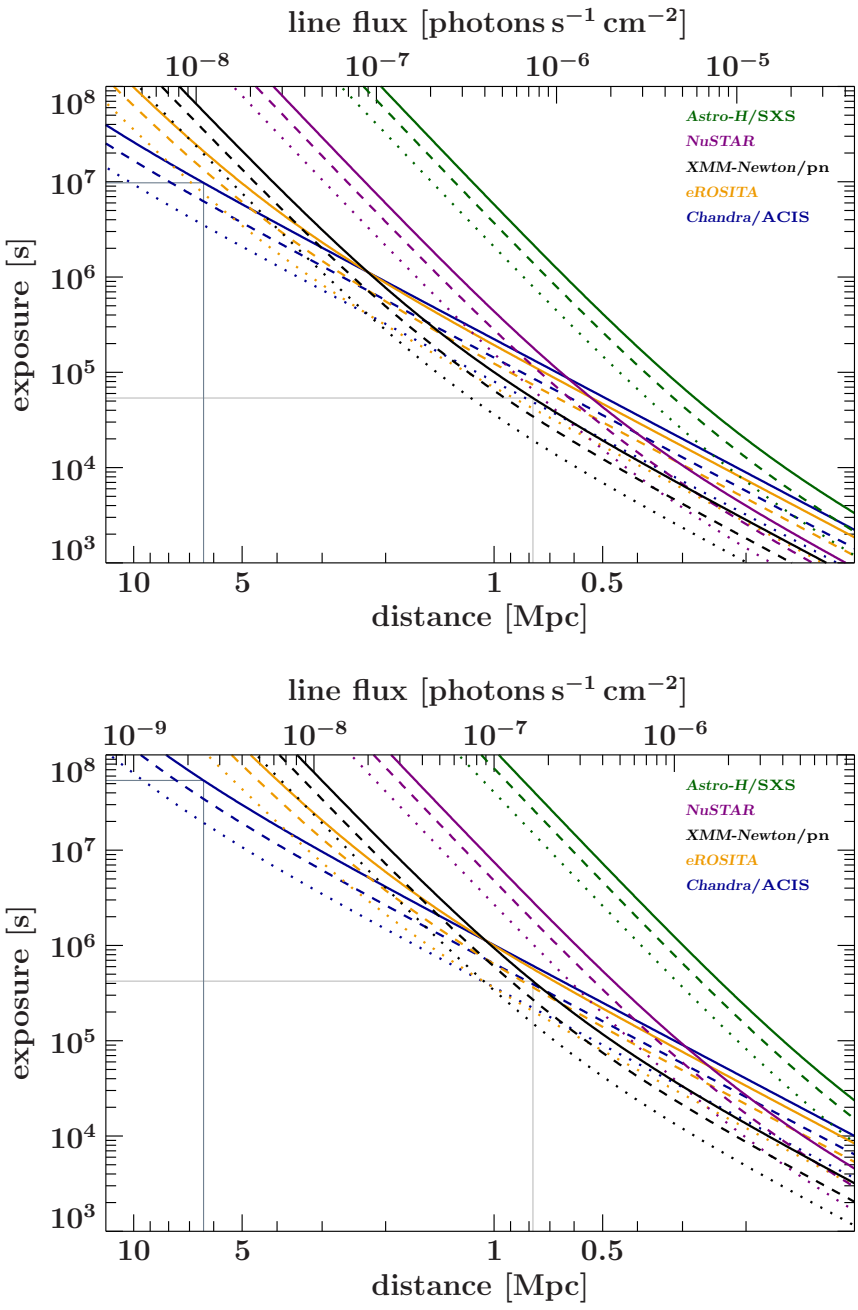

Figure 4.5: Required exposure times as a function of photon flux (indicated on the upper X-axis) for the detection of the 5.9 keV line with different X-ray instruments in case of the delayed-detonation model (upper panel) and the violent merger model (lower panel). The line style (dotted, dashed, solid) encodes the significance of the detection (3σ, 4σ, 5σ). The distances to the SN denoted on the lower X-axis refer to the maximum X-ray line flux that both models reach at roughly 2100 d after the explosion. The thin vertical lines mark the necessary exposure times for the distance to SN 2011fe (6.4 Mpc) and for the distance to M31 (0.78 Mpc). They are given for a detection with a significance of 5σ with respect to the most sensitive instrument in each case (adapted from Seitenzahl et al. 2014).

In Fig. 4.5, the simulation results are shown. For each of these five instruments, the required exposure times for a line detection with 5σ, 4σ, and 3σ significance are given in dependence on the distance to the SN and for each of the two explosion models discussed above. The determination of the distance is based on the assumption that the X-ray line is observed at the maximum flux value of the models at roughly 2100 d after the explosion. Due to the fact that the predicted line flux of the violent merger model is lower than that of the delayed-detonation model by a factor of 4.5, the distances corresponding to a detection of the X-ray line with the same significance as for the delayed-detonation model are accordingly shifted by a factor of $1/\sqrt{4.5}$. Therefore, in order to reach the same significance for a detection of the X-ray line as in the delayed-detonation model, longer exposure times are needed in case of the violent merger model.

The different slopes of the curves in Fig. 4.5 at low and high line fluxes indicate two different regimes for the line detection. If the explosion event is further away, the line fluxes are low and the background count rates of the detector dominate the source flux (background dominated regime). Since the instrumental background is very low for Chandra/ACIS, this detector is the best choice to detect the line for SNe at distances above 2 Mpc. For explosion events in the local Universe with source fluxes $\gtrsim 10^{-7}\,\mathrm{photons\,s^{-1}\,cm^{-2}}$, the count rates are not background dominated any more and the sensitivity of a detector is determined by the size of its effective area (source dominated regime). In this case, XMM-Newton is the best-suited instrument and for a SN at a distance comparable to that of M31 (see Fig. 4.5), exposure times of several 100 ks are sufficient to detect the 5.9 keV line at adequate significance.

Besides the study of the different flux contributions at 5.9 keV described above, the line detection is simulated in greater detail for the XMM-Newton/pn instrument, too. In order to fully resolve the line, Doppler broadening is taken into consideration and a typical velocity of $v = 3000\,\mathrm{km\,s^{-1}}$ is assumed for the line width. As before, the line fluxes are set to the maximum value for both explosion models. An example of such a resolved line detection can be seen in Fig. 4.6 where the results for the delayed-detonation model are depicted. According to these detailed simulations, the line fluxes can be determined with uncertainties less than 15 % for sufficient exposure times and a distinction of the two models is possible for distances of less than 1 Mpc. A detection of the 5.9 keV line is still feasible for more distant SNe (see Fig. 4.5), although a model distinction is much more challenging then. For SNe at a distance of 6.4 Mpc like the recently discovered SN 2011fe, a line detection at 5σ significance level would require an exposure time of $\sim 10^7$ s in case of the most sensitive instrument for such an observation, the Chandra/ACIS detector. Therefore SNe at these distances are marginally out of reach for current and near-future X-ray telescopes, but further developments in the section of X-ray detectors and especially proposed large-scale missions such as Athena+ (Nandra et al. 2013) should also make these SNe accessible for further investigations.

It has to be noted that variations of the parameters EM, kT, and v do not affect the results of the simulations presented above in a substantial way. Since the fluxes

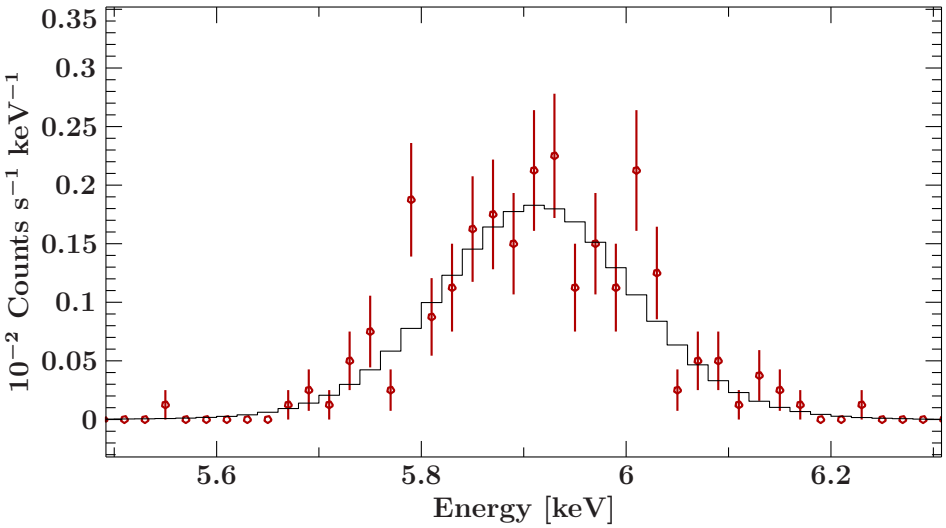

Figure 4.6: Detailed simulation of a background-subtracted spectrum for the XMM-Newton/pn instrument (exposure time 500 ks). For the flux of the 5.9 keV line, a SN explosion according to the delayed-detonation scenario at a distance of 0.78 Mpc is assumed. The red symbols show the simulated data, the best-fit result with a Gaussian emission line is indicated in black. The continuum count rate resulting from an emission measure of $10^{51}\,\mathrm{cm}^{-3}$ is considerably below the instrumental background (adapted from Seitenzahl et al. 2014).

due to thermal continuum emission are significantly lower than the line flux at 5.9 keV from the decay of ^{55}Fe, even larger changes of the values for EM and kT only have minor consequences regarding the line detectability, and the predictions concerning the necessary exposure times (see Fig. 4.5) remain quite robust. Even if the contribution of non-thermal emission resulting from efficiently accelerated CR particles should be of the same order of magnitude as the thermal emission model, the line detectability would remain qualitatively unaffected. Similarly, due to the dominant X-ray line flux, additional contributions to the X-ray background around 5.9 keV can be regarded as negligible in most situations. In case of higher ejecta velocities, a larger Doppler broadening only leads to slightly more extended error bars for the determination of the line flux. This is why the 5.9 keV emission line provides a unique distinctive feature that is independent of the choice of a specific parameter set of the explosion models.

Due to the fact that even very different explosion scenarios can exhibit huge degeneracies in their observables, it is important to find clear and robust signatures that unambiguously point towards differences in the suggested explosion models. In case of the two leading explosion scenarios of SNe Ia, a near-Chandrasekhar mass delayed detonation and a violent merger of two WDs, the different central densities at the time of freeze-out are characteristic properties. As a consequence, ^{55}Co is produced more abundantly in the delayed-detonation model and there the flux of

the 5.9 keV X-ray line is 4.5 times larger than in the violent merger model. The estimates concerning the line detectability shown in Fig. 4.5 can therefore be used as a reference for future SN Ia X-ray observations. In view of the scarcity of SNe Ia in the local Universe and the sensitivities of current X-ray instruments, X-ray fluxes alone are not suitable for constraining the relative rates of SNe Ia originating from different progenitor models (cf. Ruiter et al. 2011). But in case of individual events at distances up to ~ 2 Mpc, X-ray observations with a focus on the 5.9 keV emission line are very promising. In order to disentangle the two explosion models, an exposure time of less than 500 ks would be sufficient for a SN Ia in the local group (M31). For the delayed-detonation model, a line detection at a significance level of 5σ would even be possible for exposure times $\gtrsim 50$ ks. Therefore, the 5.9 keV signature can be used to address the open questions concerning SN Ia explosion and progenitor scenarios, and it represents an independent and viable diagnostic tool that should be taken into account in future X-ray observations.

5 Nucleosynthesis calculations in Type Ia supernova explosion models

In this chapter, the application of nuclear network calculations for the determination of the nucleosynthetic yields in SNe Ia simulations is further discussed. The main focus of the following sections concentrates on the effects of an update of the used reaction rate libraries with respect to the isotopic abundances in the ejecta of SNe Ia, and the implementation of an extended nuclear reaction network in the Leafs code.

5.1 Overview

The distinction of different SNe Ia explosion models crucially relies on robust predictions of the isotopic yields of explosive nucleosynthesis. In view of the large degeneracies that are even present in the observables of very different explosion scenarios (see Chapter 3), distinctive observable features often depend on less abundant isotopes (see the example of ^{55}Fe in Chapter 4) or small differences in the isotopic yields. Therefore, accurate calculations of explosive nucleosynthesis in SN Ia simulations are necessary. Besides a detailed treatment of the combustion physics and the microscopic properties of nuclear burning fronts in the hydrodynamical code, the uncertainties of the nuclear network calculations themselves have to be minimised for that purpose. Since large reaction networks are required for a precise determination of the isotopic yields, a full treatment of all nuclear reactions during the hydrodynamical simulation is computationally very expensive. This is why the detailed isotopic abundances are normally calculated in a post-processing step and only an approximate determination of the nuclear energy release is implemented in the hydrodynamical simulation (see below). After the inclusion of the newest available reaction rate libraries in the post-processing network, previous calculations and calculations using the actual data are compared in the following. Additionally, a medium-sized nuclear network is constructed that is large enough to contain all isotopes that are relevant to radiative transfer calculations (see Subsection 3.3.2), but still allows for applications within the hydrodynamical code. This enables a comparison of the post-processing method with in-situ nuclear network calculations during the hydrodynamical evolution of the SN explosion, and with an increase of

the available computing power, even a full treatment of a large reaction network within the LEAFS code may become possible in the future.

5.2 Treatment of nuclear reactions in simulations of Type Ia supernovae

Most parts of the explosion models discussed in this thesis are simulated with the LEAFS code. This hydrodynamical code has been developed at the Max Planck Institute for Astrophysics and is described in the publications by Reinecke et al. (1999); Röpke & Hillebrandt (2005); Schmidt et al. (2006); Röpke & Niemeyer (2007) and Röpke & Niemeyer (2007). A short overview of the physical foundations and of the basic numerical concepts is given in the following.

5.2.1 Reactive Euler equations and thermonuclear rate equations

Since WD matter can be modelled as a fully ionised plasma with arbitrarily degenerate and arbitrarily relativistic electrons, the continuum assumption[1] is fulfilled and the hydrodynamical Euler equations can be applied (Hillebrandt & Niemeyer 2000). The properties of an ordinary fluid are described by balance equations for mass, momentum, and energy (e.g. Landau & Lifshitz 1959):

$$\partial_t \rho + \nabla(\rho \mathbf{u}) = 0, \tag{5.1}$$

$$\partial_t(\rho \mathbf{u}) + \nabla(\rho \mathbf{u} \otimes \mathbf{u}) = -\nabla p + \rho \mathbf{f}, \tag{5.2}$$

$$\partial_t(\rho e_{\mathrm{tot}}) + \nabla(\rho e_{\mathrm{tot}} \mathbf{u}) = -\nabla(p\mathbf{u}) + \rho \mathbf{u} \cdot \mathbf{f} + \rho s(\mathbf{r}) \tag{5.3}$$

with the mass density ρ and the fluid velocity $\mathbf{u}$. External forces are indicated with $\mathbf{f}$ and can be derived from $\mathbf{f} = \nabla\Phi$ in case of the gravitational potential Φ. Thermonuclear reactions are accounted for by an additional source term $s(\mathbf{r})$ in the energy balance equation. An additional balance equation is introduced for the description of the changes in the chemical composition due to combustion processes:

$$\partial_t(\rho X_j) + \nabla(\rho \mathbf{u} X_j) = r_j(\rho, T, \mathbf{X}), \quad j = 1, ..., N \tag{5.4}$$

where $\mathbf{X}$ ($X_j = \rho_j/\rho$) denotes the mass fractions of N chemical species and r_j is the reaction rate for species j. It has to be noted that $\mathbf{X}$ and $\mathbf{r}$ are defined in the

[1] For the continuum assumption to be valid, the mean free path of the individual particles has to be much smaller than the length scale that is characteristic of the changes of important properties of the considered system. In this picture, the medium consists of fluid elements that contain certain amounts of matter in local thermal equilibrium and these fluid elements can be described with a basic set of thermodynamical quantities.

N-dimensional space of the chemical species. Since the sum of the N equations represented by Equation 5.4 is equivalent to mass conservation that is already given by Equation 5.1, the system of equations is overdetermined. Therefore, one of the species equations is usually dropped. For a closed set of equations, an equation of state for the WD matter has to be added. This equation defines the relation of pressure to density, internal energy, and composition:

$$p = f_{\mathrm{EOS}}(\rho, e_{\mathrm{int}}, \mathbf{X}). \tag{5.5}$$

The evolution of detailed nucleosynthetic abundances during the SN explosion is calculated by the application of nuclear reaction networks (see also Hix & Meyer 2006). For a reaction between a target particle j and a projectile particle k, the cross section is given by

$$\sigma = \frac{\text{number of reactions per target and s}}{\text{flux of incoming projectiles}} = \frac{r/n_j}{n_k v} \tag{5.6}$$

where n_j and n_k denote the number densities of target and projectile particles with a relative velocity v that is assumed to be constant. In general, targets and projectiles have distributions of velocities and the number of reactions r (in $\mathrm{cm}^{-3}\,\mathrm{s}^{-1}$) is defined as

$$r_{i,k} = \int \sigma\left(|\mathbf{v}_j - \mathbf{v}_k|\right) |\mathbf{v}_j - \mathbf{v}_k| \,\mathrm{d}^3 n_j \,\mathrm{d}^3 n_k. \tag{5.7}$$

For astrophysical plasmas, Maxwell-Boltzmann statistics is usually applicable and the relation

$$\mathrm{d}^3 n = n \left(\frac{m}{2\pi k_B T}\right)^{\frac{3}{2}} \exp\left(-\frac{m v^2}{2 k_B T}\right) \mathrm{d}^3 v \tag{5.8}$$

holds (Hix & Meyer 2006). With this relation, Equation 5.7 can be expressed as

$$r_{j,k} = \langle \sigma v \rangle_{j,k} \, n_j n_k. \tag{5.9}$$

With the reduced mass μ of the target-projectile system, the centre-of-mass energy E, the temperature T, and the Boltzmann constant k_B, the velocity integrated cross sections $\langle \sigma v \rangle$ of thermonuclear reactions are defined as (Clayton 1983)

$$\langle j, k \rangle \equiv \langle \sigma v \rangle_{j,k} = \left(\frac{8}{\mu \pi}\right)^{\frac{1}{2}} (k_B T)^{-\frac{3}{2}} \int_0^\infty E \sigma(E) \exp\left(-\frac{E}{k_B T}\right) \mathrm{d}E. \tag{5.10}$$

For nuclear reactions in astrophysical plasmas, background effects due to other nuclei and electrons have to be considered in addition. While experimental and theoretical reaction rates are determined for bare nuclei, the background of other particles leads to a modified Coulomb repulsion experienced by the reacting nuclei. These so-called "screening effects" are especially important for high densities and/or low temperatures. For non-vanishing temperatures, the modification of the Coulomb

repulsion can usually be accounted for by the introduction of a separate screening factor in Equation 5.10 (Brown & Sawyer 1997):

$$\langle j,k\rangle^* = f_{\mathrm{scr}}(Z_j, Z_k, \rho, T, n_i)\,\langle j,k\rangle\,. \tag{5.11}$$

The screening factor depends on the charge of the reacting particles, the density, the temperature, and the composition of the astrophysical plasma.

Based on the number of involved nuclei, nuclear reactions can be subdivided into three groups. The first group consists of all reactions where only one nucleus takes part, i.e. decays, electron and positron captures, photodisintegrations, and reactions induced by neutrinos. In these cases, the reaction rates only depend on the number densities of the target species. The second group is made up of reactions of two nuclei and the reaction rates are determined by both the number densities of target and projectile nuclei. Three-particle processes such as the triple-α process form the third group. Although an unstable intermediate target is usually involved in these reactions (e.g. Nomoto et al. 1985), the assumption of an equilibrium abundance of the unstable intermediate allows for a treatment of these reactions as three-particle processes. For each nuclear species, the relation of the temporal change of the respective number density to the reaction rates can be expressed as (Hix & Meyer 2006)

$$\left.\frac{\partial n_i}{\partial t}\right|_{\rho=\mathrm{const.}} = \sum_j \mathcal{N}_j^i r_j + \sum_{j,k} \mathcal{N}_{j,k}^i r_{j,k} + \sum_{j,k,l} \mathcal{N}_{j,k,l}^i r_{j,k,l}. \tag{5.12}$$

The three sums represent the three different groups of reactions. The factors $\mathcal{N}$ are introduced for a proper counting of numbers of nuclei and are defined by

$$\mathcal{N}_j^i = N_i, \quad \mathcal{N}_{j,k}^i = \frac{N_i}{\prod_{m=1}^{n_{j,k}} |N_m|!}, \quad \mathcal{N}_{j,k,l}^i = \frac{N_i}{\prod_{m=1}^{n_{j,k,l}} |N_m|!}. \tag{5.13}$$

Depending on how many particles of species i are destroyed or created during a reaction, the numbers N_i can be negative or positive. In order to distinguish between changes of number densities due to nuclear reactions and hydrodynamical changes of number densities due to an expansion or a contraction of the astrophysical plasma, the nuclear abundance

$$Y_i = \frac{n_i}{\rho N_A} \tag{5.14}$$

is commonly used, N_A denotes Avogadro's number. The quantity $A_i Y_i$ expresses the mass fraction of a nucleus i with atomic weight A_i and the relation $\sum_i A_i Y_i = 1$ holds. The equation $\sum_i Z_i Y_i = Y_e$ with the electron fraction $Y_e = n_e/(\rho N_A)$ accordingly reflects charge neutrality. Equation 5.12 can be rewritten in terms of nuclear abundances and the reaction cross sections already introduced above (Hix & Meyer 2006):

$$\dot{Y}_i = \sum_j \mathcal{N}_j^i \lambda_j Y_j + \sum_{j,k} \mathcal{N}_{j,k}^i \rho N_A \langle j,k\rangle\, Y_j Y_k + \sum_{j,k,l} \mathcal{N}_{j,k,l}^i \rho^2 N_A^2 \langle j,k,l\rangle\, Y_j Y_k Y_l \tag{5.15}$$

where λ_j is the one-body reaction rate for the reactions of the first group. This set of ordinary differential equations describes the evolution of the nuclear abundances Y_i with time and is only determined by the different nuclear reactions.

5.2.2 Numerical implementation

Although the Euler equations can be discretised in a straightforward manner by a replacement of the derivatives with difference quotients, these finite difference methods exhibit several disadvantages. They do not allow for an exact conservation of quantities such as mass, momentum, and energy and since they tend to smear out discontinuities, they cannot be used to resolve shock waves (LeVeque 1998). This is why the LEAFS code is based on a finite volume method. Instead of computing the changes of mass, momentum, and energy, which are defined in the centres of the cells of the computational grid, the fluxes of these quantities between the individual grid cells are calculated for a certain time interval. Afterwards, an update of the mean values of mass, momentum, and energy is performed in each cell. Due to the fact that the finite volume scheme is directly based on the integral formulation of the Euler equations, it is conservative by definition (LeVeque 1998).

In order to calculate hydrodynamical fluxes, the mean values of the conserved quantities that are defined at the cell centres also have to be known at the cell boundaries. The simplest approach to solve this problem consists of a linear extrapolation of the mean values to the cell interfaces and the subsequent solution of the Riemann problem at the resulting discontinuity between two given cells (Godunov 1959). Although higher order extrapolations of the mean values are computationally more expensive, they are more accurate and less diffusive than the original method by Godunov (LeVeque 1998). In the LEAFS code, the *Piecewise Parabolic Method* (PPM) introduced by Colella & Woodward (1984) and the PROMETHEUS implementation by Fryxell et al. (1989) are applied. In multi-dimensional simulations, directional splitting is used and the multi-dimensional Riemann problems are reduced to the one-dimensional case. To guarantee numerical stability, the calculation of the integration time step is based on the Courant-Friedrichs-Lewy (CFL) criterion (Courant et al. 1928). Since the CFL criterion is necessary but not sufficient for numerical stability, a further reduction of the time steps by a Courant factor of 0.8 is incorporated (LeVeque 1998).

In simulations of SN Ia explosions, large differences between the characteristic scales of the problem occur. While the diameter of a Chandrasekhar mass WD is of the order of 10^8 cm, the typical length scale of carbon burning can be as small as $\sim 10^{-4}$ cm in case of deflagrations (cf. Timmes & Woosley 1992) and $\sim 10^{-2}$ cm in case of detonations (cf. Khokhlov 1989). In general, these microscopic scales cannot be resolved in full-star simulations and an approximate treatment for the description of the burning fronts is needed. In the LEAFS code, the level set method first introduced by Osher & Sethian (1988) is applied for this purpose and the nuclear flames are represented as discontinuities defined by the zero level set of a signed scalar distance function (see Reinecke et al. 1999). In n-dimensional simulations, the flame fronts are described as $(n-1)$-dimensional hypersurfaces, and by the use of extensions developed by Sussman et al. (1994) and Smiljanovski et al. (1997), they can be completely coupled to the surrounding flow field.

Since the inclusion of a large nuclear reaction network in the hydrodynamical simulation is computationally very expensive, an alternative approach is chosen in the LEAFS code (see Reinecke et al. 2002). In order to approximate the energy release due to nuclear burning, only five representative species are taken into account to describe the chemical composition: alpha particles, ^{12}C, ^{16}O, "Mg", and "Ni" where the last two are just substitutes for IMEs and IGEs. Behind the burning fronts, the new chemical composition is calculated by the use of tabulated values depending on the initial chemical composition and on the prevailing densities in the respective grid cells. At high densities ($\rho \gtrsim 10^7\,\mathrm{g\,cm^{-3}}$), a mixture of Ni and alpha particles in NSE (cf. Subsection 4.2.1) is synthesised. At lower densities, the burning products mainly consist of IMEs. Depending on density and temperature, the proportion of Ni to alpha particles changes. This is accounted for by the application of a NSE data table (cf. Reinecke 2001).

The detailed nucleosynthetic abundances are determined in a post-processing step with the so-called tracer particle method. Tracer particles are virtual "test particles" that passively follow the hydrodynamical flow and record the evolution of density and temperature on their trajectories. In order to determine the density and temperature values at the positions of the tracer particles, linear interpolations of the values defined by the hydrodynamical Eulerian grid are used. Since each tracer particle represents a certain fluid element in a Lagrangian representation of the SN explosion, the chemical abundances can only be changed by nuclear reactions. Therefore it is possible to calculate the evolution of the nucleosynthetic yields for each tracer particle separately and the chemical composition of the total SN ejecta is calculated by the summation over all tracer particles.

For the simulations of SNe Ia presented in this work, the tracer particles are distributed as described in Travaglio et al. (2004). Additionally, the use of variable tracer masses allows for a better resolution of steep density gradients in low-density regions at the outer edges of the WD (Seitenzahl et al. 2010). The nuclear network that is applied in the post-processing step for the calculation of the nucleosynthetic abundances consists of 384 species ranging from protons, neutrons, and alpha particles up to ^{98}Mo. In order to solve Equation 5.15, a backward Euler algorithm is implemented. More details about the nuclear reaction network and the postprocessing algorithm can be found in Thielemann et al. (1996); Iwamoto et al. (1999) and Röpke et al. (2006a). In contrast to the simulations described in these references, the minimum temperature for the application of the reaction network is lowered to $4 \times 10^8\,\mathrm{K}$. The reaction rates are taken from the REACLIB data base in a release of T. Rauscher and F. K. Thielemann from 2009[2]. Although weak reaction rates are also included in the REACLIB database, they are solely stored as function of temperature. But in degenerate WD matter, weak reaction rates are also density dependent and, for example, β^--rates decrease with increasing density due to the reduced number of available final states for the emitted electron (cf. Langanke & Martinez-Pinedo 2000). This is why the temperature and density dependent values

[2]http://download.nucastro.org/astro/reaclib/

provided by Fuller et al. (1980, 1982a,b, 1985) and Langanke & Martinez-Pinedo (2000) are used.

5.3 Integration of new reaction rate libraries in the post-processing network

In the following two subsections, the applied reaction rates are examined for completeness and up-to-dateness. The influence of certain updates concerning the weak reactions as well as the REACLIB database is studied by comparison of post-processing calculations with previous and current data sets.

5.3.1 Weak reaction rate libraries

For a long time, the tabulations of weak interaction rates by Fuller et al. (1980, 1982a,b, 1985) (FFN) have been the standard for many astrophysical applications. The tables provided by these authors include rates for electron capture, beta decay, positron emission as well as the associated neutrino losses for nuclei with atomic mass numbers from 21 to 60. Using a parametrisation based on the independent particle model and experimental data for low-lying transitions, the authors calculated the weak reaction rates under the assumption of a single Gamov-Teller (GT) resonance. Since nucleon-nucleon correlations lead to a quenching of the total GT strength and a fragmentation of the GT strength distribution over many states in the daughter nucleus, independent particle models are not sufficient to reproduce the GT strength distribution inferred from experimental data (Brown & Wildenthal 1988). Instead, complete shell models have to be taken into account. With this approach, Oda et al. (1994) determined the rates of all relevant weak processes for *sd*-shell nuclei with $A = 17$-39. A few years later, further progress in the efficiency of shell-model calculations and increasing computer power allowed for the computation of weak interaction rates of pf-shell nuclei with $A = 45$-65 (Langanke & Martinez-Pinedo 2000). Since shell-model calculations of nuclei with $A = 40$-44 require the consideration of both *sd*- and pf-shells, fully consistent computations of the weak interaction rates still remain to be done.

In the post-processing calculations, the following combination of weak interaction rates has been implemented so far. For nuclei up to $A = 44$, the rates from FFN have been included, the rates from Langanke & Martinez-Pinedo (2000) have been used for nuclei with $A \geq 45$. Although the FFN rates and the rates determined by more elaborate shell models are mostly in good agreement for *sd*-shell nuclei, Oda et al. (1994) also point out that for high densities and temperatures significant deviations can occur. Especially in cases where FFN had to rely on extrapolations and empirical methods due to a lack of experimental data, differences up to an order of magnitude are found by comparison to the shell-model calculations. This is why

the rates from Oda et al. (1994) have been included now for nuclei up to $A = 39$ in the post-processing network in place of the FFN rates.

In a first step, the nuclear reaction network is tested independently of a complete post-processing of a specific hydrodynamical explosion model. The test calculations are performed for an initial abundance of 50 % ^{12}C and 50 % ^{16}O. This is similar to the initial composition of the WD models used in the hydrodynamical simulations. For different temperature and density conditions, the nuclear network is executed and the new chemical abundances are determined for an integration time of 0.1 s. A comparison of the results for the different compilations of weak reaction rates is shown in Figs. 5.1 and 5.2. For temperatures larger than 6.0×10^9 K, the NSE solver of the reaction network is used.

For most of the 384 isotopes, the nucleosynthetic yields determined with and without the inclusion of the more exact weak interaction rates of Oda et al. (1994) hardly show any difference. Representative examples of the identical evolution of abundances for both libraries of weak reactions are ^{56}Ni and ^{54}Fe in Fig. 5.1 or ^{4}He and ^{58}Ni in Fig. 5.2. Besides the dependency of the abundances on different temperatures, also the variation of the yields with respect to different densities is depicted. Only a few isotopes show significant differences in their abundances at high densities, examples of this behaviour are ^{39}K and ^{34}S in Fig. 5.1 or ^{30}P and ^{26}Al in Fig. 5.2. This is in line with the statement of Oda et al. (1994) that the most pronounced differences between the shell-model weak interaction rates and the older FFN rates appear in the high-density regime. Although these differences occur only for isotopes that are less abundant in the test calculations, the influence of the updated weak reaction rates on the nucleosynthetic yields of a complete hydrodynamical model still has to be investigated.

To this end, a two-dimensional model similar to the N100 model introduced in Subsection 3.3.1 is applied. Although the turbulent flow can be treated more accurately in three-dimensional simulations, the computational effort is much lower in two dimensions and the description of the hydrodynamical evolution is sufficient to draw inferences about the importance of certain reaction rates. With the assumption of an axisymmetric configuration, the hydrodynamical model is simulated on a grid of 512×1024 cells. In order to record the temperature and density conditions during the explosion for the subsequent post-processing step, 41000 tracer particles with variable masses are distributed in the initial setup of the WD. For the initial composition of the post-processing calculations, solar metallicity as given by Asplund et al. (2009) is used and the mass fraction of ^{12}C is accordingly reduced to allow for a preservation of particle number.

For the same hydrodynamical simulation, the post-processing step is performed twice. The first time, the weak reaction rates of FFN are utilised, the second time, these rates are updated with the results of Oda et al. (1994). The results can be inferred from Table 5.1 where the chemical composition of the ejecta is given at 100 s after the explosion. The relative deviations of the nucleosynthetic yields

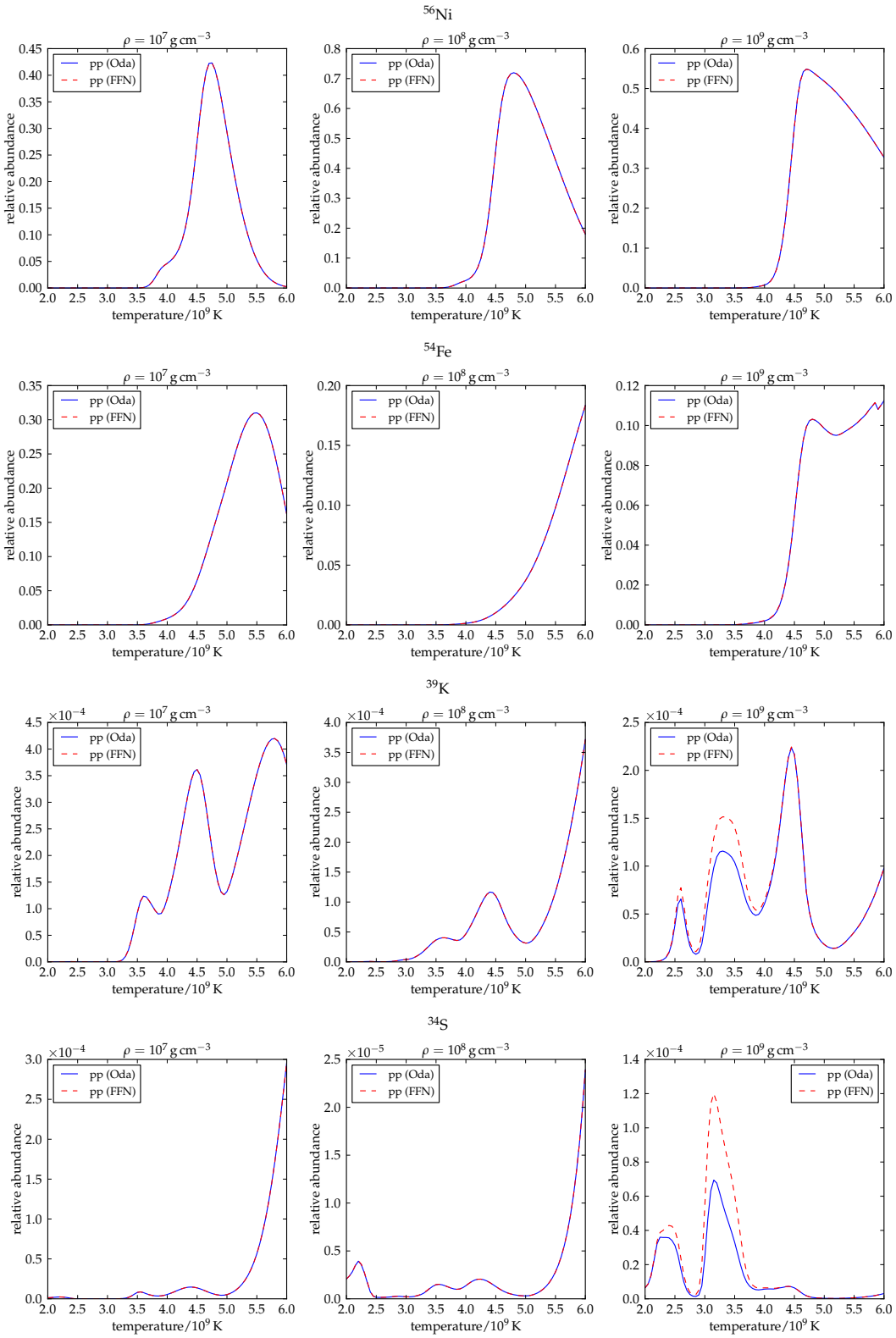

Figure 5.1: Comparison of nuclear reaction network calculations with different libraries of weak reaction rates for selected isotopes. The results for the FFN rates are represented by red dashed lines, the computations based on the shell-model results of Oda et al. (1994) are indicated in blue.

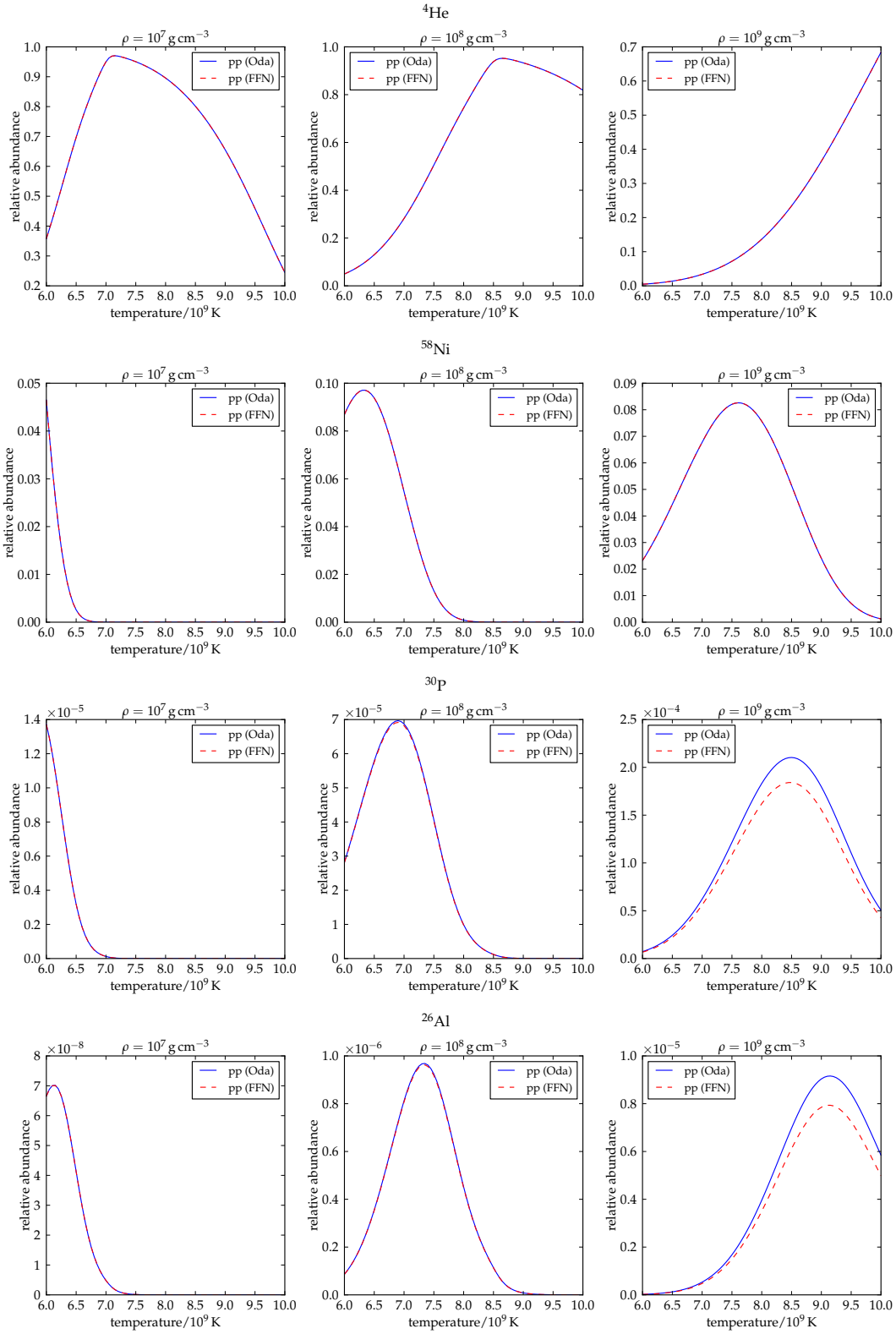

Figure 5.2: Comparison of nuclear reaction network calculations with different libraries of weak reaction rates for selected isotopes by application of the NSE solver. The results for the FFN rates are represented by red dashed lines, the computations based on the shell-model results of Oda et al. (1994) are indicated in blue.

Table 5.1: Comparison of nucleosynthetic yields in case of a two-dimensional delayed-detonation model. While the first post-processing calculation uses the weak reaction rates of FFN (second column), the rates of Oda et al. (1994) are taken into account for the second calculation (third column). For each calculation, the 35 most abundant species at 100 s after the explosion are listed. The relative deviations between the two calculations are given in the fourth column.

isotope	nucleosynthetic yields (FFN rates, in $M_\odot$)	nucleosynthetic yields (Oda rates, in $M_\odot$)	relative deviation (in %)
^{56}Ni	6.0071×10^{-1}	6.0074×10^{-1}	0.0050
^{28}Si	2.8699×10^{-1}	2.8699×10^{-1}	0.0000
^{32}S	1.4025×10^{-1}	1.4025×10^{-1}	0.0000
^{54}Fe	1.0433×10^{-1}	1.0433×10^{-1}	0.0000
^{58}Ni	5.9148×10^{-2}	5.9144×10^{-2}	−0.0068
^{16}O	5.5756×10^{-2}	5.5756×10^{-2}	0.0000
^{56}Fe	2.8893×10^{-2}	2.8876×10^{-2}	−0.0589
^{36}Ar	2.7135×10^{-2}	2.7135×10^{-2}	0.0000
^{40}Ca	2.5507×10^{-2}	2.5507×10^{-2}	0.0000
^{57}Ni	1.3552×10^{-2}	1.3552×10^{-2}	0.0000
^{52}Fe	1.2808×10^{-2}	1.2809×10^{-2}	0.0078
^{24}Mg	1.0687×10^{-2}	1.0687×10^{-2}	0.0000
^{55}Co	1.0377×10^{-2}	1.0378×10^{-2}	0.0096
^{60}Ni	6.0872×10^{-3}	6.0842×10^{-3}	−0.0493
^{55}Fe	3.3482×10^{-3}	3.3468×10^{-3}	−0.0418
^{12}C	2.0059×10^{-3}	2.0059×10^{-3}	0.0000
^{20}Ne	1.5739×10^{-3}	1.5738×10^{-3}	−0.0064
^{57}Co	1.5463×10^{-3}	1.5457×10^{-3}	−0.0388
^{34}S	1.1702×10^{-3}	1.1702×10^{-3}	0.0000
^{53}Fe	1.1513×10^{-3}	1.1514×10^{-3}	0.0087
^{60}Zn	8.8709×10^{-4}	8.8714×10^{-4}	0.0056
^{52}Cr	7.2920×10^{-4}	7.2845×10^{-4}	−0.1030
^{4}He	7.0991×10^{-4}	7.0995×10^{-4}	0.0056
^{30}Si	6.7484×10^{-4}	6.7483×10^{-4}	−0.0015
^{38}Ar	6.2740×10^{-4}	6.2739×10^{-4}	−0.0016
^{59}Ni	6.1356×10^{-4}	6.1338×10^{-4}	−0.0293
^{48}Cr	5.8519×10^{-4}	5.8521×10^{-4}	0.0034
^{29}Si	3.8285×10^{-4}	3.8284×10^{-4}	−0.0026
^{53}Mn	3.8113×10^{-4}	3.8091×10^{-4}	−0.0578
^{50}Cr	3.6915×10^{-4}	3.6912×10^{-4}	−0.0081
^{27}Al	3.4465×10^{-4}	3.4460×10^{-4}	−0.0145
^{31}P	2.1617×10^{-4}	2.1615×10^{-4}	−0.0093
^{62}Zn	1.9868×10^{-4}	1.9868×10^{-4}	0.0000
^{33}S	1.6657×10^{-4}	1.6657×10^{-4}	0.0000
^{56}Co	1.2616×10^{-4}	1.2614×10^{-4}	−0.0159

shown in the fourth column immediately lead to the conclusion that the changes due to the inclusion of the new weak reaction rates are negligible. The biggest difference amounts to 0.1 % and radioactive isotopes like ^{56}Ni, ^{56}Co, ^{52}Fe, and ^{48}Cr that are important for the resulting observables in different wavelength regimes (see Subsection 3.3.2) show no significant deviations at all. Although the shell-model calculations of Oda et al. (1994) reveal short-comings in the previously determined rates by FFN for certain weak interactions, an update of the weak interaction rates has almost no effect on the nucleosynthetic yields that are determined for the typical hydrodynamical conditions of a SN Ia explosion.

5.3.2 REACLIB libraries

Except for the weak reaction rates that are tabulated in dependence on temperature and density (see Subsection 5.3.1), all other nuclear reaction rates in the post-processing calculations are taken from the REACLIB database (see e.g. Cyburt et al. 2010). Being a nuclear reaction rate library that is especially compiled for astrophysical applications, the REACLIB database contains fits to theoretically and experimentally determined rates. The rates are stored as a function of temperature by the use of the following parametrisation (Cyburt et al. 2010):

$$\lambda = \exp\left[a_0 + \sum_{i=1}^{5} a_i T_9^{\frac{2i-5}{3}} + a_6 \ln T_9\right] \tag{5.16}$$

with the temperature T_9 given in units of 10^9 K and seven parameters a_i defining the best fit for the respective reaction rate. The REACLIB library is regularly updated with respect to the available information from experiments and theoretical rate predictions. For the determination of most of the theoretical rates, statistical model calculations with the NON-SMOKER$^{\mathrm{WEB}}$ code are used (Rauscher 2008). Many of the experimentally determined reaction rates are based on the compilations of the NACRE collaboration (Angulo et al. 1999) and the results of Iliadis et al. (2001). If experimentally based reaction rates are available, the theoretical rates are accordingly replaced to obtain higher accuracies. More details about the contents of the REACLIB library can be found in Cyburt et al. (2010).

In the earlier calculations with the post-processing reaction network, the REACLIB database in the version of T. Rauscher and F. K. Thielemann from 2009 has been used (see above). In order to study the effect on the nucleosynthetic yields, these results are compared to calculations with the current release of the REACLIB database, REACLIBV2.0[3]. In both cases, the weak reaction rates from Oda et al. (1994) are included. The way of proceeding is similar to the description in the previous subsection. After a set of test calculations that apply the nuclear network (for

[3]https://groups.nscl.msu.edu/jina/reaclib/db/index.php

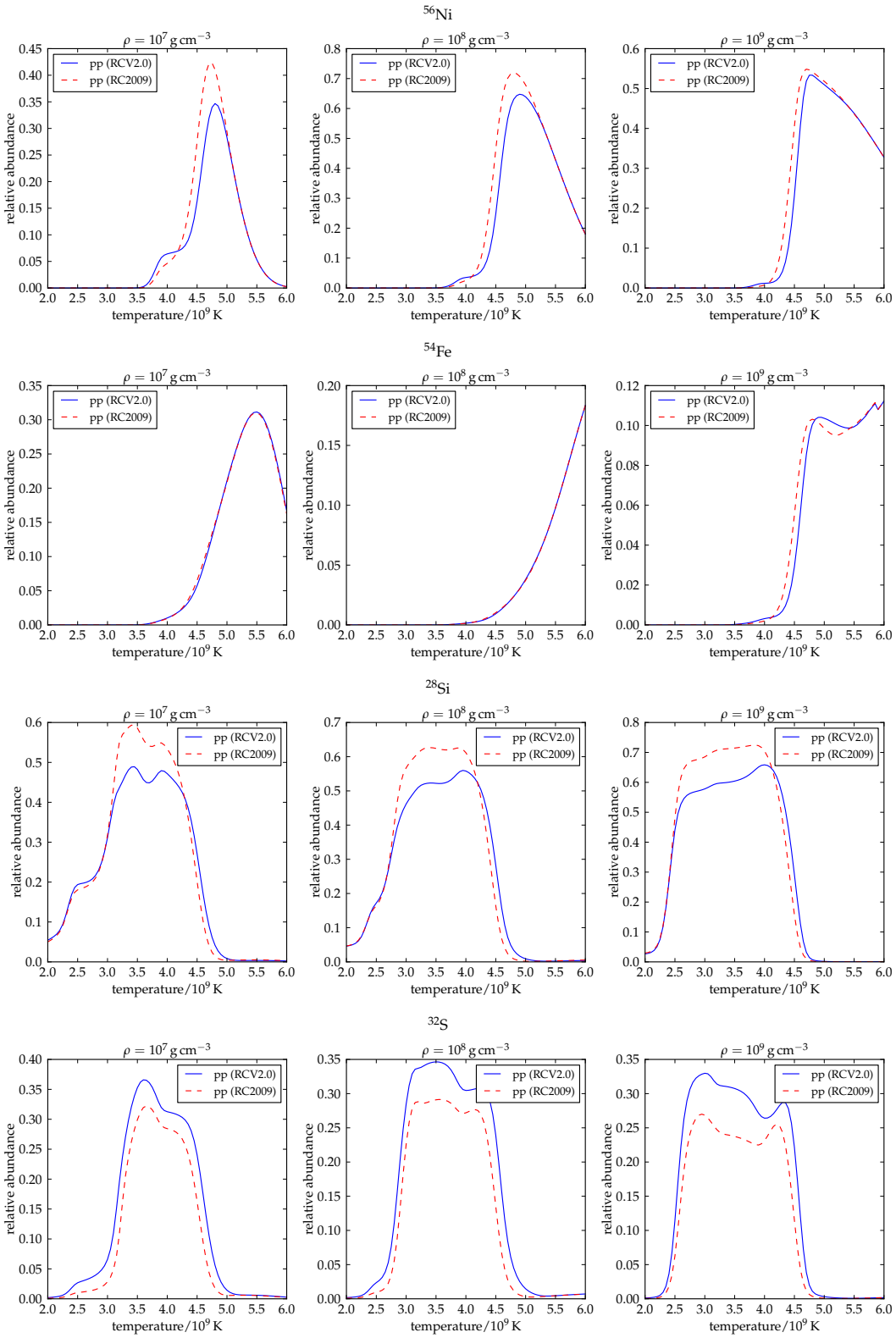

Figure 5.3: Comparison of nuclear reaction network calculations with different versions of the REACLIB library for selected isotopes. The results for the version from 2009 are represented by red dashed lines, the computations based on the current release (V2.0) are indicated in blue.

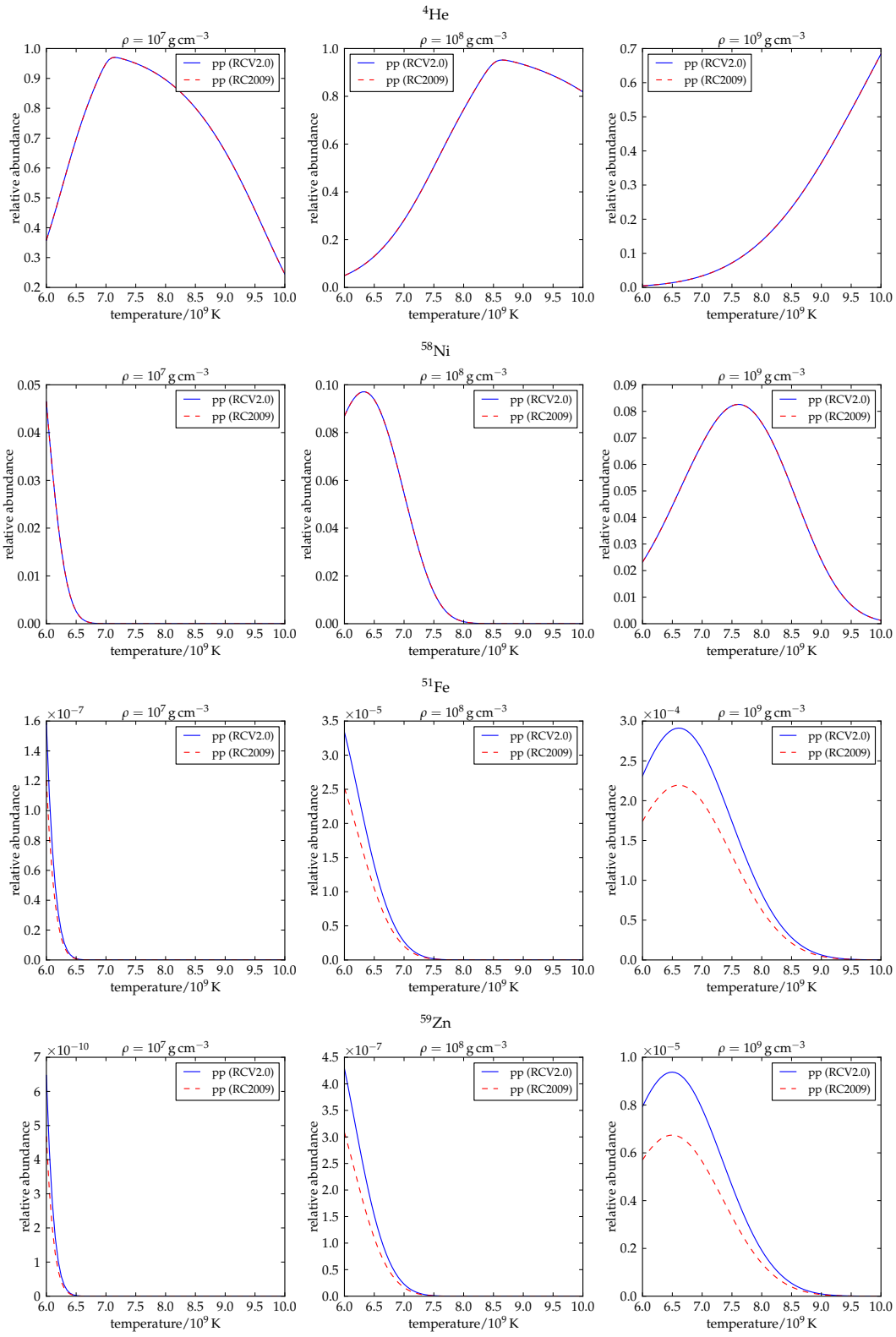

Figure 5.4: Comparison of nuclear reaction network calculations with different versions of the REACLIB library for selected isotopes by application of the NSE solver. The results for the version from 2009 are represented by red dashed lines, the computations based on the current release (V2.0) are indicated in blue.

Table 5.2: Comparison of nucleosynthetic yields in case of a two-dimensional delayed-detonation model. While the first post-processing calculation uses the REACLIB library from 2009 (second column), the current release (V2.0) is taken into account for the second calculation (third column). The 35 most abundant species at 100 s after the explosion are listed. The relative deviations between the two calculations are given in the fourth column.

isotope	nucleosynthetic yields (REACLIB2009, in $M_\odot$)	nucleosynthetic yields (REACLIBV2.0, in $M_\odot$)	relative deviation (in %)
^{56}Ni	6.0074×10^{-1}	5.5150×10^{-1}	−8.2
^{28}Si	2.8699×10^{-1}	2.8376×10^{-1}	−1.1
^{32}S	1.4025×10^{-1}	1.7684×10^{-1}	26.1
^{54}Fe	1.0433×10^{-1}	9.1782×10^{-2}	−12.0
^{58}Ni	5.9144×10^{-2}	7.2925×10^{-2}	23.3
^{16}O	5.5756×10^{-2}	5.9332×10^{-2}	6.4
^{56}Fe	2.8876×10^{-2}	2.8594×10^{-2}	−1.0
^{36}Ar	2.7135×10^{-2}	3.4708×10^{-2}	27.9
^{40}Ca	2.5507×10^{-2}	3.2504×10^{-2}	27.4
^{57}Ni	1.3552×10^{-2}	1.4519×10^{-2}	7.1
^{52}Fe	1.2809×10^{-2}	1.2930×10^{-2}	0.9
^{24}Mg	1.0687×10^{-2}	5.6347×10^{-3}	−47.3
^{55}Co	1.0378×10^{-2}	7.8642×10^{-3}	−24.2
^{60}Ni	6.0842×10^{-3}	6.6408×10^{-3}	9.1
^{55}Fe	3.3468×10^{-3}	3.2470×10^{-3}	−3.0
^{12}C	2.0059×10^{-3}	1.9631×10^{-3}	−2.1
^{20}Ne	1.5738×10^{-3}	1.8902×10^{-3}	20.1
^{57}Co	1.5457×10^{-3}	1.5839×10^{-3}	2.5
^{34}S	1.1702×10^{-3}	1.1364×10^{-3}	−2.9
^{53}Fe	1.1514×10^{-3}	1.0525×10^{-3}	−8.6
^{60}Zn	8.8714×10^{-4}	2.2922×10^{-3}	158.4
^{52}Cr	7.2845×10^{-4}	6.5476×10^{-4}	−10.1
^{4}He	7.0995×10^{-4}	1.2777×10^{-3}	80.0
^{30}Si	6.7483×10^{-4}	4.7509×10^{-4}	−29.6
^{38}Ar	6.2739×10^{-4}	7.2162×10^{-4}	15.0
^{59}Ni	6.1338×10^{-4}	6.9528×10^{-4}	13.4
^{48}Cr	5.8521×10^{-4}	6.8782×10^{-4}	17.5
^{29}Si	3.8284×10^{-4}	3.4240×10^{-4}	−10.6
^{53}Mn	3.8091×10^{-4}	3.4698×10^{-4}	−8.9
^{50}Cr	3.6912×10^{-4}	3.2834×10^{-4}	−11.0
^{27}Al	3.4460×10^{-4}	2.1773×10^{-4}	−36.8
^{31}P	2.1615×10^{-4}	2.7046×10^{-4}	25.1
^{62}Zn	1.9868×10^{-4}	6.9128×10^{-4}	247.9
^{33}S	1.6657×10^{-4}	2.2835×10^{-4}	37.1
^{56}Co	1.2614×10^{-4}	1.2409×10^{-4}	−1.6

the initial conditions see Subsection 5.3.1) without post-processing a specific hydrodynamical model, the nucleosynthetic yields are determined for a two-dimensional delayed-detonation model as introduced above.

The results for the test calculations are shown in Figs. 5.3 and 5.4, for the nuclear reactions at temperatures above 6.0×10^9 K, again the NSE solver is used. Since in NSE all reactions except for the weak interactions are in equilibrium (cf. Subsection 4.2.1), nearly no deviations between the calculations with the two different REACLIB libraries are expected (see e.g. the results for ^{4}He and ^{58}Ni in Fig. 5.4). Only in those cases where the weak reaction rate libraries do not provide density and temperature dependent rates for a certain isotope, the NSE solver has to recourse to the solely temperature dependent weak reaction rates included in the REACLIB database. If these rates have been updated in the new release of the library, the abundances of certain isotopes can change. Examples of this behaviour are given by the two isotopes ^{51}Fe and ^{59}Zn in Fig. 5.4.

More prominent differences that are based on the rate updates in the REACLIBV2.0 release can be seen in Fig. 5.3 where the results for the test calculations in the non-NSE regime are presented. Even for isotopes that are also abundantly produced in SN Ia explosions, partly significant deviations up to 20 % between the two calculations occur in different temperature and density ranges. In order to study the influence of these deviations on the chemical composition of the ejecta in a hydrodynamical explosion model, the post-processing step for the two-dimensional delayed-detonation model is also performed by application of the REACLIBV2.0 library. In Table 5.2, the results are compared to the previous calculations and the relative deviations are given. While the abundances of many isotopes show relative differences of a few percent up to $\sim 25\,\%$, the deviations for several isotopes are significantly larger and can amount up to a factor of three. Nevertheless, the total abundance structure of the different isotopes is relatively robust. This is comparable to the results of Parikh et al. (2013) who studied the effect of varying individual reaction rates by a factor of ten on the nucleosynthesis in SNe Ia. But since an updated release of the REACLIB database includes new values for many reaction rates, the variations shown in Table 5.2 are respectively larger. This underlines the uncertainties that still exist in current reaction rate libraries and immediately translate into the accuracy of the determination of observables from the results of hydrodynamical SN Ia simulations. Since the differences between certain releases of reaction rate libraries can still be quite significant, the dependency of predicted observables from SNe Ia models on nuclear reactions also emphasises the need for further experimental and theoretical efforts in order to reduce the uncertainties for important reaction rates (see also Parikh et al. 2013).

In spite of the uncertainties that still exist for nuclear reaction rates, the reader has to note that besides the respective reaction rates also the hydrodynamical conditions that define the environment for nucleosynthesis processes are decisive for the chemical abundances in the SN ejecta. The distinct observable signatures for two fundamentally different classes of explosion scenarios discussed in the previous two

chapters rely on the one hand on symmetries or asymmetries in the explosion mechanism, the resulting distribution of ^{56}Ni, and the different total ejecta mass (see Chapter 3) or on the other hand on characteristic entropy and density conditions during certain phases of nucleosynthetic processes (see Chapter 4). Although variations of the predicted absolute fluxes may occur to a certain degree, the differences in the observables of the two models do not primarily depend on a precise value of a certain reaction rate and especially the abundances of the isotopes involved in the production of these signatures in a major way prove to be rather robust.

5.4 Implementation of a nuclear reaction network in the LEAFS code

Since detailed nucleosynthesis calculations during the hydrodynamical simulation have not been possible so far, a further project in the course of this thesis was the inclusion of a nuclear reaction network in the Leafs code. This allows for detailed comparisons of the currently applied tracer particle method with in-situ nuclear network calculations and also resolved treatments of nuclear flames may become possible in future three-dimensional SNe Ia simulations.

5.4.1 The nuclear reaction network YANN

Due to the fact that the reaction network used in the post-processing step is especially optimised for the treatment of tracer particle trajectories and lacks a certain modularity that is important for a flexible use of different matrix solvers, network sizes, etc., the nuclear reaction network Yann (Yet Another Nuclear Network) developed by R. Pakmor and P. Edelmann (cf. Pakmor et al. 2012a) is utilised for this purpose. The initial value problem defined by the set of ordinary differential equations in Equation 5.15 can in principle be solved by many different methods, but since the different reaction rates cover a wide range of characteristic timescales, only a few numerical algorithms are capable of dealing with the problem efficiently. The dependence on a wide range of characteristic timescales causes a numerical system to be "stiff" (cf. Higham & Trefethen 1993). In case of explicit methods, stiffness typically occurs when the size of the time step is limited by the requirement of numerical stability instead of numerical accuracy. Since implicit methods are not subject to such limitations, the Bader-Deuflhard algorithm that is based on a semi-implicit midpoint rule (see Bader & Deuflhard 1983) is used for the integration of the nuclear reaction network. As required by the size of the network, a full direct matrix solver or a sparse matrix solver can be applied (cf. Pakmor et al. 2012a).

Since the Leafs code is written in Fortran and the nuclear reaction network Yann is written in C, the interoperability of both codes is ensured by the application of the intrinsic Fortran module `ISO_C_BINDING`. With this standardised mechanism of

Fortran 2003 being also available in most Fortran 95 compilers that partially include Fortran 2003 features, the relevant procedures, types, and global data objects can be defined in such a way that the Fortran code is able to reliably communicate with the C code. For that purpose, an additional module (`yann.F90`) is included in the Leafs code. With this module, it is now possible to call the full network solver as well as the NSE solver of Yann directly in Leafs by the use of the functions `yann_integrate` and `yann_nse_integrate` that solve the nuclear reaction equations for a given temperature, density, and time step. In order to advect the network species with the hydrodynamical flow, they are treated like the five representative species that have already been included in Leafs (see above). In addition to the variable `xnuc` where the abundances of the representative species are stored, a second variable `xnuc_yann` is introduced and the Fortran modules that control the hydrodynamics and the usage of the Riemann solver are accordingly adjusted. The extension of the Leafs code with the nuclear network is carried out in such a way that the Yann network becomes available by the definition of a corresponding preprocessor variable, otherwise the Leafs code is compiled without the Yann code. Due to the modularity of Yann, the network calculations can be adjusted to the respective needs. The network size, the reaction rate libraries or the consideration or non-consideration of certain reaction details (screening, variable temperatures during the integration time step, etc.) can easily be changed and allow for a flexible application of Yann in the Leafs code.

5.4.2 Construction of medium-sized nuclear reaction networks

Network sizes of 384 isotopes as included in the post-processing procedure are far too large for a reasonable application within hydrodynamical simulations. Since the computational effort of a hydrodynamical simulation with an additional nuclear network is totally dominated by the network calculations, the usage of large reaction networks especially in two- and three-dimensional simulations is computationally too costly. This is why two medium-sized nuclear networks have been constructed that allow for further applications within the hydrodynamical SNe Ia simulations. Such a medium-sized reaction network has to fulfill two requirements: On the one hand, the number of isotopes should be small enough to make network calculations feasible within the Leafs code. On the other hand, the reaction network should contain all reactions that are important for the correct energy release during explosive nucleosynthesis in SNe Ia and the number of isotopes should be sufficient to enable radiative transfer calculations with the previously determined abundances. Only then reasonable comparisons between the tracer particle method and in-situ nucleosynthesis calculations are possible and, for example, the reaction network can be used for improvements of approximate treatments of nuclear flames that are currently included in the Leafs code (see Subsection 5.2.2).

For the construction of the medium-sized nuclear reaction networks, the PyYann tool developed by P. Edelmann at the Max Planck Institute for Astrophysics has

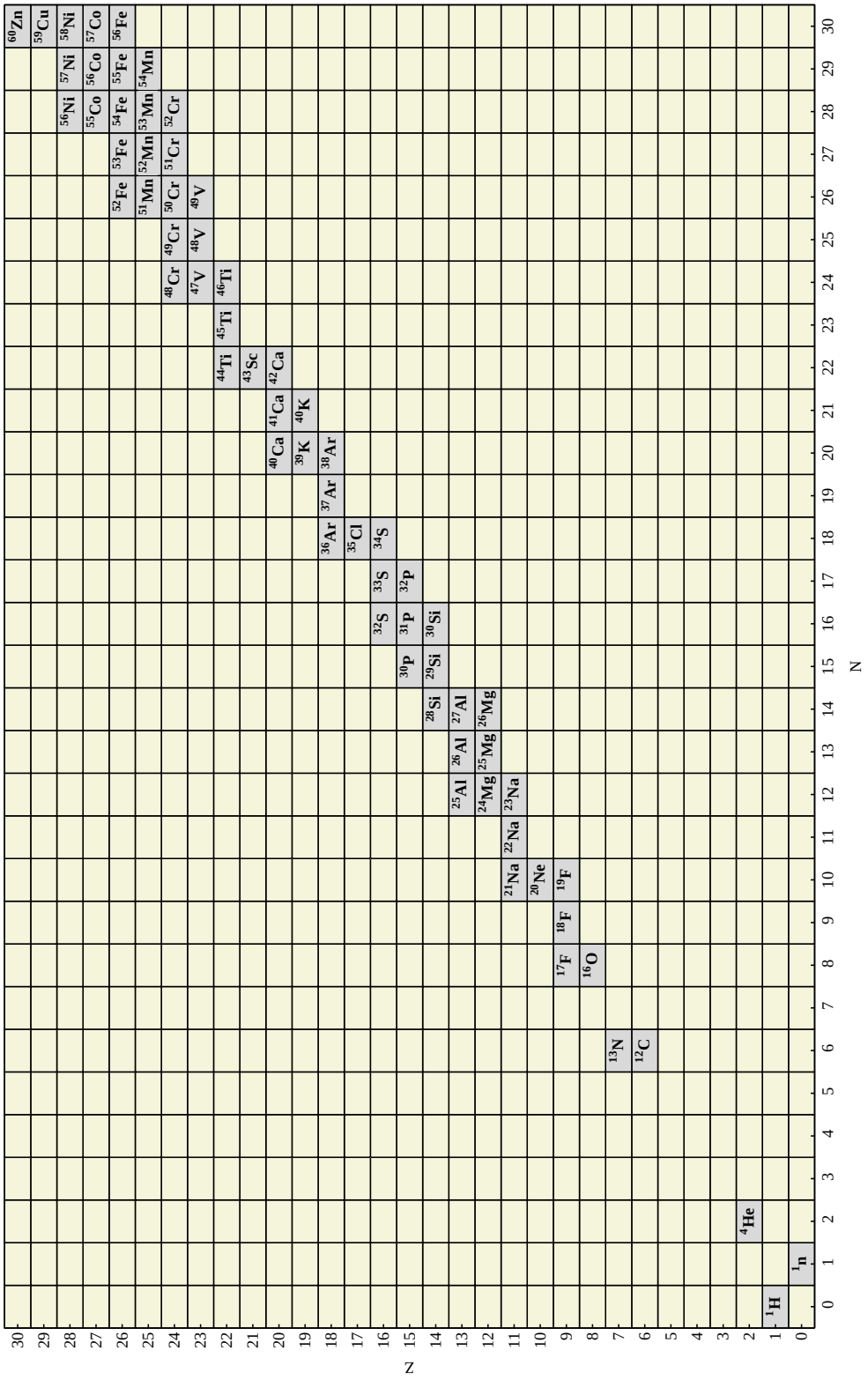

Figure 5.5: Nuclide chart of the reduced nuclear reaction network consisting of 70 isotopes. N, the number of neutrons, is indicated on the x-axis, the number of neutrons Z is given on the y-axis.

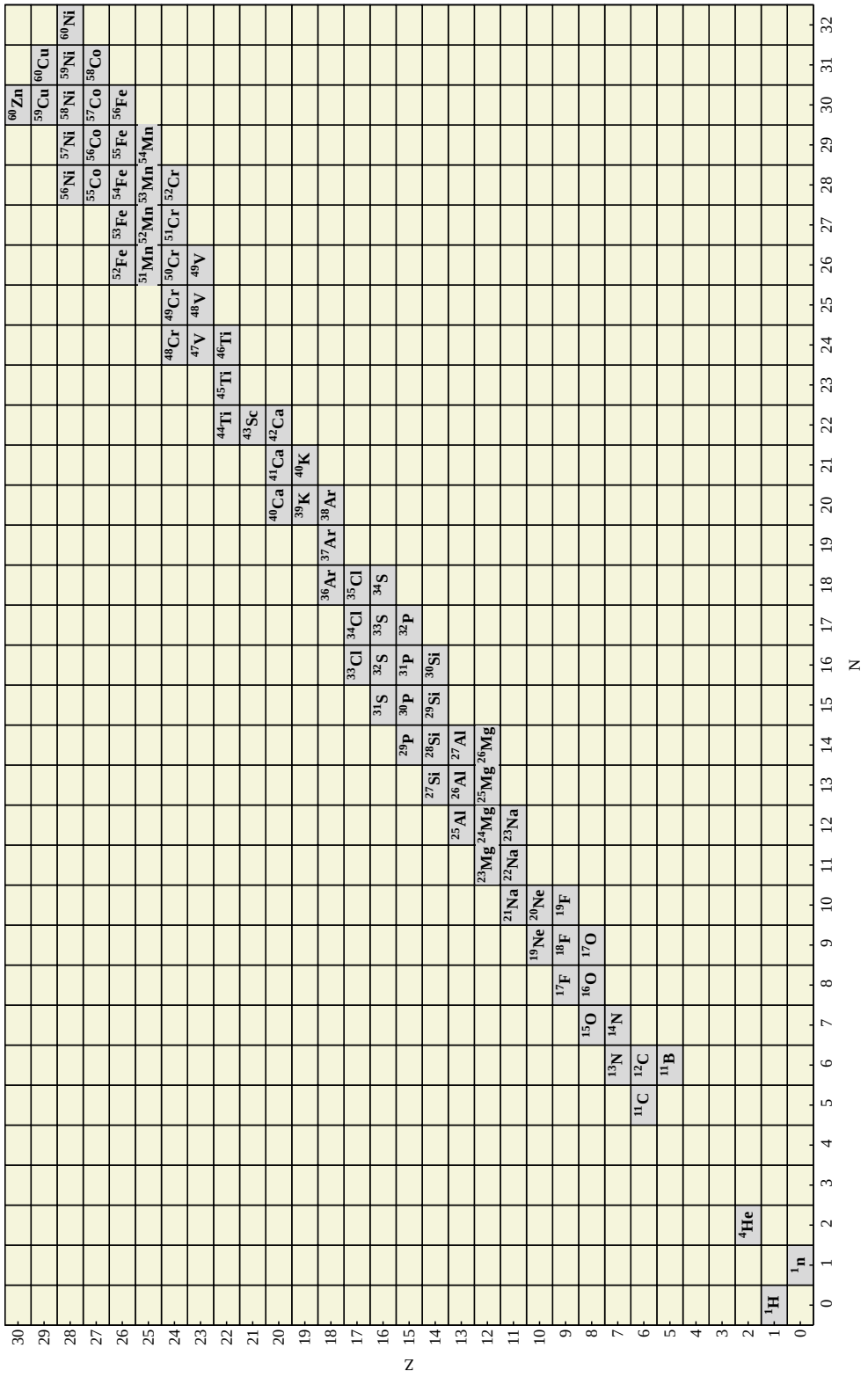

Figure 5.6: Nuclide chart of the reduced nuclear reaction network consisting of 82 isotopes. N, the number of neutrons, is indicated on the x-axis, the number of neutrons Z is given on the y-axis.

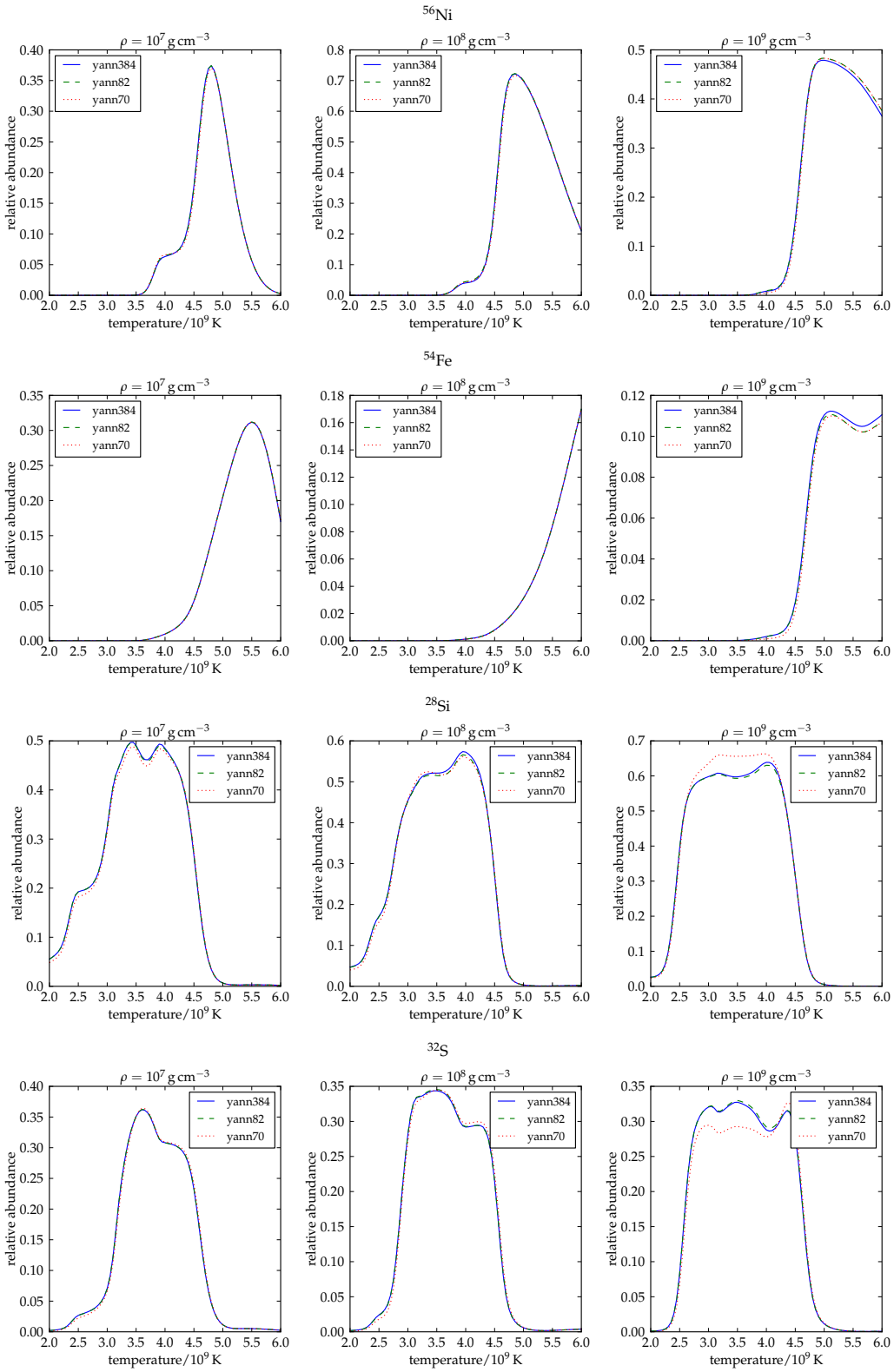

Figure 5.7: Comparison of nuclear reaction network calculations for different network sizes. The results for the large network with 384 isotopes are indicated in blue, the computations for the two medium-sized networks with 82 and 70 isotopes are indicated by green dashed and red dotted lines.

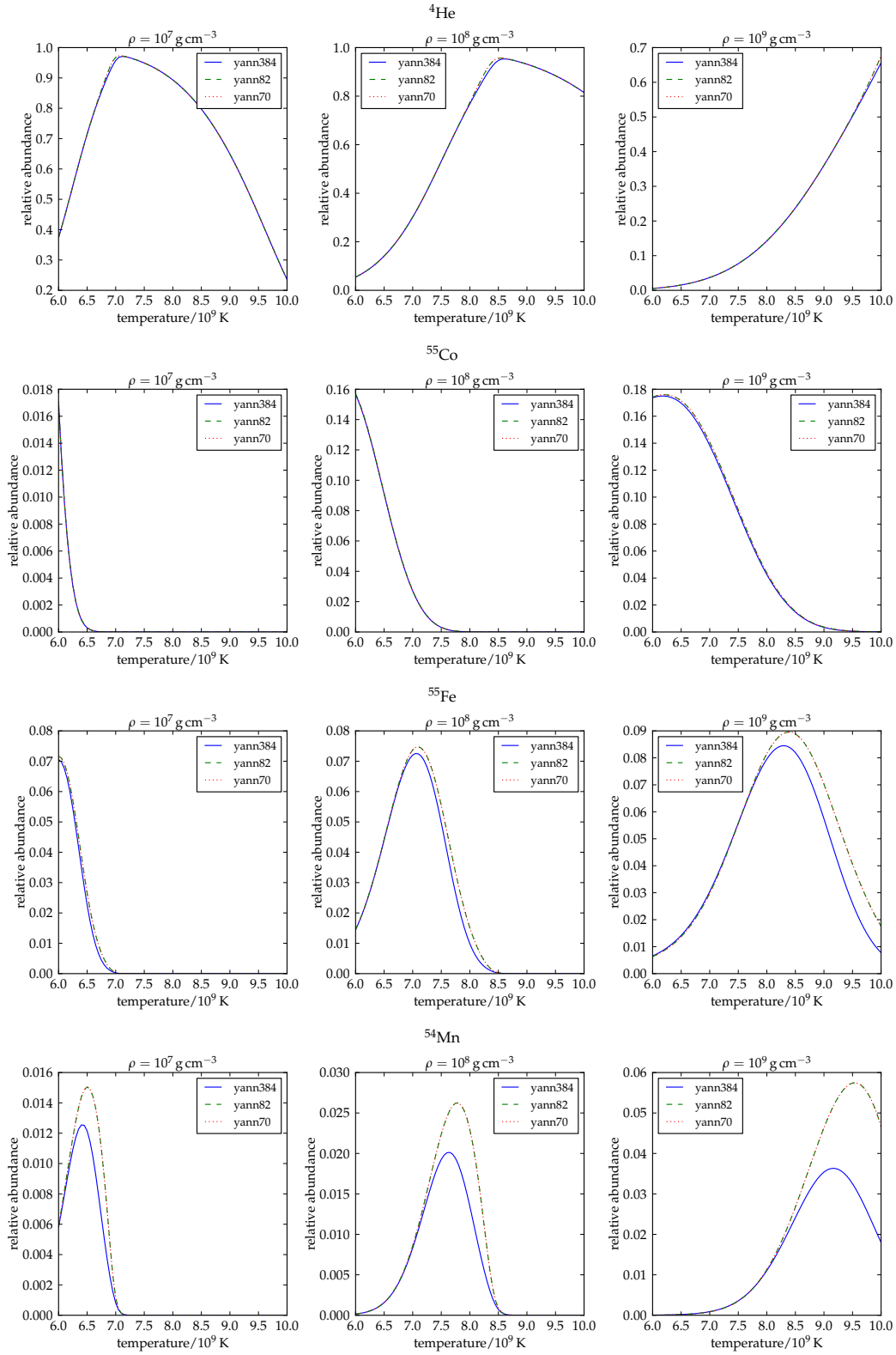

Figure 5.8: Comparison of nuclear reaction network calculations for different network sizes and by application of the NSE solver. The results for the large network with 384 isotopes are indicated in blue, the computations for the two medium-sized networks with 82 and 70 isotopes are indicated by green dashed and red dotted lines.

been used. The graphical user interface of this tool to the nuclear network YANN provides an efficient way to test the importance of certain isotopes and reaction rates for nucleosynthesis calculations. Nucleosynthesis experiments allow for an immediate feedback on the removal or adding of species concerning the resulting energy release and the final nuclear abundances. Initially, the 384 isotopes that are also included in the post-processing calculations serve as starting point. By successively removing isotopes and comparing nucleosynthesis calculations for the reduced network and the previous isotope pattern, the differences with respect to the energy release and to the abundances after a certain integration time are studied. Depending on the deviations from the nucleosynthesis calculations with the large network of 384 isotopes (the difference in the energy release and the abundance of the most frequent isotopes is usually required to be less than 5 %), a certain isotope is removed permanently or added back to the reduced network. With this procedure, finally two nuclear reaction networks consisting of 70 and 82 isotopes could be constructed (see Figs. 5.5 and 5.6).

A comparison of YANN calculations with the large reaction network (384 isotopes) and the two medium-sized networks (70 and 82 isotopes) is given in Figs. 5.7 and 5.8. The abundances of selected isotopes are shown for different densities and temperatures. For the presented results, initial abundances of 50 % ^{12}C and 50 % ^{16}O as well as an integration time of 0.1 s have been assumed. The NSE solver has been used for temperatures above 6.0×10^9 K. The calculations with the large network and the two medium-sized networks are in good agreement for the most abundant isotopes. Since more reactions are accessible in the network with 82 isotopes, the deviations with respect to the large reaction network are smaller than those of the nuclear network with 70 isotopes (see e.g. the results for ^{28}Si and ^{32}S in Fig. 5.7). In general, a more precise determination of nuclear abundances and of the energy release always comes at the expense of computational efficiency and depending on the application of the nuclear network, both parts have to be weighed up. The fact that a reduction of a nuclear network by more than 300 isotopes cannot be realised without accepting larger differences in the abundances for certain isotopes can be inferred from Fig. 5.8. For the examples of ^{55}Fe and ^{54}Mn, more pronounced deviations occur in certain density and temperature regimes. Due to the smaller number of isotopes in case of the medium-sized reaction networks, some weak reaction chains, which these two isotopes are part of, cannot take place any more, or due to a lack of alternative reactions, these two isotopes are produced more abundantly than in case of the large reaction network.

Nevertheless, the two newly constructed reaction networks consisting of 70 and 82 isotopes generally reproduce the energy release and the abundance pattern of the larger network for many applications with sufficient accuracy. With the implementation of YANN in the LEAFS code, the network size can easily be adjusted as required by the considered operating site, and depending on the available computing power, also larger reaction networks can be used.

6 Summary and outlook

In this work, high-energy observables arising during different phases of SN explosions are studied with respect to their potential for allowing conclusions on suggested explosion scenarios and physical mechanisms that are thought to influence the evolution of SNe in a major way. The focus on selected observables at keV and MeV energies is motivated by the appearance of large degeneracies that can even be found for disparate scenarios in many wavelength regimes. Since the discussed emission in the high-energy regime is directly linked to nuclear processes being usually very distinct for different suggested physical models, the signatures at keV and MeV energies allow for meaningful comparisons of simulations with observations.

By the modelling of high-energy observables of SN explosions, several open issues concerning different aspects of SNe are addressed in this work. The first issue concerns the connection between SNe and the acceleration of CRs. Especially the shock fronts of SNRs, which build up when the ejecta are driven into the ambient medium after the explosion, provide an ideal environment for diffusive shock acceleration processes. But so far, unambiguous conclusions on SNRs as acceleration sites of particles with energies up to 10^{15} eV have remained elusive since leptonic and hadronic emission models cannot easily be disentangled by observations in the GeV and TeV regime. In Chapter 2, it is shown that the interactions of accelerated hadronic particles with nuclei in the ambient medium produce characteristic signatures at MeV energies that immediately reveal the existence of efficient acceleration processes. By observation of these so-called nuclear de-excitation lines, conclusions on the composition of the ejecta and the cosmic rays as well as the acceleration mechanisms are possible. If a new telescope mission with the currently proposed sensitivities is launched in the near future (for example the GRIPS mission), the definite verification or falsification of CR acceleration theories will come into reach, and a major step towards the identification of the origin of Galactic CRs can be done.

As discussed in Chapter 3, gamma-ray emission in the MeV energy range cannot only provide evidence for cosmic-ray acceleration sites, but also serves as a diagnostic tool for the explosion and progenitor scenarios of SNe Ia. In contrast to core-collapse SNe, progenitor systems of SNe Ia have not been observed so far and despite the importance of this distinct class of explosion events for various branches of astrophysics, the contributions of different proposed progenitor scenarios to the total number of SNe Ia remain unclear and the question of the realisation of certain proposed explosion mechanisms in nature is far from being solved. The validation of

different physical models by comparing sophisticated three-dimensional simulations with observations can be further complicated by large viewing-angle dependencies of line fluxes as well as integrated fluxes over a broader energy range. In Chapter 3, it is shown that the gamma radiation at a few MeV can be used to constrain explosion models of SNe Ia. Originating mainly from the decays of ^{56}Ni and ^{56}Co in the first weeks after explosion, the gamma-ray emission provides information about the distribution of the radioactive isotopes and the composition of the ejecta. Other than, for example, the optical or infrared emission that leaves the SN ejecta after complex conversion processes of the initial gamma-ray photons and strongly depends on the detailed atomic level populations, the evolution of the gamma-ray emission is mainly influenced by the half-lives of the radioactive isotopes and the branching ratios of the resulting spectral lines. The dominant interaction processes of gamma-ray photons in this energy regime are Compton scatterings. Photoelectric absorption and pair production are less important. Due to the relative simplicity of the gamma-ray emission, the detection of fully resolved spectral lines is often not required for the deduction of information about the underlying explosion scenario. According to the results in Chapter 3, even bolometric measurements or the determination of flux ratios of broader energy bands (hardness ratios) are sufficient to differentiate between two explosion models (a violent merger and a delayed-detonation model) that represent the two suggested main progenitor channels of SNe Ia. Detector simulations of a proposed next-generation gamma-ray telescope show that a distinction between the two explosion models is possible up to the distance of the Virgo cluster ($\sim 16\,\mathrm{Mpc}$).

In Chapter 4, the search for characteristic signatures of the two different SN Ia explosion models is extended to the X-ray regime. By a thorough study of the nucleosynthesis conditions in the violent merger and the delayed-detonation models, it is shown that the abundance of the radioactive isotope ^{55}Fe is very sensitive to the entropy and density conditions during the freeze-out from NSE. Since the daughter nucleus ^{55}Mn produces an X-ray line at 5.9 keV, the abundance of ^{55}Fe and therefore the conditions during explosive nucleosynthesis can be inferred from X-ray observations. With the half-life of ^{55}Fe (2.7 yr) and the evolution of the opacity of the ejecta at keV energies, the optimal time frame for observations of the 5.9 keV line is determined by radiative transfer calculations and found to be approximately six years after explosion. A detailed consideration of continuum emission processes that can potentially reduce the chances of a line detection gives rise to the conclusion that these X-ray backgrounds can be neglected in most cases. Detector simulations of current and planned X-ray instruments show that a distinction of the two explosion models is feasible for distances up to 1 Mpc with XMM-Newton/pn for reasonable exposure times. This distance limit can be further enlarged by future large-scale missions such as Athena+. In case of the delayed-detonation model where more ^{55}Fe is synthesised than in the violent merger model, a line detection is also possible for larger distances. Due to the fact that ^{55}Fe is produced much less abundantly than the isotopes ^{56}Ni and ^{56}Co that are responsible for the gamma-ray emission at

early times, the line flux at 5.9 keV is significantly reduced compared to the fluxes in the gamma-ray regime. This is why measurements of the 5.9 keV line do not allow for the same distance limits as the gamma-ray detections discussed in Chapter 3.

The results presented in Chapters 3 and 4 indicate that exact predictions of observables that can finally lead to a distinction of different SN Ia models are not possible without a precise treatment of nuclear reactions during the explosion. While the approximate energy release due to nuclear burning is inferred from calibrated tables, the detailed nucleosynthetic abundances are determined in a post-processing step in the current setup of the simulations. The reaction rates that are used by the applied nuclear reaction networks are still subject to pronounced experimental and theoretical uncertainties. In Chapter 5, previous post-processing calculations and calculations that are based on recently updated reaction rate libraries are compared and it is shown that deviations in the abundances of the most important isotopes of $\sim 25\,\%$ can occur. Although the distinct signatures discussed in Chapters 3 and 4 are not severely affected by these deviations since they only depend on fundamental properties such as explosion asymmetries or temperature and density conditions, uncertainties in the reaction rates of course influence the prediction of absolute fluxes by radiative transfer calculations. Therefore it is evident that further experimental and theoretical efforts are needed for determining the nuclear reaction rates as precisely as possible at the temperature and density conditions that are relevant for SN explosions.

In order to allow for a flexible treatment of nuclear reactions also during the hydrodynamical simulations, a nuclear reaction network has been included directly into the SN code during this work. Since in-situ calculations with large nuclear reaction networks are still computationally too demanding, two medium-sized networks with 82 and 70 isotopes are constructed in such a way that the differences are as small as possible concerning the energy release and the abundances of the most important isotopes compared to a large network with several hundred isotopes. This enables further developments of the SN code in the future and approximations for certain processes that have been used up to now can be replaced by in-situ network calculations. Additionally, increasing computer power may lead to the possibility of replacing the post-processing method by using larger reaction networks also directly in three-dimensional hydrodynamical simulations.

To continue this approach, two-dimensional SNe Ia simulations with in-situ network calculations are currently carried out by the use of the medium-sized reaction network consisting of 70 isotopes. Since these simulations are still computationally challenging, computing time at the Jülich Supercomputing Centre is partly used for this purpose. As a first step, the network is only passively coupled to the hydrodynamical evolution. Similar to the tracer particle method, the nucleosynthetic abundances are calculated in dependence on the prevailing temperature and density conditions and the 70 species are advected with the flow. But in contrast to the Lagrangian approach of the tracer particles and the calculation of the nucleosynthetic abundances in a post-processing step, the abundances are now directly

determined on the Eulerian grid during the hydrodynamical simulation. To increase the efficiency of the computations, the reaction network is only executed every few hydrodynamical time steps. The optimal time step size for the reaction network calculations that allows both for efficient and accurate in-situ computations of the nucleosynthetic yields is still subject to current research and detailed comparisons of this method with the post-processing approach have already been initiated.

In summary, the results of this work underline that further progress concerning unresolved issues such as the origin of Galactic CRs or the progenitor scenarios of SNe Ia can only be achieved by comparing theoretical predictions and observational evidences over a broad range of wavelengths. The conclusions in view of the large degeneracies that fundamentally different physical models often exhibit in the commonly investigated wavelength regimes have to be two-fold: On the one hand, theoretical models should thoroughly be investigated towards characteristic observable signatures at multiple energies. As shown in this work, especially those observables that are directly linked to nuclear processes are well-suited for this purpose. Of course, this has to be combined with a further refinement of nuclear network calculations and a reduction of the theoretical and experimental uncertainties of the reaction rates that are applied in the simulations. On the other hand, this multi-wavelength approach has also to be supported by respective observations. At the moment, no satellite mission covering the MeV energy range with sufficient sensitivities is available and the information that is provided by nuclear de-excitation lines or gamma-ray emission from radioactive decay is simply lost. Therefore, the results of this thesis also encourage further efforts towards the realisation of a detection instrument at MeV energies in the near future. Furthermore, especially in case of the differentiation of various models of SNe Ia, the importance of combining observables arising at different time windows after explosion is evident. Only if multi-wavelength and time evolution aspects of physical models are taken into consideration in a complementary approach from both theoretical and observational sides, further progress concerning the question of SN Ia progenitors seems to be possible.

Zusammenfassung

In der vorliegenden Arbeit werden Hochenergie-Beobachtungsgrößen, die während verschiedener Phasen von Supernova-Explosionen entstehen, hinsichtlich der Möglichkeit von Rückschlüssen auf vorgeschlagene Explosionsszenarien und physikalische Mechanismen, welche einen wichtigen Einfluss auf die Entwicklung dieser Explosionen ausüben, untersucht. Die Schwerpunktsetzung auf Beobachtungsgrößen im keV- und MeV-Energiebereich ist dabei durch die großen Ähnlichkeiten begründet, die grundverschiedene Szenarien in ihrer Emission in vielen Wellenlängenbereichen zeigen. Da die diskutierten Beobachtungsgrößen im Hochenergie-Bereich direkt mit nuklearen Prozessen verknüpft sind, die bei unterschiedlichen physikalischen Modellen sehr charakteristisch ausgeprägt sein können, eignen sich gerade die vorgestellten Signaturen im keV- und MeV-Bereich für aussagekräftige Vergleiche von Simulationen und Beobachtungen.

Mehrere offene Fragen, die verschiedene Aspekte von Supernova-Explosionen betreffen, werden in dieser Arbeit mit Hilfe der Modellierung von Hochenergie-Beobachtungsgrößen behandelt. Als erstes zentrales Thema wird auf die Verbindung zwischen Supernova-Explosionen und Beschleunigungsmechanismen kosmischer Strahlung eingegangen. Die Schockfronten von Supernova-Überresten, die entstehen, wenn die Materieauswürfe nach der Explosion in das Umgebungsmedium getrieben werden, stellen ideale Bedingungen für das Auftreten von diffusiven Schockbeschleunigungsprozessen dar. Allerdings waren eindeutige Rückschlüsse auf die Existenz von solchen Beschleunigungsprozessen, aufgrund derer Teilchen Energien von bis zu 10^{15} eV erreichen können, in Supernova-Überresten bisher meist nicht möglich, da leptonische und hadronische Emissionsmodelle durch Beobachtungen im GeV- und TeV-Bereich nicht einfach zu unterscheiden sind.

Im zweiten Kapitel wird gezeigt, dass die Wechselwirkungen von beschleunigten hadronischen Teilchen mit Atomkernen im Umgebungsmedium charakteristische Signaturen produzieren, die die Existenz von effizienten Beschleunigungsprozessen unmittelbar offenbaren. Die Beobachtung von solchen sogenannten nuklearen Deexzitationslinien erlaubt direkte Rückschlüsse auf die Zusammensetzung der Materieauswürfe und der kosmischen Strahlung sowie auf die Beschleunigungsmechanismen selbst. Durch den Start einer neuen Satellitenmission mit den gegenwärtig geplanten Sensitivitäten (hier sei auf die vorgeschlagene GRIPS-Mission verwiesen) kommt eine eindeutige Überprüfung von Theorien zur Beschleunigung von kosmischer Strahlung in Reichweite. Dies ermöglicht einen großen Schritt in Richtung der Identifizierung von Beschleunigungsorten kosmischer Strahlung innerhalb unserer Galaxie.

Wie im dritten Kapitel ausgeführt wird, bietet die Gamma-Emission im MeV-Energiebereich nicht nur die Nachweismöglichkeit von Beschleunigungsorten der kosmischen Strahlung, sondern dient auch als Diagnosewerkzeug für Explosions- und Vorläuferszenarien von Typ Ia-Supernovaexplosionen. Im Gegensatz zu Kernkollaps-Supernovaexplosionen wurde bisher kein Vorläufersystem für Supernovae vom Typ Ia beobachtet. Trotz der Bedeutung dieser speziellen Klasse von Supernovaexplosionen für verschiedene Bereiche der Astrophysik ist der genaue Anteil der vorgeschlagenen Vorläuferszenarien an der Gesamtheit der Typ Ia-Supernovae bisher unbekannt und die Frage nach der grundsätzlichen Realisierung bestimmter diskutierter Explosionsmechanismen weitgehend ungeklärt. Eine weitere Schwierigkeit bei der Validierung verschiedener physikalischer Modelle durch den Vergleich von detaillierten dreidimensionalen Simulationen mit Beobachtungsdaten ergibt sich durch die Tatsache, dass starke Abhängigkeiten der Linienflüsse wie auch der über einen größeren Energiebereich integrierten Flüsse vom Sichtwinkel zur Supernovaexplosion die Unterscheidung verschiedener Modelle deutlich erschweren können.

Im dritten Kapitel wird gezeigt, dass die Gammastrahlung bei einigen MeV herangezogen werden kann, um Explosionsmodelle von Typ Ia-Supernovae weiter einzuschränken. Die Gamma-Emission, die hauptsächlich aus den Zerfällen von ^{56}Ni und ^{56}Co in den ersten Wochen nach der Explosion stammt, beinhaltet Informationen über die Verteilung der radioaktiven Isotope und über die Zusammensetzung der Materieauswürfe. Anders als beispielsweise die Emission im optischen oder infraroten Wellenlängenbereich, die die Materieauswürfe erst nach komplizierten Konversionsprozessen der anfänglich erzeugten Gammaphotonen verlässt und stark von den detaillierten Besetzungszahlen der atomaren Energieniveaus abhängt, wird die Gamma-Emission nahezu ausschließlich durch die Halbwertszeiten der radioaktiven Isotope sowie durch die Verzweigungsverhältnisse der resultierenden Spektrallinien bestimmt. Die dominierenden Wechselwirkungsprozesse der Gammaphotonen in diesem Energiebereich sind Compton-Streuungen. Photoelektrische Absorptionen oder Paarproduktionsprozesse sind weniger wichtig. Aufgrund dieser relativ einfachen Struktur der Gamma-Emission wird die Detektion von gut aufgelösten Spektrallinien häufig nicht benötigt, um Informationen über das zugrunde liegende Explosionsszenario zu erhalten. Entsprechend den Ergebnissen von Kapitel 3 können selbst bolometrische Messungen oder die Bestimmung von Flussverhältnissen in breiteren Energiebändern (sog. Härteverhältnisse) ausreichen, um zwei Explosionsmodelle (ein Modell einer sog. gewaltsamen Verschmelzung zweier weißer Zwerge sowie ein Modell einer sog. verzögerten Detonation in einem weißen Zwerg, der Masse von einem nichtentarteten Begleitstern akkretiert) zu unterscheiden, die die beiden hauptsächlich diskutierten Vorläuferszenarien von Typ Ia-Supernovae repräsentieren. Detektorsimulationen eines Gammastrahlen-Teleskops der derzeit vorgeschlagenen nächsten Generation zeigen, dass eine Unterscheidung zwischen den beiden Explosionsmodellen bis zu der Entfernung des Virgo-Klusters ($\sim 16\,\mathrm{Mpc}$) möglich ist.

Im vierten Kapitel wird die Suche nach charakteristischen Signaturen der beiden unterschiedlichen Typ Ia-Explosionsmodelle in den Röntgenenergiebereich ausge-

weitet. Durch eine sorgfältige Analyse der Nukleosynthese-Bedingungen im Modell der gewaltsamen Verschmelzung zweier weißer Zwerge sowie im Modell der verzögerten Detonation wird gezeigt, dass die Häufigkeit des radioaktiven Isotops ^{55}Fe sehr empfindlich auf die Entropie- und Dichtebedingungen reagiert, die während des Ausfrierens der nuklearen Reaktionen aus dem nuklearen statistischen Gleichgewicht bestehen. Da der Tochterkern ^{55}Mn Photonen mit Energien von 5.9 keV emittiert, können Röntgenbeobachtungen dazu genutzt werden, die Häufigkeit von ^{55}Fe und damit die Bedingungen, die während der explosiven Nukleosynthese geherrscht haben, zu bestimmen. Unter Berücksichtigung der Halbwertszeit von ^{55}Fe und der Opazitätsentwicklung der Materieauswürfe bei keV-Energien wird das optimale Zeitfenster für Beobachtungen der 5.9 keV-Linie bestimmt, welches etwa bei sechs Jahren nach der Explosion liegt. Eine detaillierte Betrachtung von Prozessen, die zur Kontinuumsemission bei keV-Energien beitragen und die Erfolgsaussichten einer Liniendetektion potentiell stark verringern können, ergibt, dass diese Emissionsprozesse in den meisten Fällen vernachlässigt werden können. Detektorsimulationen von aktuell verfügbaren und geplanten Röntgeninstrumenten zeigen, dass im Falle von XMM-Newton/pn bei realistischer Beobachtungsdauer eine Unterscheidung der beiden Explosionsmodelle bis zu einer Entfernung von 1 Mpc möglich ist. Diese Entfernungsgrenze kann mit Hilfe von zukünftigen Röntgenteleskopen wie der vorgeschlagenen „Athena+“-Mission weiter erhöht werden. Im Falle des Modells der verzögerten Detonation, wo ^{55}Fe deutlich häufiger produziert wird als im Modell der gewaltsamen Verschmelzung zweier weißer Zwerge, sind Detektionen der Röntgenlinie auch für größere Entfernungen möglich. Aufgrund der Tatsache, dass ^{55}Fe in deutlich geringeren Mengen als die Isotope ^{56}Ni und ^{56}Co, die für die frühe Gamma-Emission verantwortlich sind, produziert wird, ist der Linienfluss bei 5.9 keV auch deutlich geringer als die entsprechenden Flüsse im Gammabereich. Dadurch sind mit Messungen der 5.9 keV-Linie nicht die gleichen Entfernungen bezüglich der Unterscheidung von Explosionsmodellen zu erreichen wie mit der in Kapitel 3 diskutierten Gamma-Emission im MeV-Bereich.

Die Ergebnisse, die in den Kapiteln 3 und 4 dargestellt werden, zeigen, dass genaue Vorhersagen von Beobachtungsgrößen, die schließlich zu einer Unterscheidung von verschiedenen Explosionsmodellen von Typ-Ia-Supernovae führen, nicht ohne die präzise Behandlung von Kernreaktionen während der Explosion erfolgen können. Während bei den gegenwärtig verwendeten Simulationen die Energiefreisetzung durch nukleares Brennen näherungsweise mit Hilfe von kalibrierten Tabellen bestimmt wird, erfolgt die Berechnung der detaillierten Isotopenhäufigkeiten in einem Post-Prozessierungsschritt. Die Reaktionsraten, die in den nuklearen Reaktionsnetzwerken verwendet werden, unterliegen immer noch größeren experimentellen und theoretischen Unsicherheiten.

Im fünften Kapitel werden bisherige Post-Prozessierungsrechungen mit Rechnungen verglichen, die kürzlich aktualisierte Bibliotheken von Reaktionsraten verwenden. Es wird gezeigt, dass auch bei den am häufigsten auftretenden Isotopen Unterschiede von bis zu 25 % auftreten können. Auch wenn die Signaturen, die in Kapitel 3

und 4 diskutiert werden, von solchen Abweichungen nur wenig beeinflusst werden, da sie von fundamentalen Eigenschaften wie Explosionsasymmetrien oder den vorherrschenden Temperatur- und Dichtebedingungen abhängen, wirken sich die Unsicherheiten in den Reaktionsraten natürlich auf die Vorhersage von absoluten Flüssen durch Strahlungstransportrechnungen aus. Daher wird deutlich, dass weitere experimentelle und theoretische Anstrengungen unternommen werden müssen, um die Reaktionsraten bei den in Supernovaexplosionen vorherrschenden Temperatur- und Dichtebedingungen möglichst präzise zu bestimmen.

Um eine flexible Behandlung von Kernreaktionen auch während der hydrodynamischen Simulationen zu ermöglichen, wird während dieser Arbeit auch ein nukleares Reaktionsnetzwerk direkt in den Supernova-Code integriert. Da in-situ-Rechnungen mit großen Reaktionsnetzwerken zu aufwändig sind, werden zwei mittelgroße Netzwerke mit 82 und 70 Isotopen so konstruiert, dass die Unterschiede bezüglich der Energiefreisetzung und der Häufigkeit der wichtigsten Isotope im Vergleich zu einem großen Netzwerk mit mehreren hundert Isotopen möglichst gering sind. Dies erlaubt weitere Verbesserungen des Supernova-Codes, und Näherungsverfahren, die bisher für verschiedene Prozesse benutzt wurden, können in Zukunft durch in-situ-Netzwerkrechnungen ersetzt werden. Weiterhin wird die immer größere zur Verfügung stehende Rechenleistung dazu führen, dass die bisher verwendete Post-Prozessierungsmethode auch durch große nukleare Reaktionsnetzwerke, die direkt in den Supernova-Code integriert sind, ersetzt werden kann.

Um diesen Ansatz fortzuführen, werden derzeit zweidimensionale Simulationen von Typ-Ia-Supernovaexplosionen unter Benutzung des mittelgroßen Reaktionsnetzwerks mit 70 Isotopen durchgeführt. Da diese Simulationen immer noch eine Herausforderung hinsichtlich des Rechenaufwandes darstellen, wird für diesen Zweck teilweise Rechenzeit am Jülich Supercomputing Centre genutzt. In einem ersten Schritt wird das Reaktionsnetzwerk nur passiv mit der hydrodynamischen Entwicklung gekoppelt. Ähnlich wie bei der Tracer-Partikel-Methode werden die Isotopenhäufigkeiten in Abhängigkeit von den vorherrschenden Temperatur- und Dichtebedingungen berechnet und die 70 Isotope werden mit dem Strom advektiert. Aber im Gegensatz zu dem Lagrangeschen Ansatz der Tracer-Partikel und der Berechnung der Isotopenhäufigkeiten in einem Post-Prozessierungsschritt werden die Häufigkeiten nun direkt auf dem Eulerschen Gitter während der hydrodynamischen Simulation bestimmt. Um die Effizienz der Berechnungen zu erhöhen, wird das Reaktionsnetzwerk nicht jeden hydrodynamischen Zeitschritt ausgeführt. Die optimale Zeitschrittgröße für die Netzwerkrechnungen, die sowohl eine effiziente als auch präzise Bestimmung der Isotopenhäufigkeiten ermöglicht, ist Gegenstand aktueller Forschung. Detaillierte Vergleiche von dieser Methode mit dem Post-Prozessierungsansatz wurden bereits begonnen.

Zusammenfassend unterstreichen die Ergebnisse dieser Arbeit die Notwendigkeit, den Vergleich von theoretischen Vorhersagen und Beobachtungen auf einen möglichst großen Wellenlängenbereich auszudehnen. Nur dies ermöglicht weitere Fortschritte bezüglich ungelöster Fragestellungen wie derjenigen nach dem Ursprung

galaktischer kosmischer Strahlung oder nach den Vorläufersystemen von Typ-Ia-Supernovaexplosionen. Die Tatsache, dass physikalisch unterschiedliche Modelle in den üblicherweise untersuchten Wellenlängenbereichen häufig große Ähnlichkeiten in ihren Beobachtungsgrößen aufweisen, erfordert einen komplementären Ansatz hinsichtlich weiterer Untersuchungen: Zum einen muss die Untersuchung theoretischer Modelle hinsichtlich charakteristischer Signaturen auf alle Energieskalen erweitert werden. In der vorliegenden Arbeit wird gezeigt, dass insbesondere jene Beobachtungsgrößen, die direkt mit Kernprozessen verknüpft sind, als solche charakteristischen Signaturen in Frage kommen. Dies muss natürlich mit weiteren Verbesserungen von nuklearen Netzwerkrechnungen und einer Reduktion der Unsicherheiten der Reaktionsraten auf theoretischer und experimenteller Seite einhergehen. Zum anderen muss ein solcher Multi-Wellenlängen-Ansatz auch durch die entsprechenden Detektionsmöglichkeiten der Beobachtungsgrößen unterstützt werden. Zur Zeit gibt es keine Satellitenmission, die den MeV-Energiebereich mit den benötigten Sensitivitäten abdeckt, und die Informationen, die in nuklearen Deexzitationslinien oder in der Gamma-Emission von radioaktivem Zerfall enthalten sind, können nicht genutzt werden. Daher weisen die Resultate dieser Arbeit auch auf die Notwendigkeit hin, eine Satellitenmission im MeV-Bereich in naher Zukunft zu realisieren. Weiterhin zeigt sich insbesondere bei der Unterscheidung von Explosionsszenarien von Typ-Ia-Supernovae, dass gerade die Kombination von Beobachtungsgrößen, die zu verschiedenen Zeitpunkten nach der Explosion detektierbar sind, zu erfolgversprechenden Resultaten führt. Nur wenn sowohl die Multi-Wellenlängen- als auch die Zeitentwicklungsaspekte der physikalischen Modelle gemeinsam berücksichtigt werden, können Vergleiche von theoretischen Vorhersagen mit experimentellen Beobachtungen zu weiteren Fortschritten hinsichtlich der Frage nach den Vorläufersystemen von Typ-Ia-Supernovae führen.

Nomenclature

Cas A	Cassiopeia A
CR	cosmic ray
FFN	Fuller, Fowler, and Newman
GT	Gamov-Teller
IGE	iron group element
IME	intermediate mass element
NSE	nuclear statistical equilibrium
QSE	quasi equilibrium
rms	root mean square
SN	supernova
SN Ia	Type Ia supernova
SNR	supernova remnant
WD	white dwarf

Bibliography

Abdo, A. A., Ackermann, M., Ajello, M., et al. 2010, ApJL, 710, L92

Achterberg, A., Gallant, Y. A., Kirk, J. G., & Guthmann, A. W. 2001, MNRAS, 328, 393

Ackermann, M., Ajello, M., Allafort, A., et al. 2013, Science, 339, 807

Agostinelli, S., Allison, J., Amako, K., et al. 2003, Nuclear Instruments and Methods in Physics Research A, 506, 250

Aharonian, F., Akhperjanian, A., Barrio, J., et al. 2001, A&A, 370, 112

Ajello, M., Greiner, J., Sato, G., et al. 2008, ApJ, 689, 666

Albert, J., Aliu, E., Anderhub, H., et al. 2007, A&A, 474, 937

Ambwani, K. & Sutherland, P. 1988, ApJ, 325, 820

Anderson, M., Rudnick, L., Leppik, P., Perley, R., & Braun, R. 1991, ApJ, 373, 146

Andritschke, R. 2006, PhD thesis, Technical University of Munich

Angulo, C., Arnould, M., Rayet, M., et al. 1999, Nuclear Physics A, 656, 3

Araya, M. & Cui, W. 2010, ApJ, 720, 20

Arcones, A. & Thielemann, F.-K. 2013, Journal of Physics G Nuclear Physics, 40, 013201

Arnett, D. 1996, Supernovae and Nucleosynthesis: An Investigation of the History of Matter from the Big Bang to the Present (Princeton University Press)

Arnett, D. & Livne, E. 1994a, ApJ, 427, 315

Arnett, D. & Livne, E. 1994b, ApJ, 427, 330

Ashworth, Jr., W. B. 1980, Journal for the History of Astronomy, 11, 1

Asplund, M., Grevesse, N., Sauval, A. J., & Scott, P. 2009, ARAA, 47, 481

Astro-H Mission. 2013, `http://astro-h.isas.jaxa.jp/researchers/sim/response.html`

Axelrod, T. S. 1980, PhD thesis, University of California, Santa Cruz

Axford, W. I., Leer, E., & Skadron, G. 1977, in International Cosmic Ray Conference, Vol. 11, International Cosmic Ray Conference, 132–137

Baade, W. & Zwicky, F. 1934a, Proceedings of the National Academy of Science, 20, 259

Baade, W. & Zwicky, F. 1934b, Proceedings of the National Academy of Science, 20, 254

Baars, J. W. M., Genzel, R., Pauliny-Toth, I. I. K., & Witzel, A. 1977, A&A, 61, 99

Badenes, C., Bravo, E., Borkowski, K. J., & Domínguez, I. 2003, ApJ, 593, 358

Badenes, C. 2010, Proc. National Academy of Science, 107, 7141

Badenes, C., Hughes, J. P., Bravo, E., & Langer, N. 2007, ApJ, 662, 472

Bader, G. & Deuflhard, P. 1983, Numerische Mathematik, 41, 373

Baring, M. G., Ellison, D. C., Reynolds, S. P., Grenier, I. A., & Goret, P. 1999, ApJ, 513, 311

Bell, A. R. 1978a, MNRAS, 182, 147

Bell, A. R. 1978b, MNRAS, 182, 443

Bell, A. R. 2013, Astroparticle Physics, 43, 56

Bell, A. R., Gull, S. F., & Kenderdine, S. 1975, Nature, 257, 463

Berezhko, E. G., Pühlhofer, G., & Völk, H. J. 2003, A&A, 400, 971

Berezhko, E. G. & Völk, H. J. 1997, Astroparticle Physics, 7, 183

Berezhko, E. G. & Völk, H. J. 2000, A&A, 357, 283

Bethe, H. & Heitler, W. 1934, Royal Society of London Proceedings Series A, 146, 83

Bethe, H. A. & Wilson, J. R. 1985, ApJ, 295, 14

Blandford, R. & Eichler, D. 1987, Physics Reports, 154, 1

Blandford, R. D. & Ostriker, J. P. 1978, ApJL, 221, L29

Blondin, J. M., Mezzacappa, A., & DeMarino, C. 2003, ApJ, 584, 971

Blondin, S., Mandel, K. S., & Kirshner, R. P. 2011, A&A, 526, A81+

Bloom, J. S., Kasen, D., Shen, K. J., et al. 2012, ApJL, 744, L17

Blumenthal, G. R. & Gould, R. J. 1970, Reviews of Modern Physics, 42, 237

Boggs, S. E. 2006, New Astron. Rev., 50, 604

Boller, T. 2011, The eROSITA background, `http://www2011.mpe.mpg.de/erosita/eROSITA_background_v8.pdf`

Bradt, H. 2004, Astronomy Methods (Cambridge University Press)

Branch, D. 1998, ARAA, 36, 17

Braun, R., Gull, S. F., & Perley, R. A. 1987, Nature, 327, 395

Bravo, E. & García-Senz, D. 2006, ApJL, 642, L157

Bravo, E. & Martínez-Pinedo, G. 2012, Phys. Rev. C, 85, 055805

Brown, B. A. & Wildenthal, B. H. 1988, Annual Review of Nuclear and Particle Science, 38, 29

Brown, L. S. & Sawyer, R. F. 1997, Reviews of Modern Physics, 69, 411

Brown, P. J., Dawson, K. S., de Pasquale, M., et al. 2012, ApJ, 753, 22

Browne, E. & Firestone, R. 1986, Table of Radioactive Isotopes, ed. V. Shirley (Wiley)

Burrows, A. & The, L.-S. 1990, ApJ, 360, 626

Bykov, A. M. & Fleishman, G. D. 1992, MNRAS, 255, 269

Bykov, A. M. & Uvarov, Y. A. 1999, Soviet Journal of Experimental and Theoretical Physics, 88, 465

Caprioli, D. 2012, JCAP, 7, 38

Caprioli, D., Blasi, P., Amato, E., & Vietri, M. 2008, ApJL, 679, L139

Cassisi, S., Iben, I. J., & Tornambe, A. 1998, ApJ, 496, 376

Chan, K.-W. & Lingenfelter, E. R. 1990, in International Cosmic Ray Conference, Vol. 1, International Cosmic Ray Conference, 101

Chan, K. W. & Lingenfelter, R. E. 1988, in American Institute of Physics Conference Series, Vol. 170, Nuclear Spectroscopy of Astrophysical Sources, ed. N. Gehrels & G. H. Share, 110–115

Chan, K. W. & Lingenfelter, R. E. 1991, ApJ, 368, 515

Chandra X-ray Center. 2012, The Chandra Proposers' Observatory Guide, `http://cxc.cfa.harvard.edu/proposer/POG/html/index.html`

Chandrasekhar, S. 1931, ApJ, 74, 81

Chevalier, R. A. 1977, ARAA, 15, 175

Chevalier, R. A. & Kirshner, R. P. 1979, ApJ, 233, 154

Clayton, D. D. 1974, ApJ, 188, 155

Clayton, D. D. 1983, Principles of stellar evolution and nucleosynthesis (Chicago: University of Chicago Press)

Clayton, D. D., Colgate, S. A., & Fishman, G. J. 1969, ApJ, 155, 75

Clayton, D. D. & The, L.-S. 1991, ApJ, 375, 221

Colella, P. & Woodward, P. R. 1984, Journal of Computational Physics, 54, 174

Colgate, S. A. & McKee, C. 1969, ApJ, 157, 623

Courant, R., Friedrichs, K. O., & Lewy, H. 1928, Math. Ann., 100, 32

Cyburt, R. H., Amthor, A. M., Ferguson, R., et al. 2010, ApJS, 189, 240

Dan, M., Rosswog, S., Guillochon, J., & Ramirez-Ruiz, E. 2011, ApJ, 737, 89

DeLaney, T. & Rudnick, L. 2003, ApJ, 589, 818

Dermer, C. D. 1986, A&A, 157, 223

Di Stefano, R. 2010, ApJ, 712, 728

Docenko, D. & Sunyaev, R. A. 2010, A&A, 509, A59

Drury, L. 1983, Space Sci. Rev., 36, 57

Dubner, G. M., Velázquez, P. F., Goss, W. M., & Holdaway, M. A. 2000, AJ, 120, 1933

Ellison, D. C., Decourchelle, A., & Ballet, J. 2005, A&A, 429, 569

Engelmann, J. J., Ferrando, P., Soutoul, A., Goret, P., & Juliusson, E. 1990, A&A, 233, 96

Fermi, E. 1949, Physical Review, 75, 1169

Fesen, R. A., Hammell, M. C., Morse, J., et al. 2006, ApJ, 645, 283

Filippenko, A. V. 1997, ARAA, 35, 309

Fink, M., Kromer, M., Seitenzahl, I. R., et al. 2013, ArXiv e-prints

Fink, M., Röpke, F. K., Hillebrandt, W., et al. 2010, A&A, 514, A53

Fransson, C., Lundqvist, P., & Chevalier, R. A. 1996, ApJ, 461, 993

Fryxell, B. A., Müller, E., & Arnett, W. D. 1989, Hydrodynamics and nuclear burning, MPA Green Report 449, Max-Planck-Institut für Astrophysik, Garching

Fuller, G. M., Fowler, W. A., & Newman, M. J. 1980, ApJS, 42, 447

Fuller, G. M., Fowler, W. A., & Newman, M. J. 1982a, ApJ, 252, 715

Fuller, G. M., Fowler, W. A., & Newman, M. J. 1982b, ApJS, 48, 279

Fuller, G. M., Fowler, W. A., & Newman, M. J. 1985, ApJ, 293, 1

Gaensler, B. M. & Slane, P. O. 2006, ARAA, 44, 17

Gaisser, T. K., Protheroe, R. J., & Stanev, T. 1998, ApJ, 492, 219

Geier, S., Heber, U., Kupfer, T., & Napiwotzki, R. 2010, A&A, 515, A37

Gilfanov, M. & Bogdán, Á. 2010, Nature, 463, 924

Ginzburg, V. L. & Syrovatskii, S. I. 1969, The origin of cosmic rays (New York: Gordon and Breach)

Ginzburg, V. L. & Syrovatskij, S. I. 1967, in IAU Symposium, Vol. 31, Radio Astronomy and the Galactic System, ed. H. van Woerden, 411

Giordano, F., Naumann-Godo, M., Ballet, J., et al. 2012, ApJL, 744, L2

Godunov, S. K. 1959, Matematicheskii Sbornik, 47, 271

Gómez-Gomar, J., Isern, J., & Jean, P. 1998, MNRAS, 295, 1

Goobar, A. & Leibundgut, B. 2011, Annual Review of Nuclear and Particle Science, 61, 251

Gotthelf, E. V., Koralesky, B., Rudnick, L., et al. 2001, ApJL, 552, L39

Greiner, J., Iyudin, A., Kanbach, G., et al. 2009, Experimental Astronomy, 23, 91

Greiner, J., Mannheim, K., Aharonian, F., et al. 2012, Experimental Astronomy, 34, 551

Gruber, D. E., Matteson, J. L., Peterson, L. E., & Jung, G. V. 1999, ApJ, 520, 124

Gutierrez, J., Garcia-Berro, E., Iben, I. J., et al. 1996, ApJ, 459, 701

Hachinger, S., Mazzali, P. A., Taubenberger, S., Pakmor, R., & Hillebrandt, W. 2009, MNRAS, 399, 1238

Hachisu, I., Kato, M., & Nomoto, K. 1999, ApJ, 522, 487

Hachisu, I., Kato, M., & Nomoto, K. 2010, ApJL, 724, L212

Hamuy, M., Phillips, M. M., Suntzeff, N. B., et al. 1996, AJ, 112, 2391

Harkness, R. 1991, in European Southern Observatory Conference and Workshop Proceedings, Vol. 37, European Southern Observatory Conference and Workshop Proceedings, ed. I. J. Danziger & K. Kjaer, 447

Harrison, F. A., Boggs, S., Christensen, F., et al. 2010, in Space Telescopes and Instrumentation 2010: Ultraviolet to Gamma Ray, ed. M. Arnaud, S. S. Murray, & T. Takahashi, SPIE Conf. Ser. 7732

Heger, A., Fryer, C. L., Woosley, S. E., Langer, N., & Hartmann, D. H. 2003, ApJ, 591, 288

Heger, A., Woosley, S. E., & Spruit, H. C. 2005, ApJ, 626, 350

Helder, E. A. & Vink, J. 2008, ApJ, 686, 1094

Helder, E. A., Vink, J., Bykov, A. M., et al. 2012, Space Sci. Rev., 173, 369

Helfand, D. J., Collins, B. F., & Gotthelf, E. V. 2003, ApJ, 582, 783

Henke, B. L., Gullikson, E. M., & Davis, J. C. 1993, At. Data Nucl. Data Tables, 54, 181

Herant, M., Benz, W., Hix, W. R., Fryer, C. L., & Colgate, S. A. 1994, ApJ, 435, 339

Hess, V. F. 1912, Phys. Zeit., 13, 1084

Higham, D. J. & Trefethen, L. N. 1993, BIT Numerical Mathematics, 33, 285

Hillas, A. M. 2005, Journal of Physics G Nuclear Physics, 31, 95

Hillas, A. M. 2006, Journal of Physics Conference Series, 47, 168

Hillebrandt, W., Kromer, M., Röpke, F. K., & Ruiter, A. J. 2013, Frontiers of Physics, 8, 116

Hillebrandt, W. & Niemeyer, J. C. 2000, ARAA, 38, 191

Hinton, J. A. & Hofmann, W. 2009, ARAA, 47, 523

Hirsch, J. G. & Page, D. 1998, Nuclear and particle astrophysics (Cambridge University Press)

Hix, W. R. & Meyer, B. S. 2006, Nuclear Physics A, 777, 188

Hix, W. R. & Thielemann, F.-K. 1999, ApJ, 511, 862

Höflich, P., Khokhlov, A., & Müller, E. 1992, A&A, 259, 549

Höflich, P., Wheeler, J. C., & Khokhlov, A. 1998, ApJ, 492, 228

Homeier, D., Koester, D., Hagen, H., et al. 1998, A&A, 338, 563

Hörandel, J. R. 2008, Advances in Space Research, 41, 442

Houck, J. C. & Allen, G. E. 2006, ApJS, 167, 26

Howell, D. A., Sullivan, M., Nugent, P. E., et al. 2006, Nature, 443, 308

Hoyle, F. & Fowler, W. A. 1960, ApJ, 132, 565

Hughes, J. P., Chugai, N., Chevalier, R., Lundqvist, P., & Schlegel, E. 2007, ApJ, 670, 1260

Humensky, T. B. 2008, in American Institute of Physics Conference Series, Vol. 1085, American Institute of Physics Conference Series, ed. F. A. Aharonian, W. Hofmann, & F. Rieger, 357–360

Iben, Jr., I. & Tutukov, A. V. 1984, ApJS, 54, 335

Iben, Jr., I. & Tutukov, A. V. 1985, ApJS, 58, 661

Iliadis, C., D'Auria, J. M., Starrfield, S., Thompson, W. J., & Wiescher, M. 2001, ApJS, 134, 151

Immler, S., Brown, P. J., Milne, P., et al. 2006, ApJL, 648, L119

Iwamoto, K., Brachwitz, F., Nomoto, K., et al. 1999, ApJS, 125, 439

Iwamoto, K., Mazzali, P. A., Nomoto, K., et al. 1998, Nature, 395, 672

Iyudin, A. F., Bennett, K., Bloemen, H., et al. 1995, A&A, 300, 422

Janka, H.-T. 2012, Annual Review of Nuclear and Particle Science, 62, 407

Janka, H.-T., Hanke, F., Hüdepohl, L., et al. 2012, Progress of Theoretical and Experimental Physics, 2012, 010000

Jha, S., Kirshner, R. P., Challis, P., et al. 2006, AJ, 131, 527

Jones, F. C. & Ellison, D. C. 1991, Space Sci. Rev., 58, 259

Jordan, G. C., Gupta, S. S., & Meyer, B. S. 2003, Phys. Rev. C, 68, 065801

Jordan, IV, G. C., Fisher, R. T., Townsley, D. M., et al. 2008, ApJ, 681, 1448

Kalberla, P. M. W., Burton, W. B., Hartmann, D., et al. 2005, A&A, 440, 775

Kamiya, Y., Tanaka, M., Nomoto, K., et al. 2012, ApJ, 756, 191

Kasen, D., Röpke, F. K., & Woosley, S. E. 2009, Nature, 460, 869

Kassim, N. E., Perley, R. A., Dwarakanath, K. S., & Erickson, W. C. 1995, ApJL, 455, L59

Kerzendorf, W. E., Schmidt, B. P., Asplund, M., et al. 2009, ApJ, 701, 1665

Khokhlov, A. M. 1989, MNRAS, 239, 785

Khokhlov, A. M. 1991, A&A, 245, 114

Kirk, J. G. & Schneider, P. 1987, ApJ, 315, 425

Kobayashi, C. & Nomoto, K. 2009, ApJ, 707, 1466

Kozlovsky, B., Murphy, R. J., & Ramaty, R. 2002, ApJS, 141, 523

Krause, O., Birkmann, S. M., Usuda, T., et al. 2008, Science, 320, 1195

Kromer, M. & Sim, S. A. 2009, MNRAS, 398, 1809

Kromer, M., Sim, S. A., Fink, M., et al. 2010, ApJ, 719, 1067

Krymskii, G. F. 1977, Akademiia Nauk SSSR Doklady, 234, 1306

Kuchner, M. J., Kirshner, R. P., Pinto, P. A., & Leibundgut, B. 1994, ApJL, 426, L89

Kumagai, S. & Nomoto, K. 1997, in NATO ASIC Proc. 486: Thermonuclear Supernovae, ed. P. Ruiz-Lapuente, R. Canal, & J. Isern, 515

Laming, J. M. & Hwang, U. 2003, ApJ, 597, 347

Landau, L. D. & Lifshitz, E. M. 1959, Fluid mechanics (Oxford: Pergamon Press)

Langanke, K. & Martinez-Pinedo, G. 2000, Nuclear Physics A, 673, 481

Lazendic, J. S., Dewey, D., Schulz, N. S., & Canizares, C. R. 2006, ApJ, 651, 250

Leibundgut, B. 2008, General Relativity and Gravitation, 40, 221

Leising, M. D. 2001, ApJ, 563, 185

Leising, M. D. 2006, ApJ, 651, 1019

Levenson, N. A., Graham, J. R., Keller, L. D., & Richter, M. J. 1998, ApJS, 118, 541

LeVeque, R. J. 1998, in Computational Methods for Astrophysical Flows, ed. O. Steiner & A. Gautschy, Saas-Fee Advanced Course 27 (Berlin Heidelberg New York: Springer), 1–159

Li, W., Bloom, J. S., Podsiadlowski, P., et al. 2011a, Nature, 480, 348

Li, W., Chornock, R., Leaman, J., et al. 2011b, MNRAS, 412, 1473

Li, W., Filippenko, A. V., Chornock, R., et al. 2003, PASP, 115, 453

Lingenfelter, R. E. & Higdon, J. C. 2007, ApJ, 660, 330

Livio, M. 2000, in Type Ia Supernovae, Theory and Cosmology. Edited by J. C. Niemeyer and J. W. Truran. Published by Cambridge University Press, 2000., p.33, ed. J. C. Niemeyer & J. W. Truran, 33–48

Livne, E. & Arnett, D. 1995, ApJ, 452, 62

Lucek, S. G. & Bell, A. R. 2000, MNRAS, 314, 65

Lucy, L. B. 1999, A&A, 344, 282

Lucy, L. B. 2005, A&A, 429, 19

Lundmark, K. 1920, Kungl. Svenska Vetenskapsakademiens Handlingar, 60, 1

Maeda, K., Terada, Y., Kasen, D., et al. 2012, ApJ, 760, 54

Maeda, Y., Uchiyama, Y., Bamba, A., et al. 2009, PASJ, 61, 1217

Malkov, M. A. 1997, ApJ, 485, 638

Malkov, M. A. & O'C Drury, L. 2001, Reports on Progress in Physics, 64, 429

Maoz, D. & Mannucci, F. 2012, Publications of the Astronomical Society of Australia, 29, 447

Mazzali, P. A., Chugai, N., Turatto, M., et al. 1997, MNRAS, 284, 151

Mazzali, P. A., Danziger, I. J., & Turatto, M. 1995, A&A, 297, 509

Mazzali, P. A., Röpke, F. K., Benetti, S., & Hillebrandt, W. 2007, Science, 315, 825

Meakin, C. A., Seitenzahl, I., Townsley, D., et al. 2009, ApJ, 693, 1188

Meneguzzi, M. & Reeves, H. 1975, A&A, 40, 91

Meng, X.-C. & Yang, W.-M. 2011, Research in Astronomy and Astrophysics, 11, 965

Mennekens, N., Vanbeveren, D., De Greve, J. P., & De Donder, E. 2010, A&A, 515, A89

Milne, P. A., Hungerford, A. L., Fryer, C. L., et al. 2004, ApJ, 613, 1101

Minkowski, R. 1940, PASP, 52, 206

Mizuno, T., Kamae, T., Godfrey, G., et al. 2004, ApJ, 614, 1113

Morlino, G., Blasi, P., & Vietri, M. 2007, ApJ, 662, 980

Müller, E., Höflich, P., & Khokhlov, A. 1991, A&A, 249, L1

Nagano, M. & Watson, A. A. 2000, Reviews of Modern Physics, 72, 689

Nandra, K., Barret, D., Barcons, X., et al. 2013, ArXiv e-prints

Nelemans, G., Napiwotzki, R., Karl, C., et al. 2005, A&A, 440, 1087

Nikolić, S., van de Ven, G., Heng, K., et al. 2013, Science, 340, 45

Nomoto, K. 1984, ApJ, 277, 791

Nomoto, K. & Kondo, Y. 1991, ApJL, 367, L19

Nomoto, K. & Sugimoto, D. 1977, PASJ, 29, 765

Nomoto, K., Thielemann, F.-K., & Miyaji, S. 1985, A&A, 149, 239

Nugent, P. E., Sullivan, M., Cenko, S. B., et al. 2011, Nature, 480, 344

Oda, T., Hino, M., Muto, K., Takahara, M., & Sato, K. 1994, Atomic Data and Nuclear Data Tables, 56, 231

Osher, S. & Sethian, J. A. 1988, Journal of Computational Physics, 79, 12

Ostrowski, M. 1999, A&A, 345, 256

Pacholczyk, A. G. 1970, Radio astrophysics. Nonthermal processes in galactic and extragalactic sources (San Francisco: Freeman)

Padmanabhan, P. 2000, Theoretical astrophysics. Volume 1: Astrophysical processes (Cambridge University Press)

Padmanabhan, T. 2001, Theoretical Astrophysics, Volume 2: Stars and Stellar Systems (Cambridge University Press)

Pakmor, R., Edelmann, P., Röpke, F. K., & Hillebrandt, W. 2012a, MNRAS, 424, 2222

Pakmor, R., Kromer, M., Röpke, F. K., et al. 2010, Nature, 463, 61

Pakmor, R., Kromer, M., Taubenberger, S., et al. 2012b, ApJL, 747, L10

Pakmor, R., Kromer, M., Taubenberger, S., & Springel, V. 2013, ApJL, 770, L8

Parikh, A., José, J., Seitenzahl, I. R., & Röpke, F. K. 2013, A&A, 557, A3

Parizot, E., Marcowith, A., van der Swaluw, E., Bykov, A. M., & Tatischeff, V. 2004, A&A, 424, 747

Patat, F., Benetti, S., Cappellaro, E., et al. 1996, MNRAS, 278, 111

Perlmutter, S., Aldering, G., Goldhaber, G., et al. 1999, ApJ, 517, 565

Phillips, M. M. 1993, ApJL, 413, L105

Phillips, M. M., Wells, L. A., Suntzeff, N. B., et al. 1992, AJ, 103, 1632

Plewa, T., Calder, A. C., & Lamb, D. Q. 2004, ApJL, 612, L37

Prantzos, N., Boehm, C., Bykov, A. M., et al. 2011, Reviews of Modern Physics, 83, 1001

Pskovskii, I. P. 1977, Soviet Astronomy, 21, 675

Ramaty, R., Kozlovsky, B., & Lingenfelter, R. E. 1979, ApJS, 40, 487

Rauscher, T. 2008, Online code NON-SMOKER$^{\mathrm{WEB}}$, version 5.0w and higher, http://nucastro.org/websmoker.html

Read, A. M. & Ponman, T. J. 2003, A&A, 409, 395

Reed, J. E., Hester, J. J., Fabian, A. C., & Winkler, P. F. 1995, ApJ, 440, 706

Reinecke, M., Hillebrandt, W., & Niemeyer, J. C. 2002, A&A, 386, 936

Reinecke, M., Hillebrandt, W., Niemeyer, J. C., Klein, R., & Gröbl, A. 1999, A&A, 347, 724

Reinecke, M. A. 2001, PhD thesis, Technical University of Munich

Renaud, M., Vink, J., Decourchelle, A., et al. 2006, ApJL, 647, L41

Reynolds, S. P. 2008, ARAA, 46, 89

Rho, J. & Petre, R. 1998, ApJL, 503, L167

Riess, A. G., Filippenko, A. V., Challis, P., et al. 1998, AJ, 116, 1009

Riquelme, M. A. & Spitkovsky, A. 2008, International Journal of Modern Physics D, 17, 1803

Röpke, F. K. 2005, A&A, 432, 969

Röpke, F. K., Gieseler, M., Reinecke, M., Travaglio, C., & Hillebrandt, W. 2006a, A&A, 453, 203

Röpke, F. K. & Hillebrandt, W. 2005, A&A, 431, 635

Röpke, F. K., Hillebrandt, W., Niemeyer, J. C., & Woosley, S. E. 2006b, A&A, 448, 1

Röpke, F. K., Hillebrandt, W., Schmidt, W., et al. 2007, ApJ, 668, 1132

Röpke, F. K., Kromer, M., Seitenzahl, I. R., et al. 2012, ApJL, 750, L19

Röpke, F. K. & Niemeyer, J. C. 2007, A&A, 464, 683

Ruiter, A. J., Belczynski, K., Sim, S. A., et al. 2011, MNRAS, 1282

Ruiter, A. J., Sim, S. A., Pakmor, R., et al. 2013, MNRAS, 429, 1425

Ruiz-Lapuente, P., Comeron, F., Méndez, J., et al. 2004, Nature, 431, 1069

Russell, B. R. & Immler, S. 2012, ApJL, 748, L29

Ryle, M. & Smith, F. G. 1948, Nature, 162, 462

Saio, H. & Nomoto, K. 1985, A&A, 150, L21

Scannapieco, C., Tissera, P. B., White, S. D. M., & Springel, V. 2008, MNRAS, 389, 1137

Schmidt, W., Niemeyer, J. C., Hillebrandt, W., & Röpke, F. K. 2006, A&A, 450, 283

Schure, K. M., Bell, A. R., O'C Drury, L., & Bykov, A. M. 2012, Space Sci. Rev., 173, 491

Sedov, L. I. 1959, Similarity and Dimensional Methods in Mechanics (New York: Academic Press)

Seitenzahl, I. R., Summa, A., Krauss, F., et al. 2014, submitted to MNRAS

Seitenzahl, I. R., Cescutti, G., Röpke, F. K., Ruiter, A. J., & Pakmor, R. 2013a, A&A, 559, L5

Seitenzahl, I. R., Ciaraldi-Schoolmann, F., & Röpke, F. K. 2011, MNRAS, 414, 2709

Seitenzahl, I. R., Ciaraldi-Schoolmann, F., Röpke, F. K., et al. 2013b, MNRAS, 429, 1156

Seitenzahl, I. R., Meakin, C. A., Townsley, D. M., Lamb, D. Q., & Truran, J. W. 2009a, ApJ, 696, 515

Seitenzahl, I. R., Röpke, F. K., Fink, M., & Pakmor, R. 2010, MNRAS, 407, 2297

Seitenzahl, I. R., Taubenberger, S., & Sim, S. A. 2009b, MNRAS, 400, 531

Shelton, R. L., Cox, D. P., Maciejewski, W., et al. 1999, ApJ, 524, 192

Silverman, J. M., Nugent, P. E., Gal-Yam, A., et al. 2013, ApJS, 207, 3

Sim, S. A. 2007, MNRAS, 375, 154

Sim, S. A. & Mazzali, P. A. 2008, MNRAS, 385, 1681

Sim, S. A., Seitenzahl, I. R., Kromer, M., et al. 2013, MNRAS, 436, 333

Slane, P., Helfand, D. J., van der Swaluw, E., & Murray, S. S. 2004, ApJ, 616, 403

Smartt, S. J. 2009, ARAA, 47, 63

Smiljanovski, V., Moser, V., & Klein, R. 1997, Combustion Theory Modelling, 1, 183

Stehle, M., Mazzali, P. A., Benetti, S., & Hillebrandt, W. 2005, MNRAS, 360, 1231

Stephenson, F. R. & Green, D. A. 2005, in Astronomical Society of the Pacific Conference Series, Vol. 342, 1604-2004: Supernovae as Cosmological Lighthouses, ed. M. Turatto, S. Benetti, L. Zampieri, & W. Shea, 63

Stritzinger, M., Leibundgut, B., Walch, S., & Contardo, G. 2006, A&A, 450, 241

Strong, A. W., Bloemen, H., Collmar, W., et al. 2000, in American Institute of Physics Conference Series, Vol. 510, American Institute of Physics Conference Series, ed. M. L. McConnell & J. M. Ryan, 60–63

Sturner, S. J., Skibo, J. G., Dermer, C. D., & Mattox, J. R. 1997, ApJ, 490, 619

Summa, A. 2011, in International Cosmic Ray Conference, Vol. 7, International Cosmic Ray Conference, 102

Summa, A., Elsässer, D., & Mannheim, K. 2011, A&A, 533, A13

Summa, A., Ulyanov, A., Kromer, M., et al. 2013, A&A, 554, A67

Sussman, M., Smereka, P., & Osher, S. 1994, Journal of Computational Physics, 114, 146

Takahashi, T., Mitsuda, K., Kelley, R., et al. 2010, in Society of Photo-Optical Instrumentation Engineers (SPIE) Conference Series, Vol. 7732, Society of Photo-Optical Instrumentation Engineers (SPIE) Conference Series

Tammann, G. A., Loeffler, W., & Schroeder, A. 1994, ApJS, 92, 487

Taubenberger, S., Benetti, S., Childress, M., et al. 2011, MNRAS, 412, 2735

Taylor, G. 1950, Royal Society of London Proceedings Series A, 201, 159

Thielemann, F.-K., Nomoto, K., & Hashimoto, M.-A. 1996, ApJ, 460, 408

Thielemann, F.-K., Nomoto, K., & Yokoi, K. 1986, A&A, 158, 17

Thorstensen, J. R., Fesen, R. A., & van den Bergh, S. 2001, AJ, 122, 297

Timmes, F. X. & Woosley, S. E. 1992, ApJ, 396, 649

Toonen, S., Nelemans, G., & Portegies Zwart, S. 2012, A&A, 546, A70

Townsley, D. M. & Bildsten, L. 2005, ApJ, 628, 395

Travaglio, C., Hillebrandt, W., Reinecke, M., & Thielemann, F.-K. 2004, A&A, 425, 1029

Truelove, J. K. & McKee, C. F. 1999, ApJS, 120, 299

Truran, J. W., Arnett, W. D., & Cameron, A. G. W. 1967, Canadian Journal of Physics, 45, 2315

Tuffs, R. J. 1986, MNRAS, 219, 13

Turatto, M. 2003, in Lecture Notes in Physics, Vol. 598, Supernovae and Gamma-Ray Bursters, ed. K. Weiler (Springer Berlin Heidelberg), 21–36

Uchiyama, Y. & Aharonian, F. A. 2008, ApJL, 677, L105

Vink, J. 2012, A&A Rev., 20, 49

Vink, J. & Laming, J. M. 2003, ApJ, 584, 758

Vink, J., Laming, J. M., Kaastra, J. S., et al. 2001, ApJL, 560, L79

Wanajo, S., Nomoto, K., Janka, H.-T., Kitaura, F. S., & Müller, B. 2009, ApJ, 695, 208

Wang, B. & Han, Z. 2012, New Astronomy Review, 56, 122

Webber, W. R. 1998, ApJ, 506, 329

Webbink, R. F. 1984, ApJ, 277, 355

Weidemann, V. & Koester, D. 1983, A&A, 121, 77

Weidenspointner, G., Shrader, C. R., Knödlseder, J., et al. 2006, A&A, 450, 1013

Weiler, K. W. & Panagia, N. 1978, A&A, 70, 419

Whelan, J. & Iben, I. J. 1973, ApJ, 186, 1007

Williams, B. J., Blair, W. P., Blondin, J. M., et al. 2011, ApJ, 741, 96

Willingale, R., Bleeker, J. A. M., van der Heyden, K. J., Kaastra, J. S., & Vink, J. 2002, A&A, 381, 1039

Wilms, J., Allen, A., & McCray, R. 2000, ApJ, 542, 914

Woosley, S. E., Arnett, W. D., & Clayton, D. D. 1973, ApJS, 26, 231

Woosley, S. E., Blinnikov, S., & Heger, A. 2007, Nature, 450, 390

Woosley, S. E. & Bloom, J. S. 2006, ARAA, 44, 507

Woosley, S. E. & Heger, A. 2006, ApJ, 637, 914

Woosley, S. E., Heger, A., & Weaver, T. A. 2002, Reviews of Modern Physics, 74, 1015

Woosley, S. E. & Kasen, D. 2011, ApJ, 734, 38

Woosley, S. E., Kerstein, A. R., Sankaran, V., Aspden, A. J., & Röpke, F. K. 2009, ApJ, 704, 255

Woosley, S. E., Taam, R. E., & Weaver, T. A. 1986, ApJ, 301, 601

Woosley, S. E. & Weaver, T. A. 1994, in Les Houches Session LIV: Supernovae, ed. S. A. Bludman, R. Mochkovitch, & J. Zinn-Justin (Amsterdam: North-Holland), 63–154

Yamanaka, M., Kawabata, K. S., Kinugasa, K., et al. 2009, ApJL, 707, L118

Yanasak, N. E., Wiedenbeck, M. E., Mewaldt, R. A., et al. 2001, ApJ, 563, 768

Yoon, S.-C. & Langer, N. 2005, A&A, 443, 643

Zirakashvili, V. N., Aharonian, F. A., Yang, R., Ona-Wilhelmi, E., & Tuffs, R. J. 2013, ArXiv e-prints

Zirakashvili, V. N. & Ptuskin, V. S. 2008, in American Institute of Physics Conference Series, Vol. 1085, American Institute of Physics Conference Series, ed. F. A. Aharonian, W. Hofmann, & F. Rieger, 336–339

Zoglauer, A., Andritschke, R., & Schopper, F. 2006, New Astron. Rev., 50, 629

Zwicky, F. 1938, ApJ, 88, 522

Appendix

Publikationsliste

Im Laufe des Dissertationsvorhabens wurden folgende wissenschaftliche Arbeiten erstellt und veröffentlicht:

1. **A. Summa**, D. Elsässer, and K. Mannheim. Nuclear de-excitation line spectrum of Cassiopeia A. *Astronomy and Astrophysics*, 533:A13, September 2011.
2. **A. Summa**. Nuclear Lines as a Fingerprint of Hadronic Cosmic Rays. *International Cosmic Ray Conference*, 7:102, 2011
3. S. Saxena, **A. Summa**, D. Elsässer, M. Rüger, and K. Mannheim. Constraints on dark matter annihilation from M87. Signatures of prompt and inverse-Compton gamma rays. *European Physical Journal C*, 71:1815, November 2011.
4. **A. Summa**, A. Ulyanov, M. Kromer, S. Boyer, F. K. Röpke, S. A. Sim, I. R. Seitenzahl, M. Fink, K. Mannheim, R. Pakmor, F. Ciaraldi-Schoolmann, R. Diehl, K. Maeda, and W. Hillebrandt. Gamma-ray diagnostics of Type Ia supernovae. Predictions of observables from three-dimensional modeling. *Astronomy and Astrophysics*, 554:A67, June 2013.
5. I. R. Seitenzahl, **A. Summa**, F. Krauss, S. A. Sim, R. Diehl, D. Elsässer, M. Fink, W. Hillebrandt, M. Kromer, K. Maeda, K. Mannheim, R. Pakmor, F. K. Röpke, A. J. Ruiter, and J. Wilms. 5.9 keV Mn K-shell X-ray luminosity from the decay of ^{55}Fe in Type Ia supernova models. *Submitted to Monthly Notices of the Royal Astronomical Society.*

Danksagung

Mein besonderer Dank gilt an erster Stelle Herrn Prof. Dr. Friedrich Röpke und Herrn Prof. Dr. Karl Mannheim für die Möglichkeit, die vorliegende Dissertation am Lehrstuhl für Astronomie anzufertigen. Ohne ihre kompetente Beratung und ihre kontinuierliche Unterstützung hätte ich diese Arbeit nicht erstellen können.

Ich möchte mich bei allen Mitgliedern der Typ Ia-Supernova-Gruppe bedanken, auf deren Hilfe ich immer zählen konnte. Insbesondere sind zu nennen Michael Fink und Philipp Edelmann, die mich in die Benutzung des Supernova-Codes sowie die Programmiertechniken von nuklearen Reaktionsnetzwerken eingeführt haben, und Ivo Seitenzahl, der bei allen physikalischen wie nicht-physikalischen Fragen immer ansprechbar war. Ich danke Markus Kromer, Rüdiger Pakmor und Stuart Sim für die konstruktive Zusammenarbeit sowie Sebastian Ohlmann für seine Hilfestellungen bei technischen Problemen. Neben den anregenden wissenschaftlichen Gesprächen und Diskussionen in der Gruppe werde ich gerade auch die gemeinsamen Grill- und Feuerzangenbowlenabende in bester Erinnerung behalten.

Insgesamt möchte ich die gute Arbeitsatmosphäre und das angenehme Miteinander aller Kolleginnen und Kollegen am Lehrstuhl für Astronomie hervorheben. Ich danke dem Systemadministrator Aleksander Paravac für seine Unterstützung bei Computerproblemen aller Art sowie Felicia Krauß für ihre fachkundige Hilfe bei sämtlichen Fragen rund um Röntgenbeobachtungen. Meiner Bürokollegin Dorit Eisenacher bin ich für die vielen Gespräche auch nichtwissenschaftlicher Art dankbar, die für eine gelegentlich notwendige Ablenkung gesorgt haben. Vielen Dank auch an Sonja Boyer für die bereichernde Zeit während der vergangenen Jahre in Würzburg.

Nicht zuletzt sage ich meinen Eltern herzlichen Dank für ihr Verständnis, ihren Beistand und ihre Geduld.

Eigenständigkeitserklärung

Hiermit versichere ich an Eides statt, die Dissertation eigenständig angefertigt und keine anderen als die angegebenen Quellen und Hilfsmittel benutzt zu haben.

Würzburg, den 24.02.2014

Alexander Summa